# Homogeneous Atom-cavity Coupling for Quantum Metrology

by

**Baochen Wu**

B.S., Nanjing University, 2014

M.S., University of Colorado Boulder, 2018

A thesis submitted to the

Faculty of the Graduate School of the

University of Colorado in partial fulfillment

of the requirements for the degree of

Doctor of Philosophy

Department of Physics

2021

Committee Members:

James K. Thompson, Chair

Murray J. Holland

Konrad W. Lehnert

Jun Ye

Shu-Wei Huang

Wu, Baochen (Ph.D., Physics)

Homogeneous Atom-cavity Coupling for Quantum Metrology

Thesis directed by Prof. James K. Thompson

Interactions between cold atoms and optical cavities have been proved successful in generating large amounts of spin-squeezing. However, the inhomogeneous coupling between the atoms and optical cavity, due to the standing wave nature of the cavity modes and the incommensurateness between the trapping and probing light, can limit the applications of spin-squeezed states. In this thesis, I will summarize our efforts towards creating homogeneous atom-cavity coupling, and attempts at utilizing spin-squeezed states in which the entanglement is more evenly distributed among all the atoms for quantum metrology.

I demonstrate a method to obtain more homogeneous atom-cavity coupling in the Lamb-Dicke regime by initially loading atoms into thousands of lattice sites and then using a spectroscopic method to select and keep only those atoms at lattice sites with near maximal coupling to the desired cavity mode. The degree of residual inhomogeneity is expected to reduce quadratically with the number of the retained atoms. We are able to select 4% of the atoms and get an average coupling strength of more than 91% the peak coupling strength.

I present an ongoing project to build an intracavity, guided atom interferometer with spin-squeezed states. Spin-squeezing homogeneously distributed between all the atoms are required, which will be realized by time-averaged probing of falling atoms, in the non-Lamb-Dicke regime. I will give a detailed account about how all the ingredients for the squeezed atom interferometry are realized and and a brief summary of our recent progress.

I will also talk about a novel cooling method utilizing adiabatic transfer on Raman transitions, and introduce a proposal for continuous real-time tracking of a quantum phase and the creation of spin-squeezed states in the quantum phase quadrature.

## Acknowledgements

Attending graduate school at JILA is one of the best decisions I have ever made. JILA is a place full of great physicists and wonderful engineers, where cool ideas come true.

I would like to thank my advisor James for his patience, guidance, tolerance, support and encouragement, as a mentor with great communication skills, a physicist with excellent intuition and a researcher full of passion. I have also worked with great labmates. Thank you to Kevin, Matt, Graham, Julia, Juan, Chengyi, Dylan, Matthew and Denton for all the help and discussions.

I would also like to thank all the engineers providing technical support for us. Thank you to Hans, Todd, Adam, Calvin, James, Kim and Tracy for helping us with machining problems. Thank you to Terry, Carl and other folks for helping us with electronics. Thank you to Dave and Mark for maintaining the clean room and making customized pieces.

At JILA, experimentalists can easily find theorists to discuss crazy ideas and ask questions. Thank you to Peiru, Haonan, Athreya and Murray.

There are fantastic visiting scholars at JILA. Thank you to Prof. Nicola Poli and Prof. Barak Dayan for discussing interesting ideas.

Life in Boulder has been pretty enjoyable. Thank you to my friends for playing computer games, playing Texas hold'em and working out together. Thank you to Jian for all the help and advice both on my life in Boulder and my career as a physicist.

I also want to acknowledge my high school physics teacher, Feng Yan. Thank you for motivating me to major in physics.

Finally, I would like to thank my parents for their unconditional love and support.

# Contents

**Chapter**

# Tables

**Table**

# Figures

**Figure**

# Chapter 1

# Introduction

The development of metrology has played a crucial role in human activity. More and more precise measurement of time, distance, weight, temperature, etc., has not only made human life more convenient, but also boosted the development of science and technology.

Let's take the metrology of time as an example. In ancient days, people kept track of time by monitoring the position of the sun, with hour-level uncertainty. The inventions of sundial, clepsydra and sandglass improved the uncertainty to minute level. Mechanical clocks and quartz clocks further advanced the imprecision to sub-second level. Quantum metrology was developed as physicists gained better understanding of quantum mechanics. Quantum metrology measures a physics quantity by probing the interactions between the quantity and quantum systems with discrete energy levels, whose precision is limited by the principles of quantum mechanics. With its help, atomic clocks based on masers at room temperature were able to give an uncertainty of $10^{-9}$ in fractional frequency unit in the 1950s [36], and have reached $10^{-16}$ in the 2010s [47] with the development of atomic fountains. Optical clocks have even reached $10^{-19}$ level of uncertainty [16, 70]. The current US time standard is based on caesium fountain clocks. Scientists from NIST and JILA have proposed a new time standard based on optical clocks [74].

Precise time-keeping has brought about great convenience to people's everyday life. For aeroplanes moving at 1000 miles/hour, the navigation can easily be off by miles, if the imprecision in time is at seconds level. It is also common that good deals will be fully claimed just several seconds after they start during Black Fridays! Even though quartz clocks are usually precise enough

for the two examples above, people may start to get an idea of how important precise time-keeping is. There are actually situations that we have to turn to quantum metrology with atomic clocks, for example, autonomous driving and navigation of missiles enabled by atomic clocks on satellites. With the development of optical clocks, tests of fundamental theory are enabled, say, variations of fine structure constant [90] and searches for dark matter [59].

Quantum metrology also opens up other possibilities in addition to precise time-keeping, for example, measurement of gravitational acceleration variation for mining. I will move on to discuss how quantum metrology works, what limits its precision and how we could break the limit.

## 1.1 Quantum Metrology and Spin Squeezing

Quantum metrology has become a powerful tool for precision measurement of physical quantities. It works by encoding the information of the quantity of interest into the quantum phase $\phi$ of the superposition state of a two-level system $|\psi\rangle = \left(|\downarrow\rangle + e^{i\phi}|\uparrow\rangle\right)/\sqrt{2}$. The information of the quantity of interest will be written into $\phi$ if it modifies the energy difference between $|\uparrow\rangle$ and $|\downarrow\rangle$ since the rate that $\phi$ changes is set by the energy difference $\dot{\phi} = (E_\uparrow - E_\downarrow)/\hbar$, where $\hbar$ is the reduced Planck constant. We then infer $\phi$ by applying couplings between $|\uparrow\rangle$ and $|\downarrow\rangle$ to map $\phi$ into a population difference between $|\uparrow\rangle$ and $|\downarrow\rangle$ which we can then measure to infer $\phi$. This process is named the Ramsey sequence. We will consider an electron in a magnetic field as an example. The spin of the electron aligned or anti-aligned to the magnetic field is the state we call $|\uparrow\rangle$ or $|\downarrow\rangle$. If we initialize the spin perpendicular to the magnetic field, the spin will precess at a rate set by the magnetic field, and the azimuthal angle the spin precesses through is the phase $\phi$. We are able to build a magnetometer by tracking $\phi$.

We often visualize the Ramsey sequence on Bloch spheres as shown in Fig. 1.1. The Bloch sphere is a geometrical representation of the quantum state of two-level systems. With $|\downarrow\rangle$ represented by a vector pointing at the south pole with coordinate $(0,\ 0,\ -\frac{1}{2})$ and $|\uparrow\rangle$ represented by a vector pointing at the north pole with coordinate $(0,\ 0,\ \frac{1}{2})$, a superposition state $|\psi\rangle = \left(\sin(\theta/2)|\downarrow\rangle + \cos(\theta/2)\, e^{i\phi}|\uparrow\rangle\right)$ can be represented on the Bloch sphere by the vector $(\cos(\phi)\sin(\theta),$

$\sin(\phi)\sin(\theta), \cos(\theta))/2$, with $\theta$ and $\phi$ now being interpreted as the polar coordinates of a vector of length 1/2 for a spin-1/2 system. When we have $N$ spin-1/2 systems which are in a product state of the wavefunction above, their individual Bloch vectors will connect tip-to-tail to form a collective Bloch vector, with length $N/2$. We show collective Bloch vectors in Fig. 1.1.

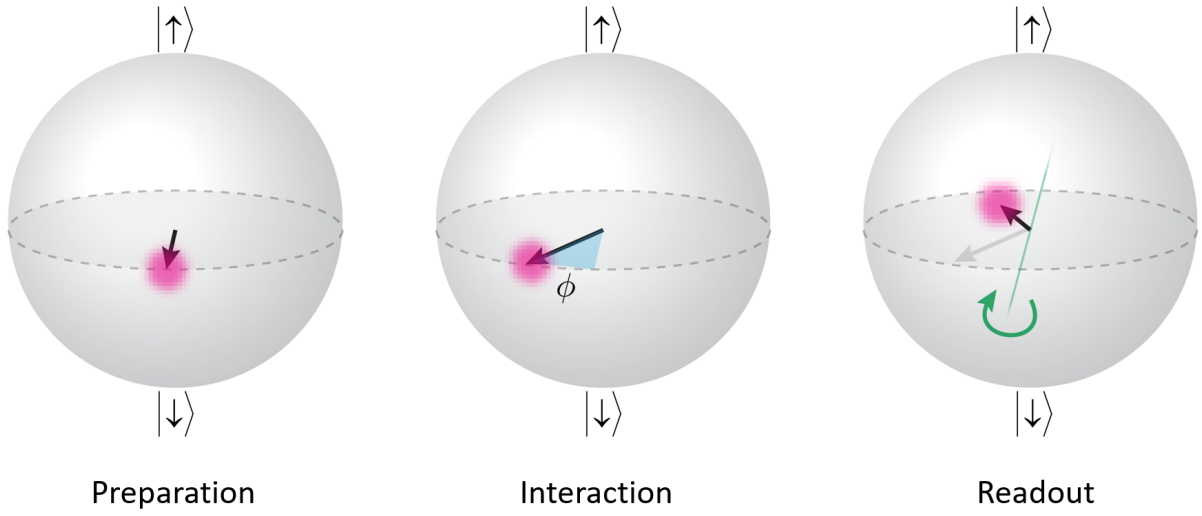


Figure 1.1: Working principles of quantum metrology. We initialize the collective Bloch vector representing the quantum state of the two-level systems onto the equator in the preparation stage. The Bloch vector will precess during the interaction stage under the effect of the quantity to be measured, for instance, the flow of time, accelerations, or a magnetic or electric field. Finally, we convert the quantum phase $\phi$ into atom number for readout. This is accomplished by once again applying a coupling between $|\uparrow\rangle$ and $|\downarrow\rangle$ with the correct phase to cause a rotation about the green axis through an angle $\pi/2$. By measuring the number of atoms in $|\uparrow\rangle$ and in $|\downarrow\rangle$, we can estimate the phase $\phi$ accrued during the interaction period.

Population measurement usually results in independent collapse of individual wavefunctions into either $|\downarrow\rangle$ or $|\uparrow\rangle$, which is subject to random-walk statistics. This sets a limit on the rms phase resolution the measurement can achieve, which we call the standard quantum limit (SQL), $\Delta\phi_{SQL} = 1/\sqrt{N}$ radians, as indicated by the pink blobs in Fig. 1.1. This is the fundamental limit on quantum metrology with unentangled atoms, and we call such a state a coherent spin state (CSS). As can be seen from the scaling, larger atom number will help to improve the precision of the measurement.

However, the number of atoms cannot be arbitrarily large, because of both technical con-

straints and potential atom-atom interactions that can lead to systematic errors and decoherence. We will eventually need to turn to quantum entanglement to break this limit and approach the fundamental limit set by quantum mechanics, which we call the Heisenberg limit, $\Delta\phi_{HL} = 1/N$ [39]. By engineering entanglement between the atoms, we could get a spin squeezed state (SSS), where atoms will conspire during the population measurement to cancel out the noise in the spin projection corresponding to the population basis, as indicated by the pink blobs in Fig. 1.2. We will refer to the noise in population basis as in atom number quadrature, and the noise in quantum phase (azimuthal angle on the Bloch sphere) as in phase quadrature throughout this thesis.

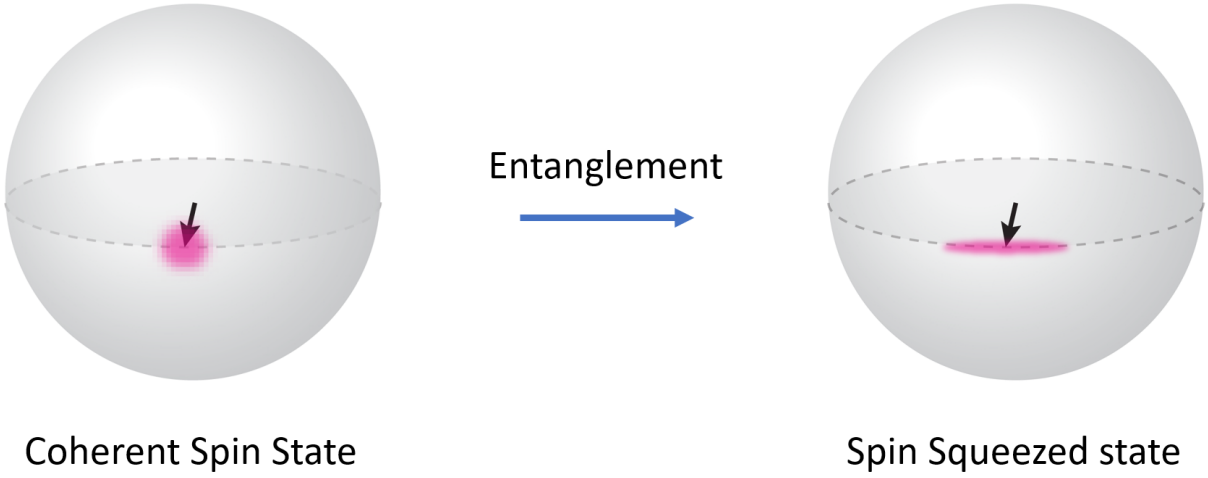


Figure 1.2: Coherent spin state and spin squeezed state

There have been many efforts to create spin squeezing through spin dynamics [14, 65, 97, 13], direct mapping from squeezed light [69] and quantum non-demolition measurement [51, 27, 20, 11]. We are able to create about 18 dB of squeezing, or 60 times improvement in the variance of atom number measurement, by cavity-based quantum non-demolition measurement in the Dicke state basis. More details of our method can be found in Sec. 3.1.1 [27, 26].

We move on in two directions. One is to make the squeezing better. We developed a site-dependent selection technique to achieve homogeneous atom-cavity coupling. The other one is to apply the squeezed states to quantum sensors. Here I will discuss the application of spin-squeezing

to an atom interferometer. I will define the inhomogeneous atom-cavity coupling problem in cavity QED experiments in Sec. 1.2, and give a brief introduction to atom interferometer in Sec. 1.3.

## 1.2 Inhomogeneous Atom-cavity Coupling

We typically send a lattice laser and an atomic probe laser into a two-mirror optical cavity for trapping and probing $^{87}$Rb atoms, with wavelengths of 813 nm and 780 nm respectively. There will be inhomogeneity in the coupling of individual atoms to the cavity because of the standing wave nature of the cavity modes [28]. Atoms are always trapped at the maxima of the optical lattice, but their coupling to the cavity can range between zero coupling and a maximum coupling depending on where they are trapped relative to the standing wave of the cavity mode of interest. For example in Fig. 1.3, atom A is trapped near an anti-node of the blue cavity mode of interest and so has maximal coupling, while atom D is trapped near a node of the cavity mode and so has very little coupling to the mode. The inhomogeneous coupling reduces the effective atom number [52], creates dephasing in driven systems [75], and brings about optomechanically-induced oscillations [27].

In Chapter 3, I will discuss these effects in detail and present our solution to this inhomogeneous coupling problem with site-dependent selections.

## 1.3 Atom Interferometry

An atom interferometer is the matterwave analog of an optical interferometer, where we take advantage of the wave nature of atoms. To understand how optical interferometers work, we first consider a Mach-Zehnder type optical interferometer in Fig. 1.4. One light beam is split into two paths first with a beam splitter. The two beams will gain differential phase $\Delta\Phi$ along different paths before they are recombined and interfered with mirrors and a second beam splitter. The intensities out of the two ports are proportional to $\cos^2(\Delta\Phi/2)$ and $\sin^2(\Delta\Phi/2)$ respectively.

The matterwave counterpart of beam splitters and mirrors are realized with two-photon Raman transitions, as shown in Fig. 1.5. For a cloud of free-falling atoms, a $\pi/2$-pulse could impart

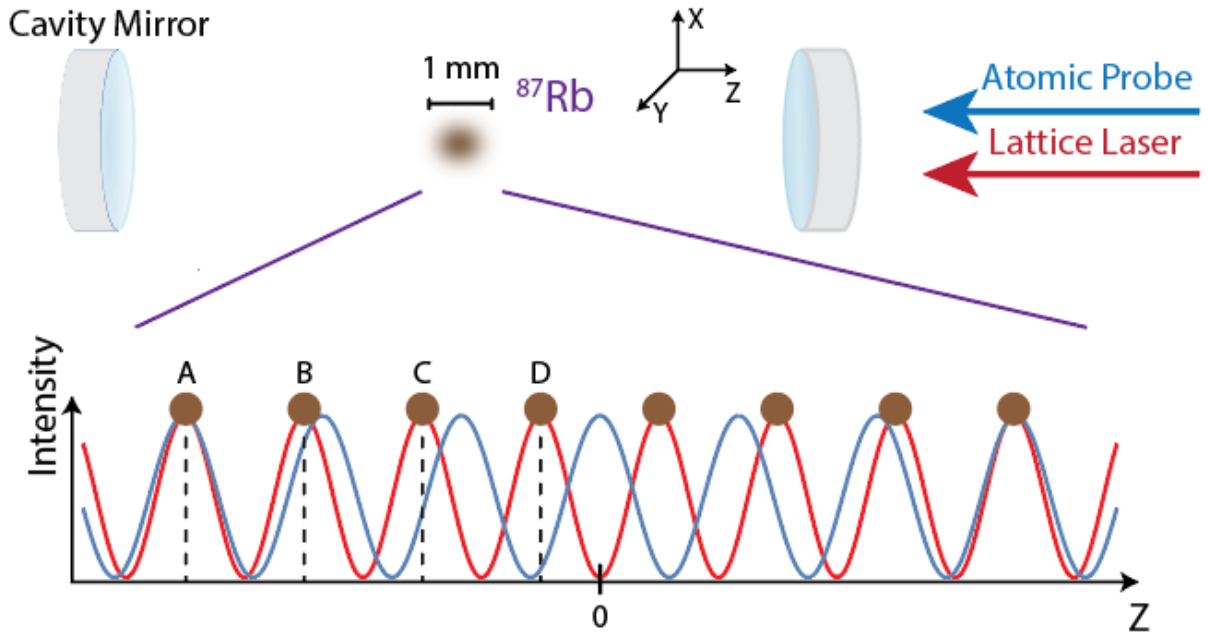


Figure 1.3: Inhomogeneous atom-cavity coupling. The lattice laser (red) is for trapping the atoms. The atomic probe (blue) is for probing the atoms. Atoms are always trapped at the maxima of the optical lattice, but not necessarily the maxima of the atomic probe, due to the difference in wavelengths between the lattice laser and the atomic probe laser, typically here 813 and 780 nm respectively.

$2\hbar k$ momentum kicks to transfer the atoms into a superposition state $|\psi\rangle = \frac{1}{\sqrt{2}}(|\downarrow, 0\hbar k\rangle + |\uparrow, 2\hbar k\rangle)$, with $\hbar$ here the reduced Planck constant, and $k$ the wavevector of the laser. The momentum transferred to the atoms causes the superposition state to move apart spatially, just as a beam splitter causes an incident field to travel along two distinct paths. A $\pi$-pulse could reverse the relative movement direction of the two atomic clouds, so that the spatially separated superposition state could re-overlap in space at some later time, just as a mirror changes the propagation direction of the incident field. The differential phase $\Delta\Phi$ is obtained from the physical quantity we want to measure, for example inertial effects such as rotations and accelerations. Here, we will consider an interferometer that is sensitive to accelerations such as gravity, as shown in the top panel of Fig. 1.6. We start with a cloud of atoms in free space. The first separation $\pi/2$-pulse transfers the atoms into a superposition state and results in spatial separation of the superposition state. After

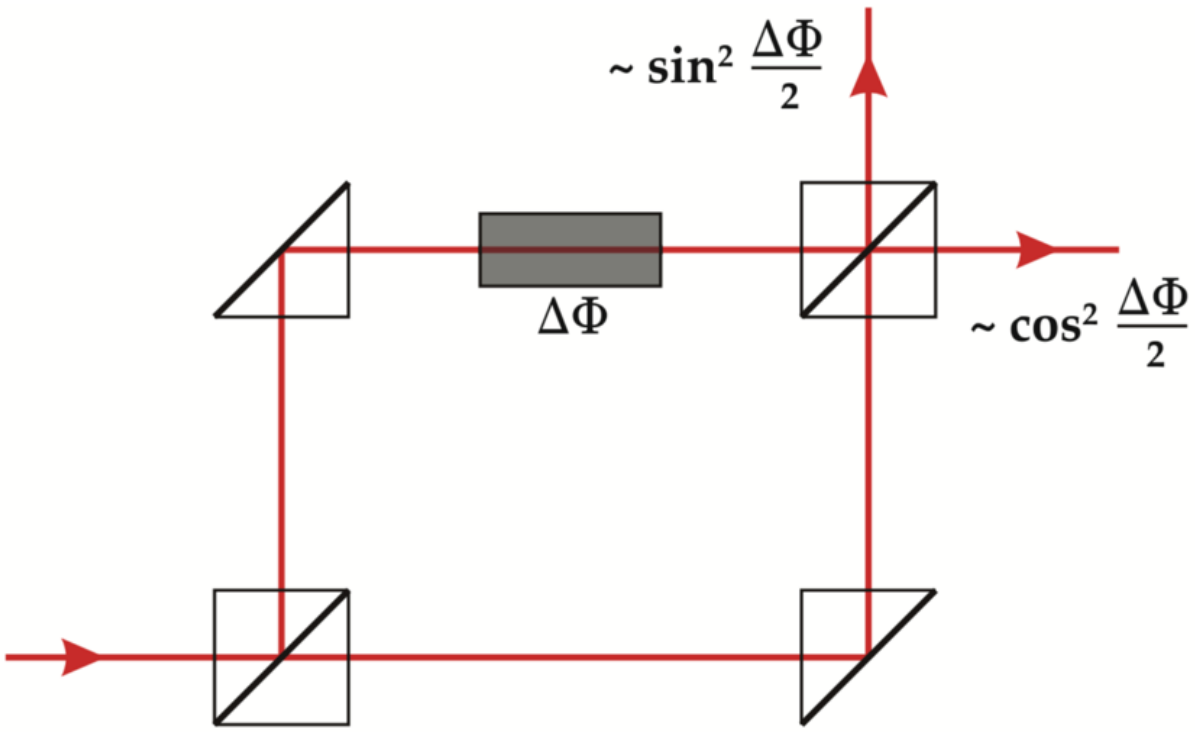


Figure 1.4: Mach-Zehnder optical interferometer

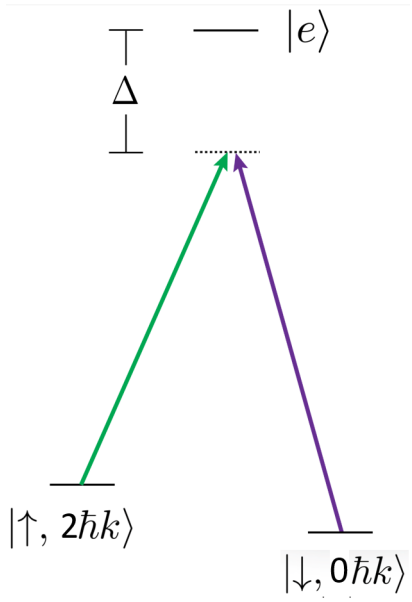


Figure 1.5: Two-photon Raman transitions

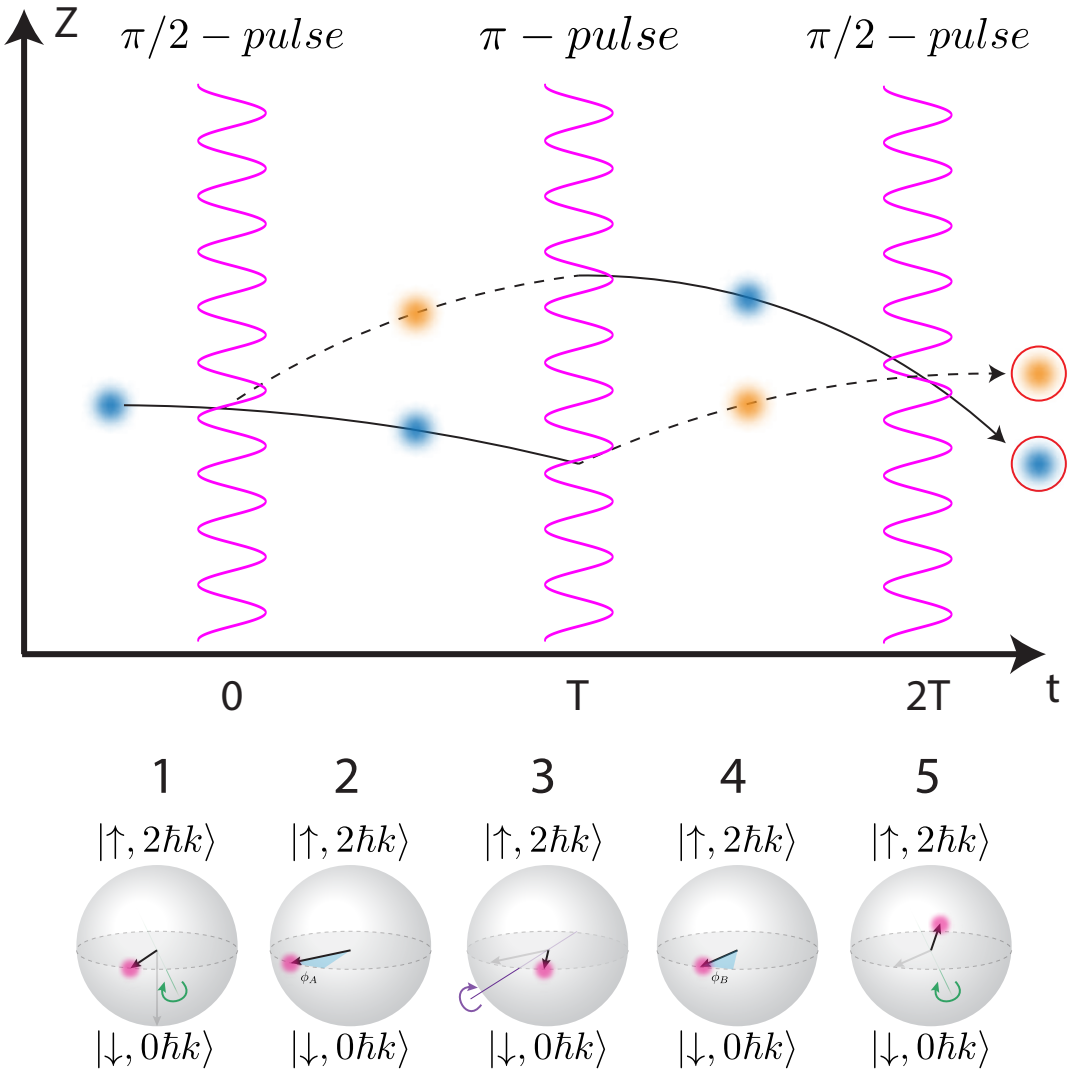


Figure 1.6: Mach-Zehnder type atom interferometer. The top panel shows how the position of the atoms evolve as a function of time t. The bottom panel maps the process to the quantum metrology paradigm discussed in Sec. 1.1. The first $\pi/2$-pulse initializes the Bloch vector on the equator. The rotation axis is indicated by the green line. Then the Bloch vector will precess through a quantum phase $\phi_A$ in time T. The $\pi$-pulse rotates the Bloch vector 180° with reference to its initial position on the equator, as indicated by the purple rotation axis. The Bloch vector will precess through another phase $\phi_B$ in time T afterwards. The final $\pi/2$-pulse will interfere the atoms, which converts information from the phase quadrature to the atom number quadrature for readout. The rotation axis is indicated by the green line. Here $\phi_B - \phi_A = \Delta\Phi$.

an evolution time of T, a mirror $\pi$-pulse is applied, which reverses the relative movement direction of the two atomic clouds so that they could recombine in space after another evolution time of

T. We use a final $\pi/2$-pulse to interfere them. The differential phase $\Delta\Phi$ arises from the different kinetic energy difference between the two clouds of atoms in the two evolution windows, because the kinetic energy is proportional to the square of the momentum. The atom numbers in $|\downarrow\rangle$ and $|\uparrow\rangle$ after interference are proportional to $\sin^2(\Delta\Phi/2)$ and $\cos^2(\Delta\Phi/2)$ respectively, with $\Delta\Phi = 4gkT^2$. In this way, we are able to build a Mach-Zehnder type atom interferometer. It is straightforward to connect the process back to the quantum metrology paradigm discussed in Sec. 1.1 after relabeling the north and south pole of the Bloch spheres with $|\uparrow, 2\hbar k\rangle$ and $|\downarrow, 0\hbar k\rangle$, as shown in the bottom panel of Fig. 1.6.

In Chapter 4, I will discuss our scheme to introduce squeezed states into atom interferometers and our progress towards building squeezed atom interferometers.

## 1.4 Doppler Cooling

Colder atomic temperature is usually favorable for quantum metrology. Doppler cooling is a widely applied cooling technique, which works by allowing the cooling laser to interact more strongly with atoms moving opposite to its propagation direction.

There are several restrictions on the Doppler cooling. First, it requires well-defined cycling transitions to work. Second, the cooling rate and equilibrium temperature is set by the linewidth of the excited state $\Gamma$. The maximum rate at which momentum can be removed from the atom is set by the maximum photon scattering rate for a saturated atom $R_{max} = \Gamma/2$. The equilibrium temperature is $T_{eq} = \hbar\Gamma/2k_B$, with $k_B$ the Boltzmann constant.

In Chapter 5, I will disccuss how these restrictions can be relaxed by adiabatic transfer and introduce a sub-Doppler cooling technique via adiabatic transfer on Raman transitions, where we achieved a final 1D temperature in $^{87}$Rb 25 times lower than the Doppler cooling limit, and the effective excited state decay rate can be modified in time, presenting another degree of freedom during the cooling process.

## 1.5 Outline of Thesis

I will devote Chapter 2 to describing the experimental apparatus, with a focus on changes from the previous generation of the experiment. In Chapter 3, I will talk about the principle and the performance of the site-dependent selection technique. I will describe our scheme for building a squeezed atom interferometer with current progress in Chapter 4. I will review a 1D sub-Doppler cooling technique via adiabatic transfer on Raman transitions in Chapter 5. I will summarize a theoretical proposal for countinuous tracking of a quantum phase, which could function as an alternative to the Ramsey sequence, focusing on a proposed implementation and technical requirements needed to implement the scheme in Chapter 6. Finally, I will conclude the thesis and discuss future directions in Chapter 7.

# Chapter 2

# Experimental Apparatus

The current generation of the experiment was reconstructed starting in late 2017. The general structure and many of the details of our current experimental apparatus are similar to the former generations and can be found from the previous theses of the group [19, 26, 9, 106]. The changes mainly happen in the parameters of the optical cavity, the way we load atoms, and the cooling procedure. I will summarize the changes and provide only a brief overview of the key experimental tools and techniques described in other theses.

## 2.1 Laser Cooling and Trapping

Our experiment always starts by cooling and trapping 200-300 thousand atoms into the $TEM_{00}$ mode of the science cavity. It usually takes three steps. First, we create a 3D MOT of several million atoms by transferring atoms from a 2D MOT. Second, we cool the atoms with polarization gradient cooling (PGC) to $10 - 20$ $\mu$K and transfer 200-300 thousand atoms into an intracavity red lattice, which is created by driving a $TEM_{00}$ mode of the science cavity with 813 nm laser light. Third, we further cool the atoms with $\Lambda$-enhanced gray molasses and 2D Raman sideband cooling in the plane transverse to the cavity axis to achieve a transverse temperature of about 1.5 $\mu$K.

### 2.1.1 3D MOT

The magneto-optical trap (MOT) is created with three pairs of counter propagating beams and a quadrupole magnetic field. The polarization and the frequency of the beams are tuned such that the atoms tend to get momentum kicks from the beams that are opposing its motion or its position from the zero point of the quadrupole field. As a result, the atoms will be cooled and trapped near the zero magnetic field point. I will refer the readers to ref. [71] for a detailed account of the physics of the MOT.

The magnetic field gradient is around 10 G/cm, with a driving current of 2.2 A. We typically have 8 mW per beam in the MOT laser and 6 mW total in the repumper laser. The waist size of the beams is about 0.5 cm. For compactness, we use lens tubes to collimate and tune the polarizations of the beams as shown in Fig. 2.1. The collimator and lens used have focal lengths of 1.1 cm and 15 cm respectively.

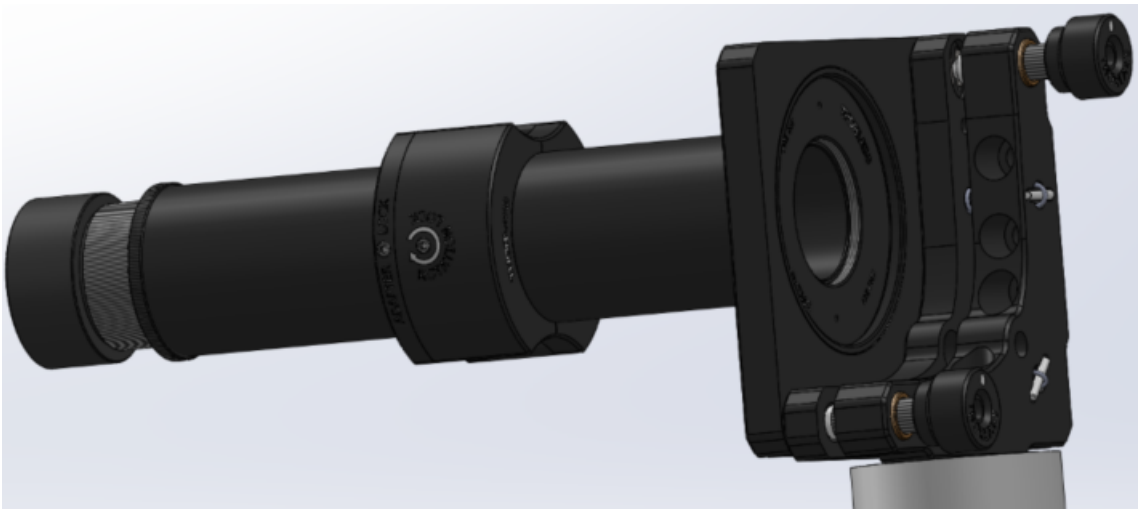

Figure 2.1: Lens tubes for collimating and tuning the polarizations of the MOT beams

### 2.1.2 PGC

Polarization gradient cooling (PGC), also known as Sisyphus cooling, works by creating a light potential in which atoms always have to climb potential hills. Every time they reach the top

of a potential hill, they are preferentially optically pumped to another ground zeeman state for which the potential now appears as the bottom of a valley with a new hill to climb, thus losing kinetic energy. I will also refer the readers to ref. [71] for a detailed account of the physics.

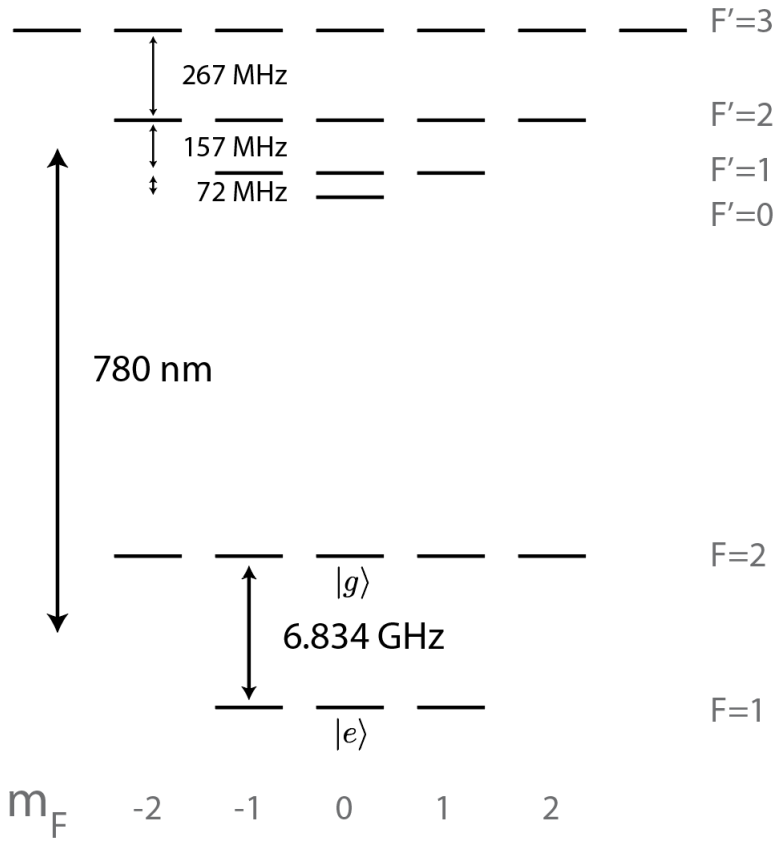


Figure 2.2: Level diagram for $^{87}$Rb D2 line

After we turn off the MOT coils and zero the magnetic field with bias coils, we could do PGC directly with our MOT beams. The detuning we use for the MOT beams is 30-40 MHz to the blue of F=2 to F'=2 transition of the $^{87}$Rb D2 line. The level diagram is shown in Fig. 2.2. The power of the MOT beams is maximized, while the power of the repumper beams is decreased by a factor of 2 to 3. We typically cool and load atoms into the optical lattice for about 30 ms. The atomic temperature after PGC is 10-20 $\mu$K with the higher temperatures for deep optical lattices with $T_{trap} = 200$ $\mu$K or more.

### 2.1.3 Λ-enhanced Gray Molasses

Λ-enhanced Gray molasses employs the principles from PGC and dark state, which is a superposition of the ground states whose excitation probability to resonant lasers is canceled out due to interference [42, 92]. We split and phase modulate the MOT laser to get a tone that is near detuned to 1-2' transition of the $^{87}$Rb D2 line. The modulation frequency is about the hyperfine splitting between F=1 and F=2 manifolds. The power of the tone from phase modulation is about 70 $\mu$W per beam. This tone and the MOT beam can be used to apply gray molasses because they are coherent. We are able to cool the atoms to about 7 $\mu$K with about 5 ms of Λ-enhance molasses.

### 2.1.4 Raman Sideband Cooling

Raman sideband cooling starts by optically pumping the atoms into a stretched state. If we could induce Raman transitions between the stretched state and another Zeeman substate whose vibrational quantum number in the optical lattice is one quanta lower, then we could keep decreasing the vibrational quantum number of the atoms by tranferring them into that substate and optically pumping them back, until the vibrational quantum number reaches 0, after which there is no longer any lower vibrational levels to transfer into and no more Raman transitions will occur [60].

Our final cooling stage is a 2D degenerate Raman sideband cooling [60] transverse to the cavity axis, i.e., in the horizontal plane. Three beams derived from the same laser subtends 128°, 116° and 116° to their neighbors. The polarization of the three beams is each 10° clockwisely rotated from vertical if viewed along the wavevector of each beam. The power in the three beams is about 55 mW, 45 mW and 45 mW respectively. The detuning of the sideband cooling laser is about 35 GHz to the red of 1-2' transition of the $^{87}$Rb D2 line. The polarization of the repumping light is a combination of $\sigma_+$ and $\pi$. One cooling cycle is defined as ramping up the 2D lattice, cooling and ramping down the 2D lattice, which takes about 2 ms. We are able to cool the atoms to about 1.5 $\mu$K in the transverse direction with two cooling cycles.

## 2.2 The Optical Cavity

The core part of our apparatus is a high-finesse optical cavity mounted in high vacuum. The SolidWorks design of the optical cavity spacer is shown in Fig. 2.3.

The cavity spacer was CNC machined from macor in the JILA machine shop. The two ceramic screws allow tuning of the position of the top mirror, and thus the free spectral range (FSR) of the cavity. The desired FSR is 10-47 MHz either red or blue detuned from the ground hyperfine spliting of $^{87}$Rb and what we currently have is 42 MHz red detuned. The reason for requiring such a detuning range can be found in Sec. 4.2.1. Our tuning procedure of the FSR is changing the position of the top mirror in the JILA clean room and then measuring the FSR in the lab, and iterating. The cavity mirrors (from FiveNine Optics) and the piezos (Piezomechanik HPCh 150/12-6/2) were glued together in the JILA clean room with Torrseal (KJLC 9530001 and 9530002). We machined an aluminum jig, as shown in Fig. 2.4 Left, to ensure that the mirrors and the piezos are concentric. The piezos and the cavity spacer were then joined with additional drops of Torrseal, assisted by a concentric-shape Delrin jig, see Fig. 2.4 Right. Kapton-dipped wires (KJLC FTAK01420) were glued to the electrodes of the piezo with silver epoxy (EPO-TEK H21D), for fine control of the cavity resonance frequency. The cavity parameters at 780 nm are summarized in Table. 2.1. By specs, the cavity linewidth at 760 nm and 813 nm are 154 kHz and 170 kHz respectively. The main difference of the new cavity is its finesse at 780 nm has been increased from about $2.5 \times 10^3$ to $1.3 \times 10^5$.

| Parameter | Value |
|---|---|
| Free spectral range | 6792(1) GHz |
| Linewidth $\kappa$ | 52.1(1) kHz |
| Mirror radius of curvature | 5.00(1) cm |
| Finesse | $1.3 \times 10^5$ |
| Cavity length | 2.21 cm |
| $TEM_{00}$ mode waist | 71.7 $\mu$m |
| Single-atom vaccum Rabi splitting g | 0.403 MHz |
| Cooperative C=$\frac{4g^2}{\kappa\Gamma}$ for $^{87}$Rb D2 transition | 2.06 |

Table 2.1: Parameters of the optical cavity at 780 nm

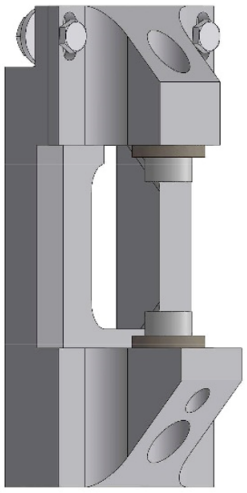

Figure 2.3: SolidWorks design of the optical cavity spacer. The spacer is designed to be made from macor. The mirrors and the piezos are already glued on, indicated by the small cylinders. The length of the cavity is tuned with the two ceramic screws at the top.

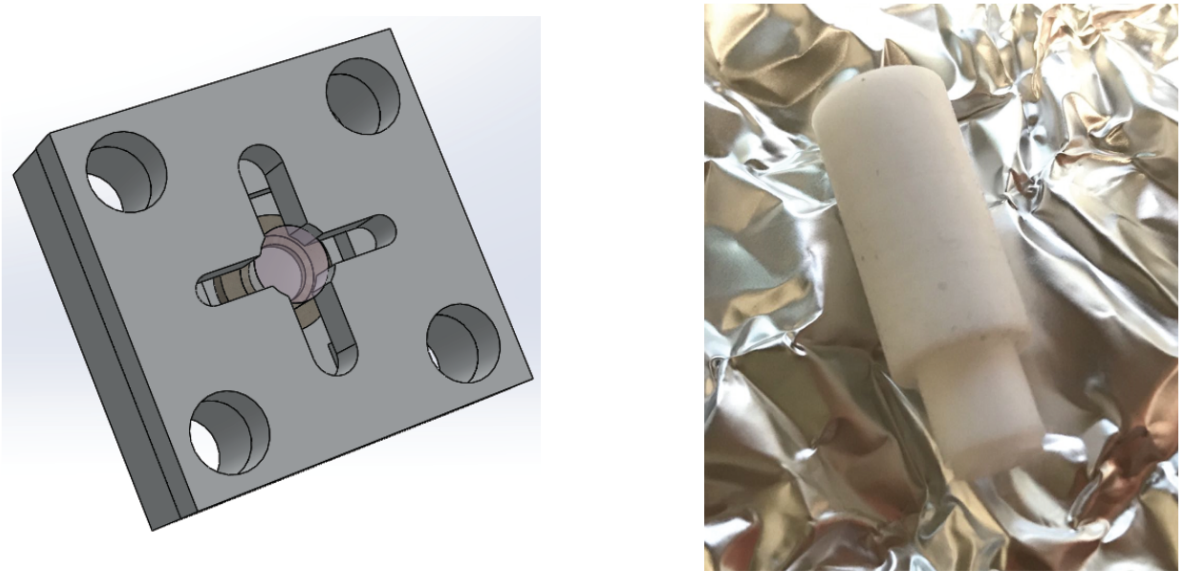

Figure 2.4: Left: SolidWorks design of jig for joining the mirrors and the piezos. Right: Picture of the jig for joining the piezos and the cavity spacer.

The cavity is mounted inside a vacuum chamber, as shown in the SolidWorks drawing Fig. 2.5, pumped with an ion pump and a titanium-sublimation pump connected to the 6-way cube at the

bottom right corner in the figure. The pressure is about $1.0 \times 10^{-8}$ torr, which limits the atomic lifetime to about 400 ms due to background collisions [53]. The vacuum pressure is limited by technical reasons from the construction of the glass cell, which I will elaborate in Sec. 2.3.

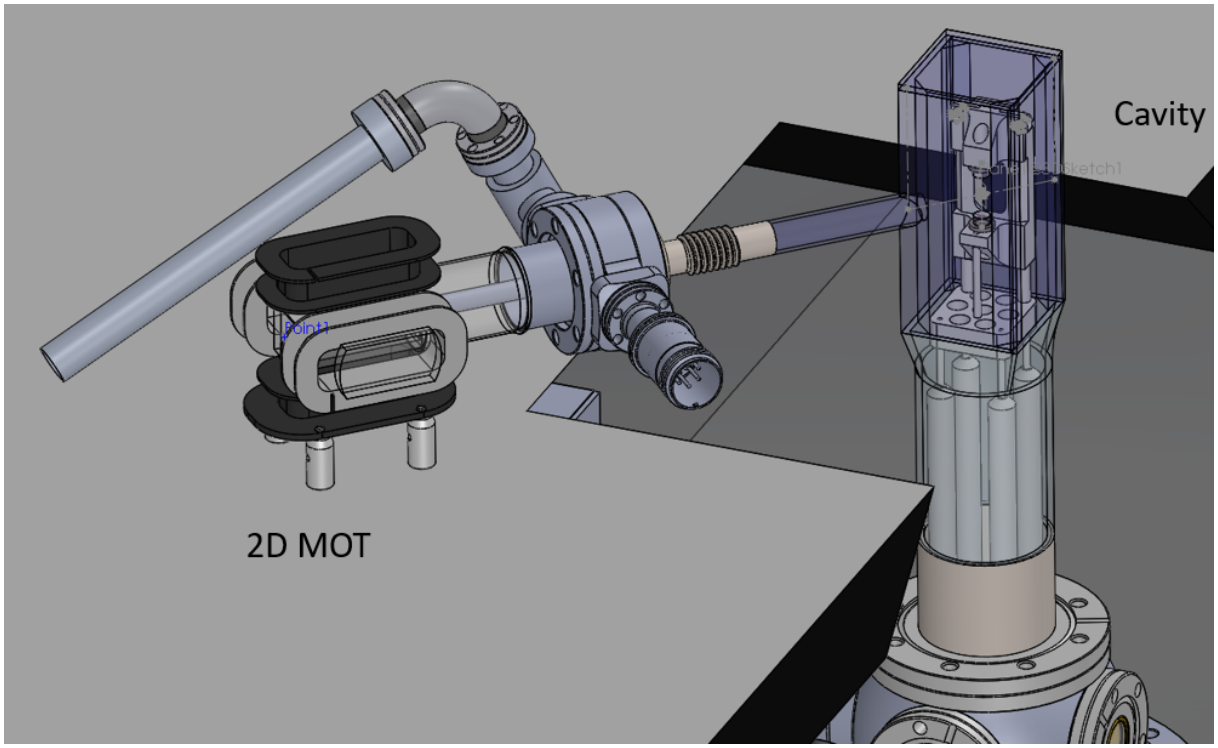


Figure 2.5: SolidWorks drawing of the vacuum system. The 2D MOT on the left-hand side is connected to the glass cell through a protrusion. The cavity is mounted inside the glass cell, which is connected to a 6-way cube at the bottom.

## 2.3 Glass Cell

The glass cell shown at the top right corner in Fig. 2.5 was made by the JILA machine shop with silicate bonding [1]. The top surface is an AR coated 2" × 2" quartz plate, and the sides are four AR coated 2" × 5" quartz plates. The reflection coefficient for the AR coated surfaces are 0.25% at 0 degree of incidence angle and 0.6% at 45 degrees for 780 nm. All quartz plates were purchased from Specialty Glass Products. Some corner support pieces, which were nominally right-angle wedges, were also added, which were custom parts from Esco Optics. The protrusion

is connected to a 2D MOT as the atomic source. The details of the 2D MOT will be discussed in Sec. 2.4.

The limitation to the vacuum pressure came from unsuccessful applications of the silicate bonding. We eventually decided to seal the leakage with torr seal (KJLC 9530001 and 9530002). However, a wrong type of torr seal was applied unfortunately, which was not able to tolerate a baking temperature of 40°C.

## 2.4 Atomic Source: 2D MOT

In the previous generation of the experiment, atoms were loaded into a 3D MOT from a background rubidium vapor produced by a heated ampoule of rubidium attached to the vacuum chamber. We decided to switch to a 2D MOT as the atomic source in the current generation to protect the high finesse optical cavity, whose finesse has been increased by more than 50 fold.

The sideview of the SolidWorks drawing of the 2D MOT could be found in Fig. 2.6a. Fig. 2.6b shows the real parts made and assembled by the JILA machine shop. We could disassemble the 2D MOT setup with the two-way crossing as a reference point, which is shown in Fig. 2.6c. The righthand side of the two-way crossing in Fig. 2.6a was a stainless steel to pyrex adaptor (Larson SP-150-F2) fused with a pyrex cuvette (Fireflysci, CM1484B, dimensions 25 mm $\times$ 25 mm $\times$ 75 mm). The lefthand side was a zero length 2-3/4" to 1-1/3" CF reducer with the bore sealed and welded to a stainless steel tube (McMaster-Carr 8457k55), whose OD was 3/8". The other side of the tube was welded to a polished round copper disk, which would work as a mirror to allow axial cooling for the 2D MOT. A tiny hole of about 0.8 mm diameter was drilled at the center of the copper disk to allow atoms from the 2D MOT to be transferred to the 3D MOT, and provide differential pumping. The top 1-1/3" port was connected to a feedthrough (KJLC IFTAG065102) to drive the getter and dispensers mounted on a macor disk as shown in Fig. 2.6d. The dispenser is the rubidium source, and the getter is like a mini pump. The macor disk was held fixed on the stainless steel tube with retaining rings (McMaster-Carr 98410A665). The bottom port was later connected to a Rb chunk (ESPI, Rb 1 gram breakseal ampoule, 3N+ purity) as a backup atomic source, as

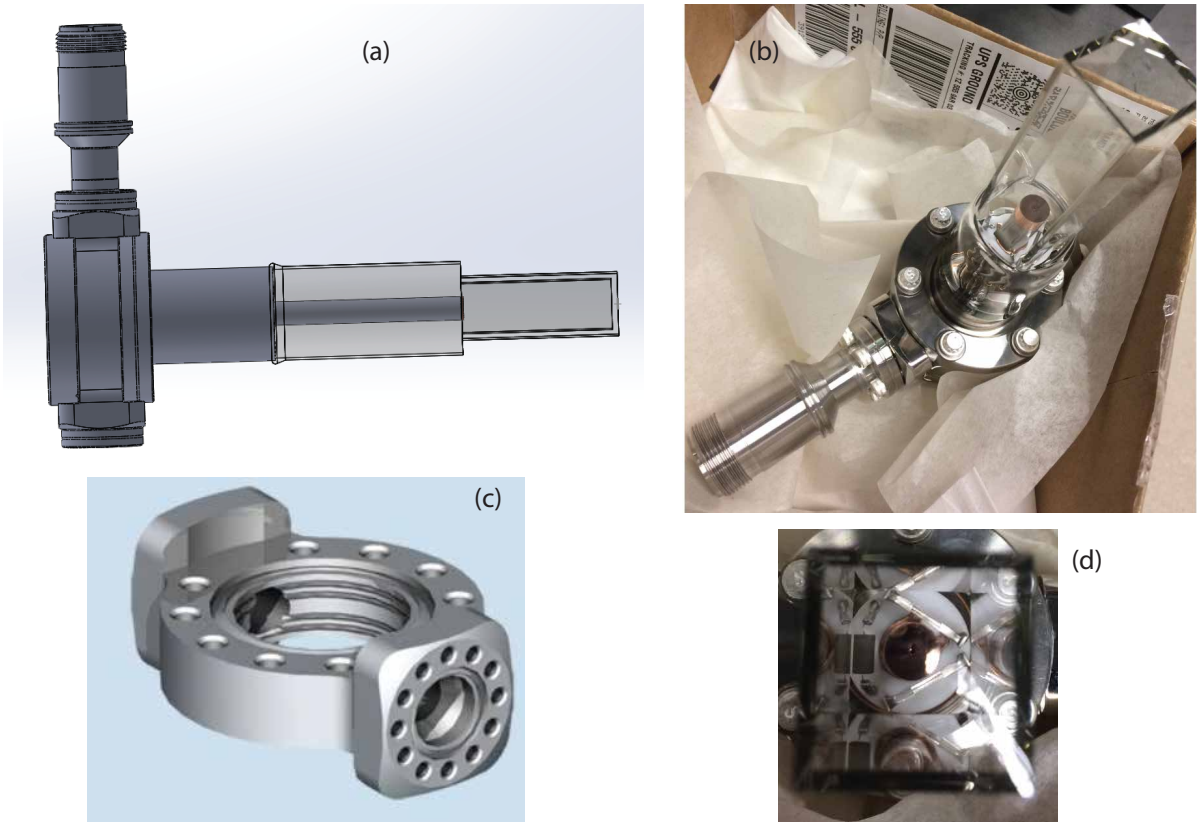


Figure 2.6: 2D MOT cell (a) Sideview of the SolidWorks drawing of the 2D MOT cell. From right to left are pyrex cuvette, pyrex to 2-3/4" CF adapter, two-way crossing, and zero-length 2-3/4" to 1-1/3" CF reducer. The stainless steel tube which we can see through the pyrex adapter is welded to the zero-length reducer. The shiny copper disk in (b) is on the other side of the tube. The 2D MOT will be formed in the pyrex cuvette. The atoms from the 2D MOT will be pushed through a tiny hole on the copper disk, the stainless steel tube and the protrusion shown in Fig. 2.5, and form a 3D MOT in the glass cell. (b) 2D MOT cell made and assembled by the JILA machine shop. (c)Two-way crossing from Kimball physics (KPI 53-650010). (d) Two Rb dispensers (SAES 5G0125) and one getter (SAES S5K0088) mounted on a macor disk.

shown in Fig. 2.5.

The 2D MOT coils were made with 3d-printed frames as shown in Fig. 2.5. The typical magnetic field gradient applied was 15-20 Gauss/cm at a current of about 1.2 A. Our optics layout drawing is shown in Fig. 2.7. The typical power out of the fiber couplers for MOT and Repumper beams is 100 mW and 5 mW respectively.

An image of the string-like 2D MOT is shown in Fig. 2.8. With 2.9 A of dispenser current,

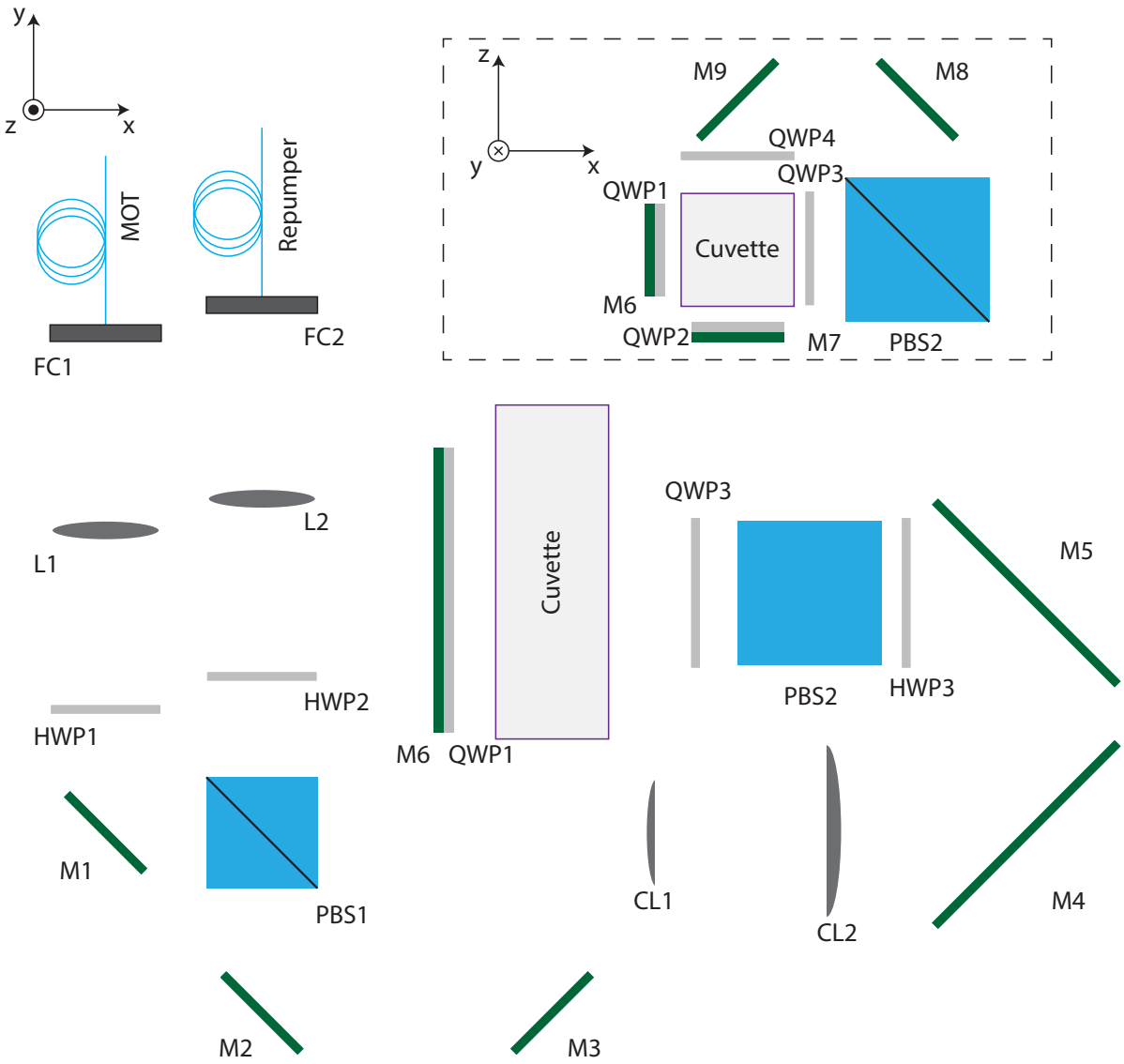


Figure 2.7: Optics layout drawing for the 2D MOT. FC1 and FC2 are fiber couplers. L1 and L2 are convex lenses with focal length 20 cm. The beams have a collimated diameter of 1.5 cm after theses lenses. HWP1-HWP3 are half waveplates. QWP1-QWP4 are quarter waveplates. M1-M8 are mirrors. PBS1 and PBS2 are polarized beam splitters. The beam reflected by PBS2 goes in the z-direction. CL1 and CL2 are cylindrical lenses, which work together to magnify one dimention of the beam to 3.5 cm in diameter. The cuvette is where the 2D MOT is located. The 3D MOT is in the far y-direction, which is not shown in the layout drawing.

and 2.3 A of getter current, we were able to load a 3D MOT of about $1.3 \times 10^7$ atoms with 1/e load time of 1.22 s, as shown in Fig. 2.9, from which we could estimate an atomic flux of about

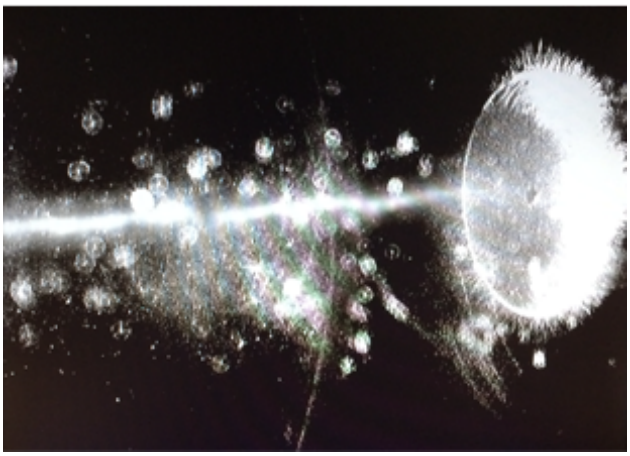

Figure 2.8: 2D MOT image. The shiny string is the 2D MOT formed inside the pyrex cuvette. The disk on the right-hand side is the copper disk. The atoms in the 2D MOT will be pushed through the center hole and eventually sent to the glass cell to form a 3D MOT.

$1.07 \times 10^7$ atoms/s. Our result is comparable to a typical 3D MOT size of about $2 \times 10^7$ atoms [91].

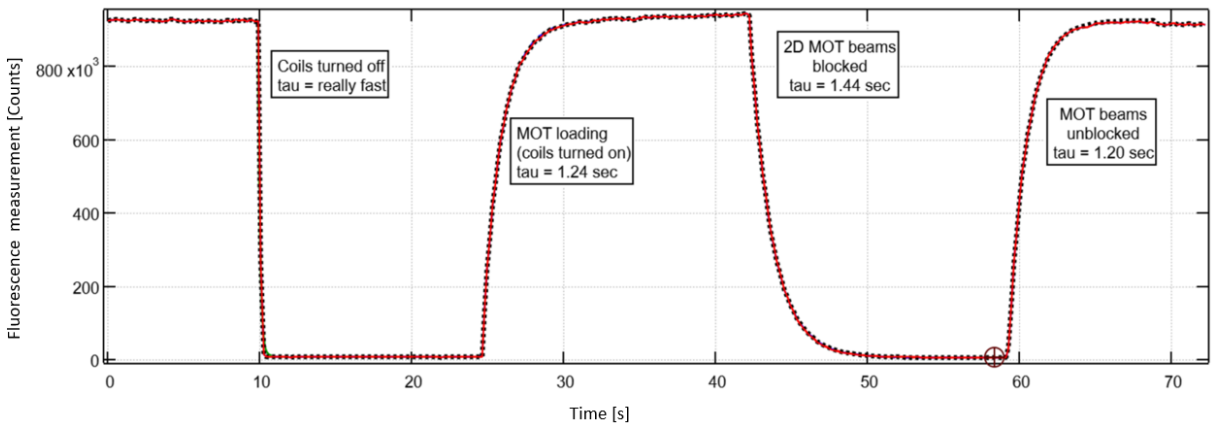


Figure 2.9: Loading curve of the 3D MOT from 2D MOT. The horizontal axis is time in second, and the vertical axis is fluorescence counts of the 3D MOT. We start with a 3D MOT in steady state. The coils are turned off at about 10 s, and back on at about 25 s to reload the 3D MOT. From the loading curve, we fit a 1/e loading time of about 1.24 seconds. At about 42 s, the 2D MOT beams are blocked. They are unblocked at about 60 s to reload the 3D MOT. The 1/3 loading time is fitted to be abobut 1.2 seconds. We report a typical loading time of 1.22 seconds which is the average of the two measured values of the loading time.

## 2.5 Frequency Stabilization of Lasers and Cavities

The experiment relies on stabilizing the frequencies of various lasers and optical cavities. Here, I give a short summary of how this is accomplished. In all, there are two cavities and nine lasers.

One cavity is a passive reference cavity which has a typical resonance frequency drift rate of about $50 - 100$ MHz/hour. The other cavity is the high finesse science cavity.

The nine lasers are listed in Table. 2.2

| Name | Wavelength | Function |
|---|---|---|
| Reference laser | 780 nm | Frequency reference, locked to $^{85}$Rb 3-4' transition |
| MOT laser | 780 nm | Create the 2d and 3d MOT, PGC and optical pumping |
| Repumper laser | 780 nm | Create the 2d and 3d MOT, PGC and optical pumping |
| Atomic probe | 780 nm | Probe the cavity resonance |
| Cavity probe | 780 nm | Common mode cancellation of the cavity frequency noise |
| Raman laser | 780 nm | Drive intracavity Raman transitions |
| Red lattice laser | 813 nm | Create intracavity red lattice |
| Blue lattice laser | 760 nm | Create intracavity blue optical dipole trap [28] |
| Sideband cooling laser | 780 nm | Drive Raman sideband cooling in the transverse plane |

Table 2.2: List of lasers

The science cavity is Pound-Drever-Hall (PDH) [7] locked to the blue lattice laser, whose 1st order sideband, created by an EOM modulated at 5-9 GHz, is PDH locked to the passive reference cavity.

The red lattice and the cavity probe are both PDH locked to the science cavity.

The reference laser is locked to a Rb vapor cell. Both MOT laser and repumper laser are beatnote (BN) locked to the reference laser with phase-frequency detectors (PFDs).

The Raman laser is BN locked to the 7th sideband of the cavity probe, and is about 95 GHz detuned from the cavity probe. The sidebands of the cavity probe is created by phase modulating with modulation frequency of 13.6 GHz.

The atomic probe is either locked to the 12th sideband of the cavity probe or to the science cavity, controlled by a high-speed switch (Minicircuits ZASWA-2-50DR+). When locking atomic

probe to the sideband of the cavity probe, their detuning is more than 100 GHz.

The sideband cooling laser is free running, since we just need to keep it 10s of GHz red detuned to F=1 to F'=2 transition of the $^{87}$Rb D2 line.

# Chapter 3

## Site-dependent Selection of Atoms for Homogeneous Atom-cavity Coupling

In this chapter, I will talk about a selection technique to achieve homogeneous atom-cavity coupling, and how the technique helps suppress optomechanically-induced oscillations. I will also discuss how different factors could affect our experiment and present some of the technical details.

### 3.1 Introduction

Atomic ensembles in optical cavities have become a versatile and powerful platform for creating atomic entanglement [51, 27, 44], generating superradiant lasers [80, 10], synthesizing quantum matter [23], interacting many-body pseudo-spin and related systems [79, 31] and precision measurement [76, 82]. As I explained previously in Sec. 1.2, the inhomogeneity in the coupling of individual atoms to the cavity is brought about by the standing wave nature of the cavity modes and the incommensurateness between the atomic probe and the lattice laser. The inhogeneous coupling reduces the effective atom number [52], creates dephasing in driven systems [75], and brings about optomechanically-induced oscillations [27]. What motivates us to develop the selection technique is that the optomechnically-induced oscillations were believed to be the primary limitation to the degree of spin squeezing we could create. It will potentially benefit the whole cavity-qed community as well.

I will review how we created a spin squeezed state (SSS) with quantum non-demolition (QND) measurement, how the optomechanical effects were excited, and how it could set a limit on spin squeezing. I will also briefly introduce some alternative solutions to the inhomogeneous coupling

problem.

### 3.1.1 Optomechanically-induced Oscillations in QND Measurement

#### 3.1.1.1 Creating Spin Squeeing with QND Measurement

As discussed in Sec. 1.1, a two-level system is like a spin-1/2 particle. The quantum states of N two-level systems can be represented in the Dicke basis $|J, m_J\rangle$, with $J = N/2$ the total spin, and $m_J$ the spin projection along z. A coherent spin state (CSS) parameterized with azimuthal angle $\phi$ and polar angle $\theta$ can be represented in the Dicke basis, as shown in Eq. (3.1) [43],

$$|\theta, \phi\rangle = \sum_{m=-J}^{J} c_m(\theta) e^{-i(J+m)\phi} |J, m\rangle , \tag{3.1}$$

with $c_m(\theta)$ subjected to a binomial distribution peaked around $\theta$, described by Eq. (3.2),

$$c_m(\theta) = \sqrt{\frac{(2J)!}{(J+m)!(J-m)!}} \cos^{J-m}(\theta/2) \sin^{J+m}(\theta/2). \tag{3.2}$$

In the limit $2J$, $2J\sin(\theta/2)$ and $2J\cos(\theta/2)$ are large, the binomial distribution can be approximated by the Gaussian distribution, as shown in Eq. (3.3),

$$|c_m(\theta)|^2 \approx \frac{1}{\sqrt{2\pi(2J\sin^2(\theta/2)\cos^2(\theta/2))}} e^{\frac{(J+m-2J\cos^2(\theta/2))^2}{2\times(2J\sin^2(\theta/2)\cos^2(\theta/2))}}. \tag{3.3}$$

The standard deviation of the Gaussian distribution in Eq. (3.3) is $\sqrt{N}/2$, for $J = N/2$ and $\theta = 90°$, so the corresponding angular uncertainty in $\theta$ is $\Delta\theta = 1/\sqrt{N}$ radians. For a CSS, we also have $\Delta\phi = \Delta\theta$.

If we could project the CSS onto the Dicke basis with a measurement, the standard deviation of the distribution obtained after the measurement will be determined by the measurement noise. Only if the measurement noise is smaller than $\sqrt{N}/2$ in atom number quadrature, we are able to create a SSS. We call this measurement a QND measurement because we preserved the coherence and thus the quantum nature of the state. I will explain how we perform the measurement in the Dicke basis below.

Consider the hyperfine F=1 and F=2 states in the $5^2S_{1/2}$ manifold of $^{87}$Rb, where $F = I + J$, with $I$ the quantum number for nuclear spin, and $J$ for the total angular momentum. The two states are labeled as $|\downarrow\rangle$ and $|\uparrow\rangle$ and they are separated by $\omega_{HF} \approx 2\pi \times 6.8$ GHz. The transition wavelength from $5^2S_{1/2}$ to $5^2P_{3/2}$, which is labeled as $|e\rangle$, is about 780 nm, as shown in Fig. 3.1 Left.

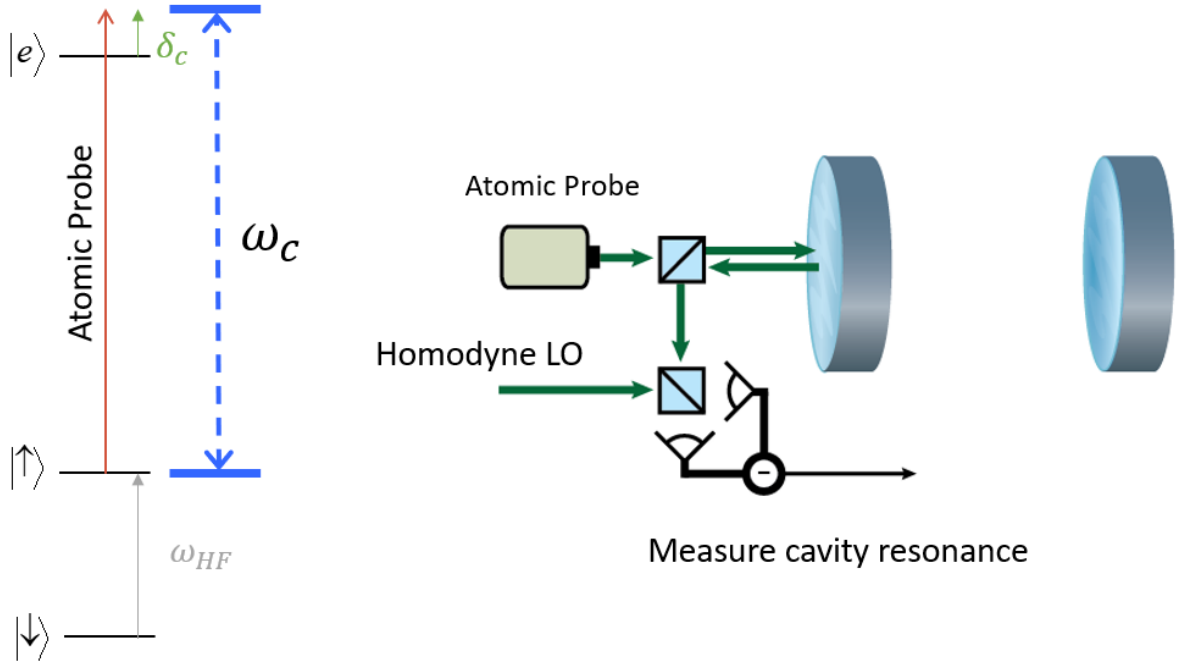


Figure 3.1: Left: Simplified $^{87}$Rb level diagram. Right: Simplified experimental diagram. The cavity resonance is measured by homodyne detection.

If we tune the cavity near resonance to $|\uparrow\rangle \rightarrow |e\rangle$ transition, the photons in the cavity are allowed to exchange between the cavity mode and the atoms in $|\uparrow\rangle$. $\omega_c$ in Fig. 3.1 indicates the cavity resonance, and $\delta_c$ is typically 400-500 MHz.

The coupling between the atoms in $|\uparrow\rangle$ and cavity can be treated as two coupled harmonic oscillators in the low atomic excitation limit, with Holstein-Primakoff approximation. The Hamiltonian is [21]

$$\hat{H} = \hbar\delta_c \hat{c}^\dagger \hat{c} + \hbar\sqrt{N_\uparrow} g(\hat{a}\hat{c}^\dagger + \hat{a}^\dagger \hat{c}), \tag{3.4}$$

where $\hat{a}^\dagger$ and $\hat{a}$ are creation and annihilation operators for the atoms with $\hat{a}^\dagger$ creating one atom in the excited state, and $\hat{a}$ destroying one atom in the excited state, $\hat{c}^\dagger$ and $\hat{c}$ are creation and annihilation operators for the cavity photons, $N_\uparrow$ is the number of atoms in $|\uparrow\rangle$, and $2g$ is the single atom vacuum Rabi frequency.

The eigenfrequencies of the Hamiltonian in Eq. (3.4) are

$$\omega_\pm = \frac{\delta_c \pm \sqrt{\delta_c^2 + (2g\sqrt{N_\uparrow})^2}}{2}. \tag{3.5}$$

In the large $\delta_c$ limit, the two eigenfrequencies correspond to one cavity-like mode and one atom-like mode. The cavity-like mode is shifted by the interaction with atoms in $|\uparrow\rangle$ by an amount $\frac{g^2 N_\uparrow}{\delta_c}$. By probing the cavity resonance change with homodyne detection, as indicated by Fig. 3.1 Right, we are able to learn how many atoms are in $|\uparrow\rangle$, without collapsing individual atomic wavefunctions. This is exactly performing measurements in the Dicke basis.

Lastly, the coupling strength of the $i$-th atom in $|\uparrow\rangle$ is $g_i$ due to inhomogeneous coupling between the atoms and the cavity. The measured $N_\uparrow$ and the coupling strength $g$ for calculating the dressed cavity resonance shift are effective quantities, which are related to the total number of atoms in $|\uparrow\rangle$ $N_{\uparrow,t}$ and the peak coupling strength for atoms sitting at the antinodes of the atomic probe $g_0$ as $N_\uparrow \approx \frac{2}{3}N_{\uparrow,t}$ and $g^2 \approx \frac{3}{4}g_0^2$. These relations are chosen to preserve the average coupling strength and the projection noise [27, 52, 20, 11, 66].

#### 3.1.1.2 Optomechanically-induced Oscillations

Fig. 3.2 explains the cause of the optomechanically-induced oscillations. All atoms are initially trapped at the maxima of the optical lattice. Another potential is developed when we turn on the atomic probe. The gradient of the potential is force, so the equilibrium position of the atoms in the optical lattice will be displaced by an amount that depends on the force induced by the atomic probe, if they are not trapped near the extrema of the atomic probe. The displacement will change the dressed cavity resonance because the atom-cavity coupling is changed.

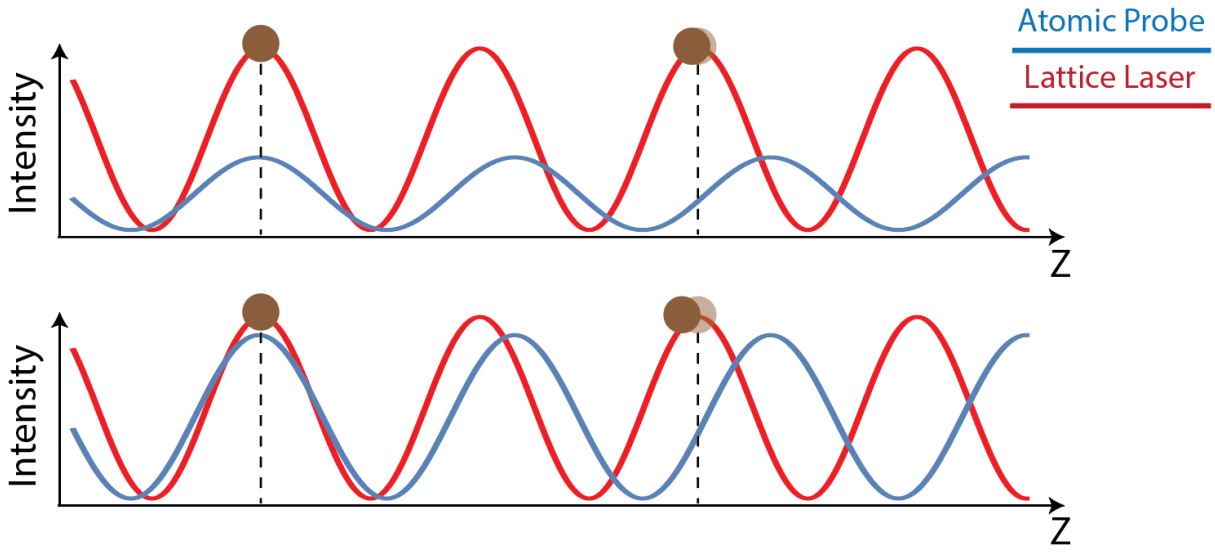


Figure 3.2: Cause of optomechanically-induced oscillations

We could expect an oscillation of the dressed cavity resonance at the axial trapping frequency of the optical lattice whenever the power in the atomic probe is changed. This oscillation will reduce the precision of the QND measurement of the cavity resonance.

Shown in Fig. 3.3 was the atomic probe induced oscillation of the dressed cavity resonance (red trace) in the previous spin squeezing generation experiment of our lab [27]. The oscillation could be partially canceled with a staggered turn-on sequence. An initial half-power turn-on of the atomic probe induced the oscillation, while the second full-power turn-on 2.5 $\mu$s (1/4 of an axial oscillation period) later coherently canceled out the initial axial oscillation. This staggered turn-on sequence suppressed the oscillation significantly, but only improved the optimal squeezing by an estimated 0.6 dB.

The optomechanical effect was still the primary limitation of the amount of squeezing available. Mitigation of this effect would be crucial for creating more squeezing.

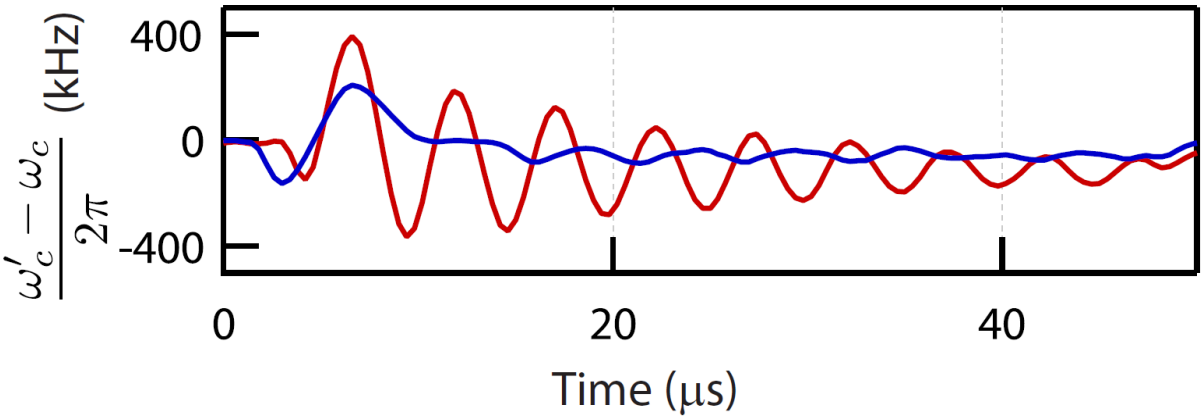


Figure 3.3: Atomic probe induced oscillations partially cancelled by a staggered turn-on sequence. $\omega_c$ and $\omega_c'$ are the original and dressed cavity resonances. The oscillations are fully present with no kick (red, 43 traces averaged) during a 40 $\mu$s measurement, but greatly reduced by a half-power 2.5 $\mu$s kick (blue, 30 traces averaged). The 2.5 $\mu$s kick length corresponds to a quarter of the axial trap oscillation period. There is an 80 MHz offset subtracted from the vertical axis. Reprinted from ref. [27].

### 3.1.2 Alternatives for Achieving Homogeneous Atom-Cavity Coupling

There have been previous efforts to circumvent the issue of inhomogeneous coupling. One way is to utilize a commensurate trapping wavelength, such as $\lambda_l = 2\lambda_p$ [51, 64], with $\lambda_l$ the trapping wavelength, and $\lambda_p$ the probing wavelength, as illustrated in Fig. 3.4a. However, the wavelength of the trapping laser could be a degree of freedom we want to reserve for tuning, for example, to engineer state-dependent traps and magic-wavelength traps [57, 68, 48]. Tightly confining magnetic traps have also allowed atoms to be loaded into single lattice sites, requiring a high atomic density at fixed total atom number. If localizing the atoms is undesired, one can also allow the atoms to move along the cavity axis to time-average away the standing-wave inhomogeneity [28], as shown in Fig. 3.4c. The flat axial potential is engineered by phase modulating the lattice laser with modulation frequency equals the FSR of the cavity, injecting the $\pm$1-order sideband of the lattice laser into the cavity along with the carrier, and tuning the relative intensity. Finally, one can use ring-cavity geometries with running waves [95], for example, Fig. 3.4b, but this adds complexity, results in larger mode volumes, and breaks the degeneracy between polarization modes of the cavity.

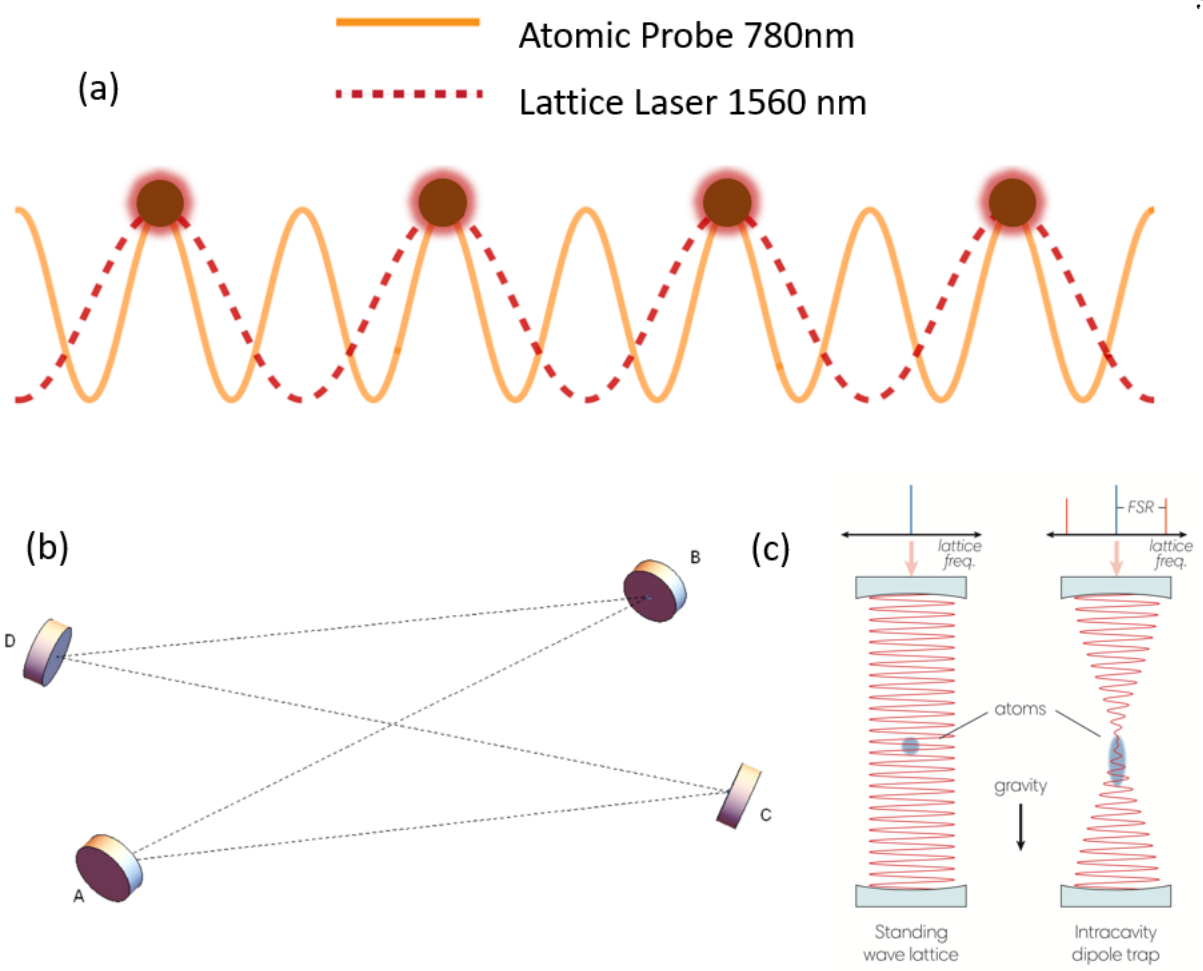


Figure 3.4: Alternatives for achieving homogeneous atom-cavity coupling. (a) Commensurate trapping wavelength. (b) Ring cavity. (c) Effective intracavity dipole trap to allow the atoms to move and time-average their coupling.

Here we demonstrate a method to obtain more homogeneous atom-cavity coupling by initially loading atoms into thousands of lattice sites and then using a spectroscopic method to select and keep only those atoms at lattice sites with near maximal coupling to the probe cavity mode. While this approach involves discarding atoms, it has favorable scaling in that the degree of homogeneity is expected to scale quadratically with the number of retained atoms.

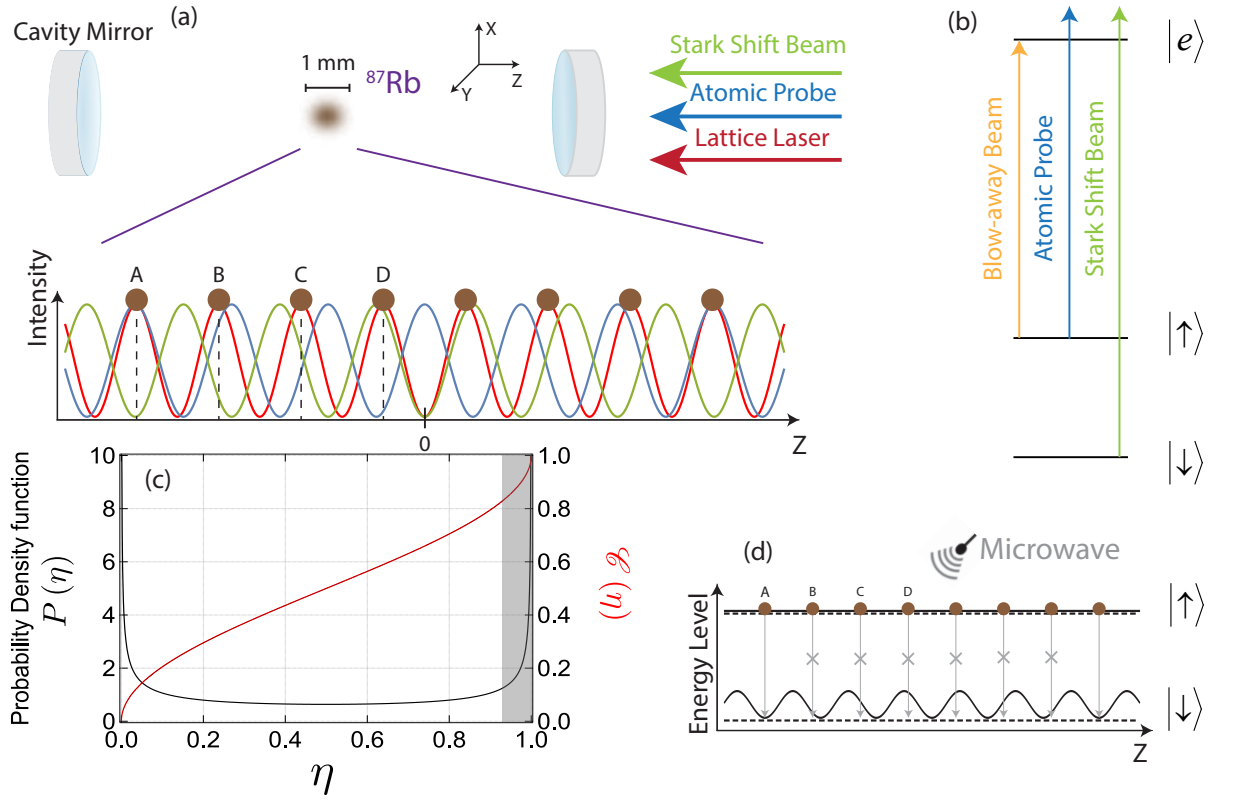


Figure 3.5: Experimental setup and working principle. (a) Three lasers are sent into the cavity for trapping (lattice laser), probing (atomic probe) and dressing (Stark shift beam) the atoms. The atoms are always trapped at the maxima of the optical lattice. The intensity of the atomic probe and the Stark shift beam the atoms see are site dependent and opposite near the center of the cavity. (b) Level diagram of $^{87}Rb$, and the relationship between the lasers and energy levels. (c) Atomic probability distribution $P(\eta)$ as a function of $\eta = g^2/g_0^2$ for atoms trapped in the optical lattice without selection. The gray region indicates the atoms we want to select. The cumulative distribution function $\mathscr{C}(\eta) = \int_0^1 P(\eta)d\eta$ is also presented to confirm that $P(\eta)$ is normalized. (d) Principles of the selection. The dashed lines are the original energy levels without the presence of the Stark shift beam. The solid lines are the Stark-shifted energy levels. Atoms with unchanged microwave transition frequencies are maximally coupled to the atomic probe, and can be selected with microwave $\pi$-pulses at well tuned frequencies.

## 3.2 Experimental Setup and Working Principle

To further explain the problem and our approach, let us consider our experimental system in which initially $N \approx 10^5$ $^{87}$Rb atoms are trapped at the center of the cavity using an intracavity optical lattice at $\lambda_L = 813$ nm. The atoms are trapped at antinodes of the lattice light as shown in Fig. 3.5a red. Two additional lasers, the atomic probe and Stark shift beams, can be injected

into the cavity at or near resonance with other longitudinal modes of the cavity. Their functions in the spectroscopic selection process will be returned to shortly.

A simplified level diagram is shown in Fig. 3.5b. The two primarily-relevant hyperfine ground states here are the magnetic-field insensitive states $|\uparrow\rangle \equiv |F = 2, m_F = 0\rangle$ and $|\downarrow\rangle \equiv |F = 1, m_F = 0\rangle$ with a splitting of 6.834 GHz. Only the optical excited state $|F' = 3, m_F = 0\rangle$ denoted by $|e\rangle$ is shown for simplicity with transition wavelengths $\lambda_a \approx 780$ nm.

Here, we wish to enhance the homogeneity of the coupling of the atoms to the atomic probe. The atomic probe and an associated longitudinal cavity mode is typically detuned by $\Delta_p/2\pi = 700$ MHz from resonance with the $|\uparrow\rangle$ to $|e\rangle$ transition. The atomic-probe can then be used to measure the shift in the frequency of the cavity mode by an amount $\delta_c \approx \left(g_0^2/\Delta_p\right) \Sigma_i^N \cos^2\left(2\pi z_i/\lambda_p\right)$ [21] where $2g_0$ is the single-particle vacuum rabi frequency, atom $i$'s position along cavity axis relative to the cavity mid-plane is $z_i$, and only atoms in $|\uparrow\rangle$ are implicitly included in the sum. This same frequency shift has been used previously to realize entanglement generation via collective measurements, cavity-optomechanics, and cavity-mediated spin-spin interactions [51, 27, 79, 15]. The goal is then to select atoms at antinodes of the probe mode (i.e. $\cos^2\left(2\pi z_i/\lambda_p\right) \approx 1$), and remove all other atoms from the cavity mode. To reduce notational complexity, we define the coupling $g_i$ of atom $i$ relative to that of a maximally coupled atom as $\eta_i \equiv \left(g_i/g_0\right)^2$.

In conceptual analogy to what is done in NMR imaging by applying magnetic field gradients [85, 8], here we engineer a spatially-dependent shift of the $|\downarrow\rangle$ to $|\uparrow\rangle$ transition frequency $\omega_{\uparrow\downarrow} \rightarrow \omega_{\uparrow\downarrow} + \delta\left(z\right)$. The frequency shift is generated by an AC Stark shift $\delta\left(z_i\right) = \delta_s \sin^2\left(2\pi z_i \lambda_s\right)$ that is induced by injecting light into a cavity mode one free spectral range away from that of the probe mode. Adjacent longitudinal modes have the desired opposite symmetry. The free spectral range of the cavity 6.791 GHz is close to the hyperfine splitting $\omega_{\uparrow\downarrow}$, so that the Stark shift mode is detuned by approximately $\Delta_s/2\pi \approx 900$ MHz from the $|\downarrow\rangle$ to $|e\rangle$ transition, leading primarily to a Stark shift of the state $|\downarrow\rangle$. Because of the small frequency difference between the probe mode and the Stark shift mode, the standing-waves are to good approximation locally out of phase near the center of the cavity where the atoms are located.

To select atoms with peak coupling to the probe mode, we begin by optically pumping atoms into $|\uparrow\rangle$, applying the spatially-dependent Stark shift beam, and then applying microwaves for $t_m \approx 200$ to 250 $\mu$s at frequency $\omega_m = \omega_{\uparrow\downarrow} + \delta_m$ to perform a $\pi$-pulse for atoms whose transition frequency is resonant with the microwaves. The bandwidth of transition frequencies that undergo the spin flip is set by the Rabi frequency $\Omega_m$ of the applied microwaves. Atoms that are not flipped to $|\downarrow\rangle$ are then removed from the trap using a radiation pressure force from the blow away beam that is tuned to resonance with the $|\uparrow\rangle$ to $|e\rangle$ transition and applied for 100 $\mu$s. If the microwaves are resonant with the unshifted transition frequency, i.e., $\delta_m = 0$, then atoms at nodes of the Stark beam will remain in the trap. We depicted the selection process in Fig. 3.5d, where atom A will survive after the blow-away stage, while atom B, C and D will be killed. We also plot the probability density of atoms as a function of $\eta$ in Fig. 3.5c. The grey region indicates the selection bandwidth set by $\Omega_m$.

The probability that an atom with a given coupling is selected is simply given by the Rabi spin flip probability as

$$F\left(\eta_c, \eta, \Omega_m, \delta_s\right) = \frac{\Omega_m^2}{\Omega_m^2 + \left(\left(\eta_c - \eta\right)\delta_s\right)^2} \sin^2\left(\frac{\pi}{2}\frac{\sqrt{\Omega_m^2 + \left(\left(\eta_c - \eta\right)\delta_s\right)^2}}{\Omega_m}\right), \tag{3.6}$$

where the microwave detuning is parameterized as $\eta_c = \delta_m/\delta_s$. In Fig. 3.6c we show the spin flip probability for a given coupling $\eta_i$ for different ratios of $\Omega_m/\delta_s$ at $\eta_c = 0$.

## 3.3 Theory Plots for Scaling in Selection

In Fig. 3.6a, we show the theoretical trade off between the fraction of of atoms retained after selection $N_s/N$ and the ensemble averaged coupling $\bar{\eta} \equiv \langle \eta_i \rangle$ for one, two, three and four selections. In Fig. 3.6b, we show the trade off versus the fractional standard deviation of the coupling about the mean $\Delta\eta/\bar{\eta} \equiv \sqrt{\langle \eta^2 \rangle - \bar{\eta}^2}/\bar{\eta}$. In this model, the microwave detuning is $\delta_m = 0$ and the atomic ensemble's axial spatial extent is much larger than the differential wavelength $\lambda_d^{-1} = \left|\lambda_l^{-1} - \lambda_p^{-1}\right|$. From numerical simulations such as in Fig. 3.6a and Fig. 3.6b, we find in

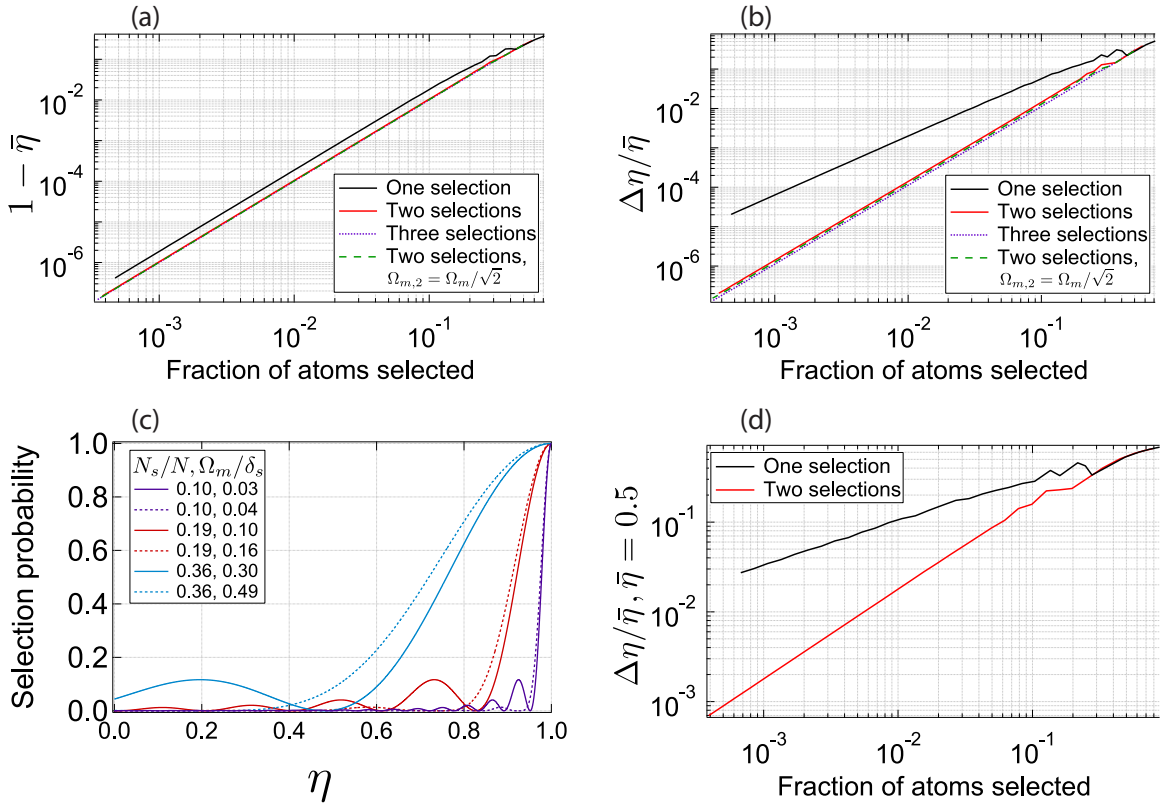


Figure 3.6: Simulation with minimal model. (a) Curves for $1-\bar{\eta}$ vs fraction of atoms selected, for one, two and three selections, coded in black solid, red solid and purple dashed. We also plotted the same relationship for two selections with varying Rabi frequencies, with the Rabi frequency of the second selection pulse $\Omega_{m,2}=\Omega_m\sqrt{2}$, which is coded in green dashed. The curve for three selections is hard to identify because it is pretty much buried under the red and green curves. The simulation is done with $\delta_m=0$, and the change in the fraction of atoms is achieved by changing the ratio $\Omega_m/\delta_s$. (b) Curves for $\Delta\eta/\bar{\eta}$ vs fraction of atoms selected, for one, two and three selections, coded in the same way as in (a). The curve for two selections with varying Rabi frequencies is also presented. (c) Transfer probability vs $\eta$ for one selection (solid curves) and two selections (dashed curves). Different colors correspond to different $\Omega_m/\delta_s$ and $N_s/N$. (d) Curves for $\Delta\eta/\bar{\eta}$ vs fraction of atoms selected, for one and two selections, color coded in black and red. These curves are obtained with $\delta_m=\frac{1}{2}\delta_s$.

the region $N_s/N<0.1$ that $1-\bar{\eta}=A\,(N_s/N)^{\alpha}$, where $\alpha=2.00$ and $A=1.83,1.04,1.00,1.00$ for 1, 2, 3 and 4 selection pulses with the same Rabi frequency respectively. The fitting result for two selections with varying Rabi frequencies is $\alpha=2.00$ and $A=1.01$. Similarly, we find $\Delta\eta/\bar{\eta}=A\,(N_s/N)^{\alpha}$, where $\alpha=1.47,2.00,2.00,2.00$ and $A=1.75,1.41,1.12,1.09$ for 1, 2, 3, and 4 selection pulses with the same Rabi frequency respectively. The fitting result for two selections

with varying Rabi frequencies is $\alpha = 2.00$ and $A = 1.27$. For two selections or greater, the qudratic scaling of the inhomogeneity is highly favorable. We also note that the inhomogeneity is only marginally improved for greater than two selection pulses. Applying two selection pulses with varying Rabi frequencies can improve the averaged coupling and homogeneity compared to two selection pulses with the same Rabi frequency, but it cannot beat three selection pulses.

For comparison, we show the trade off versus the fractional standard deviation of the coupling about the mean $\Delta\eta/\bar{\eta}$ when $\delta_m = \frac{1}{2}\delta_s$ in Fig. 3.6d. We could select atoms located at the maximum slope of the atomic probe intensity profile in this way, which are potentially useful in certain circumstances, for example, ponderomotive squeezing [15]. Because of symmetry, $\bar{\eta} = 0.5$ holds all the time, as noted in the figure. Likewise, we find $\Delta\eta/\bar{\eta} = A\,(N_s/N)^{\alpha}$, where $\alpha = 0.48, 0.99, 1.00$ and $A = 0.93, 1.70, 1.30$ for 1, 2 and 3 selection pulses with the same Rabi frequency respectively. Only linear scaling can be obtained with two or more selection pulses.

## 3.4 Microwave Spectrums and Fluorescence Measurements

How the Stark shift beam modifies the microwave spectrum is shown in Fig. 3.7a. The dashed trace is the original microwave spectrum without the presence of the Stark shfit beam with long-time Rabi flopping. The solid trace is taken with microwave $\pi$-pulses of Rabi freqeucny $\Omega_{m0} = 2\pi \times 2.04$ kHz, when the Stark shift beam is on. The horizontal axis can also be converted into $\eta = g^2/g_0^2$, which the microwave transition frequency change is proportional to, as shown in Fig. 3.7b. $\eta$ is physically meaningful in the range from 0 to 1, and the corresponding microwave frequency range suggested that the peak AC Stark shift $\delta_{s0}$ induced by Stark shift beam is about $2\pi \times 32.7$ kHz. The finite cavity frequency shift in the grey regions comes from non-zero Rabi frequency. The cavity frequency shift $\delta\omega_c$ after a microwave $\pi$-pulse takes the form in Eq. (3.7),

$$\delta\omega_c = N_{tot}\delta\omega_{c0}\int_0^1 \eta P(\eta) F(\eta_c, \eta, \Omega_p, \delta_s) d\eta, \tag{3.7}$$

where $N_{tot}$ is the total number of atoms, $\delta\omega_{c0}$ is the cavity frequency shift induced by a single atom

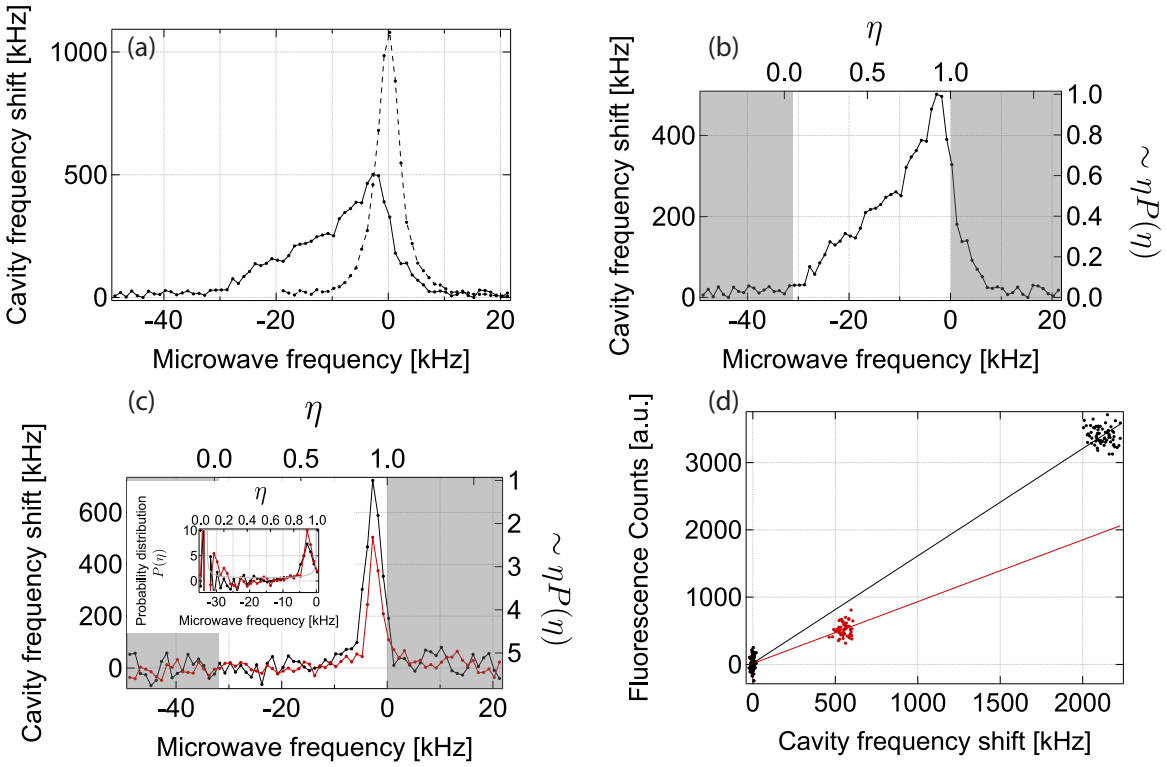


Figure 3.7: Microwave spectrums and fluorescence measurements. (a) Microwave spectrums for atoms with (solid line) and without (dashed line) the Stark shift beam. For reference, a single atom sitting at the anti-nodes of the atomic probe gives a cavity frequency shift of about 150 Hz. (b) Microwave spectrum for atoms with the Stark shift beam on in the cavity frequency shift vs microwave frequency basis can be mapped onto approximate $\eta^2 P(\eta)$ vs $\eta$ basis, with $P(\eta)$ the atomic probability distribution. Physically unavailable regions are shaded in gray. (c) Microwave spectrums for atoms after one (black) and two (red) selections are mapped in the same way as the spectrum in (b). The insets are in $P(\eta)$ vs $\eta$ basis obtained after approximating window functions as delta functions. The grey line in the background is the original probability density function for atoms without any selections. (d) Spectrums in fluorescence counts vs cavity frequency shift basis for atoms after one selection (red) and without any selections (black).

sitting at the anti-node of the atomic probe, $P(\eta)$ is the probability density, and $F(\eta_c, \eta, \Omega_p, \delta_s)$ is as defined in Eq. (3.6), with $\Omega_p$ the Rabi frequency for spectroscopy $\pi$-pulse.

$F(\eta_c)$ will approach a Dirac delta function $\delta(\eta_c)$ in the limit $\Omega_p \to 0$. As a result, the vertical axis of Fig. 3.7b can only be approximated as $\eta P(\eta)$ due to finite $\Omega_p$, represented by the tilde on the axis label. It is worth mentioning that we used $\Omega_p = \Omega_{m0}$ for the spectrum in Fig. 3.7b, and $\Omega_p \approx \frac{1}{12}\Omega_{m0}$ for the spectrums in Fig. 3.7c.

The black and red traces in Fig. 3.7c are microwave spectrums for atoms after one selection pulse and two selection pulses. The spectrums are taken with microwave $\pi$-pulses of Rabi frequency $\Omega_p = 2\pi \times 0.17$ kHz, and $\delta_m = 2\pi \times -2.7$ kHz. Likewise, the horizontal and vertical axes can be mapped to $\eta$, and $\eta P(\eta)$. If we anyway approximate $F(\eta_c)$ as Dirac delta function $\delta(\eta_c)$, we get the discrete probability density distribution $P_d(\eta)$, normalized to the total area under the curve, truncated in the range $0.4 < \eta < 1$, as shown in the inset of Fig. 3.7c. We do not include $\eta < 0.4$ in calculating the area because the data points in that range are too noisy, since the cavity frequency shift is comparable to our measurement noise floor there. The results are summarized as follows. For one selection, we measure $\bar{\eta} = 0.88(3)$, $\Delta\eta/\bar{\eta} = 0.14(3)$, $N_s/N = 0.11(1)$, and predict $\bar{\eta} = 0.90$, $\Delta\eta/\bar{\eta} = 0.12$, $N_s/N = 0.18$. For two selections, we measure $\bar{\eta} = 0.92(4)$, $\Delta\eta/\bar{\eta} = 0.1(1)$, $N_s/N = 0.083(8)$, and predict $\bar{\eta} = 0.92$, $\Delta\eta/\bar{\eta} = 0.04$, $N_s/N = 0.12$.

Another way to measure $\bar{\eta}$ is by comparing the measured cavity frequency shift to the observed fluorescence from the atoms with and without selections. Atoms contribute differently to the cavity frequency shift depending on their coupling to the cavity, but contribute equally to fluorescence imaging. Fig. 3.7d is a plot of fluorescence counts versus cavity frequency shift. The black and red data points are for atoms without selections and after one selection, whose slopes are fitted to be $a_u = 1.60(1)$ and $a_s = 0.92(3)$ Counts/kHz respectively. From the ratio of the slopes, we infer that $\bar{\eta} = a_u/2a_s = 0.87(3)$, in agreement with the numerical prediction $\bar{\eta} = 0.90$ and the previous estimate from microwave spectrum $\bar{\eta} = 0.88(1)$.

In principle, one would expect that $\bar{\eta}$ could go even closer to 1, if we select atoms with $\delta_m = 0$ kHz microwave center frequency. We decided to take the data with detuned microwave pulses for signal to noise reasons.

One important goal we want to achieve is to suppress the optomechanical oscillations with more homogeneous atom-cavity coupling. We will move on to actively probe and characterize this effect.

## 3.5 Mitigation of Optomechanically-induced Oscillations

I have explained in Sec. 3.1.1.2 the cause of optomechanically-induced oscillations. In principle, oscillations of the dressed cavity resonance at the axial trapping frequency are expected whenever the atomic probe power is changed. However, we were only able to observe the equilibrium dressed cavity resonance change as we toggled the power of the atomic probe, because the linewidth of our cavity was about 50 kHz, much smaller than the axial trapping frequency of the optical lattice, which is about 205 kHz.

To probe the optomechanical effect, we took a sequence as follows, after two selection pulses, we pumped atoms to $|F = 2, m_F = 2\rangle$, actively locked the atomic probe frequency to the dressed cavity resonance, and monitored the dressed cavity resonance as we toggled the atomic probe power up and down with windows of 100 $\mu$s long. The polarization of the atomic probe was $\sigma_+$, so that optical pumping to darker states due to free space scattering can be ignored on the $|F = 2, m_F = 2\rangle$ to $|F = 3', m_F = 3\rangle$ cycling transition. The high and low power levels were different by a factor of 3.3. The results are presented in Fig. 3.8a. The insets are zoom-ins of the grey regions, which include two toggling cycles each. The transients of the locks are removed by subtracting off the trace obtained with an empty cavity.

As a figure of merit of the degree of inhomogeneity, we consider the degree to which the optomechanical oscillations are suppressed by the selection process via the ratio $r = a_s/a_0$ of the fractional amplitudes of oscillations of the cavity resonance frequency with $a_s$ and without $a_0$ selection. We find a measured ratio $r = 0.32$ and fraction of retained atoms $N_s/N = 0.04(1)$ with $N = 8 \times 10^4$ after a double selection with $\delta_m = 0$ and $\Omega_m/\delta_s = 0.08$ in Fig. 3.8a. For comparison, the theoretical predictions are $r = 0.08$, $N_s/N = 0.14$ and $\bar{\eta} = 0.96$. To get a sense of the sensitivity of the prediction to system parameters, if we allow for a small shift in detuning of the applied microwave frequency of 2 kHz with the same sign as the applied AC stark shift, the simulation predicts $r = 0.32$, however this also predicts $N_s/N = 0.14$, and $\bar{\eta} = 0.91$ and the source of a possible 2 kHz shift is unknown. Other effects that have been considered to explain

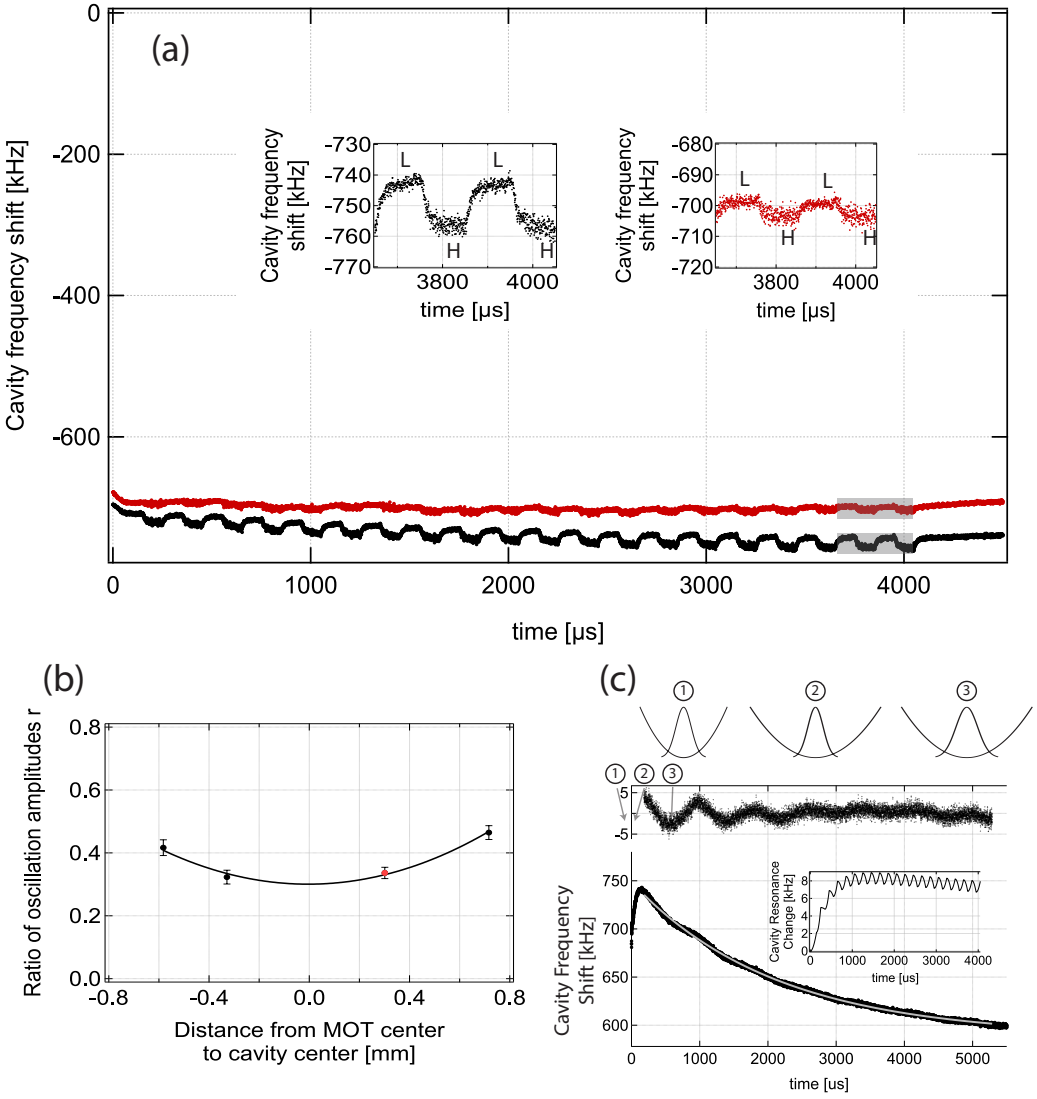


Figure 3.8: Dressed cavity equilibrium resonance change due to optomechanics. (a) Dressed cavity resonant frequency shift as a function of time when the power of the atomic probe is toggled between high and low power level. The insets are zooming-in of the grey regions. The black and red traces are for atoms without any selections and with two selections. (b) The ratio of fractional amplitudes of oscillations of the cavity resonance frequency with and without selections r, as a function of the distance from the MOT center to the cavity center. (c) Bottom panel shows the dressed cavity resonant frequency shift as a function of time with a constant atomic probe power, where the grey curve is an exponential fit. The inset is the simulated contribution of the radial oscillations to cavity-resonance frequency in Fig. Fig. 3.8b as we toggle the power in the atomic probe. The residue of the exponential fit is presented in the middle panel. The top panel sketches the relationship between the trap depth and the distribution of the atomic ensemble in position space, before, at the moment, and after the atomic probe is turned on, as indicated by the grey arrows.

the discrepancy but are not sufficiently large enough include: finite extent of axial wavefunctions, non-AC Stark shift induced inhomogeneous broadening of the microwave transition, finite radial temperature, imperfect $\pi$-pulses, errors in the ratio of the Rabi frequency to peak AC Stark shift $\Omega_m/\delta_s$, finite optical pumping to $F = 1$, and potential heating during blow away step.

We also observe that the toggling of the atomic probe power drove radial oscillations of the atomic ensemble, which makes a considerable contribution to the observed oscillation amplitude of the dressed cavity resonance. The atomic probe not only provides an axial force on the atoms, but also changes the radial confining potential. As a result, the finite temperature of the atomic ensemble and a non-adiabatic change in the radial confinement combine to drive a breathing of the radial extent of the atomic ensemble, with a period that is half of the radial oscillation period $T_r$ as illustrated in the top panel of Fig. 3.8c. Fig. 3.8c middle and bottom panels show the observed oscillations of the cavity resonance frequency due to the radial breathing. The oscillations are induced here by turning on the atomic probe and keeping it at a constant power level.

The inset of Fig. 3.8c shows the simulated contribution of the radial oscillations to the cavity-resonance frequency in Fig. 3.8a. Applying a correction for the amplitude ratio $r$, we find a corrected $r = 0.25$ closer but still off the predicted value of $r = 0.08$. This does not, however, affect the discrepancy in the number of selected atoms.

The quality of the selection also depends on the local orthogonality of the atomic probe and Stark shift standing waves, i.e., they are out of phase. We measure $r$ as a function of the position of the atomic cloud along the cavity axis as shown in Fig. 3.8b, and it is well described by a quadratic fit with a minimum value $r = 0.30(2)$. All preceding data presented in this paper was taken at the position indicated by the red point, which was 0.30(4) mm off the cavity center, not sufficiently far enough away to account for any residual discrepancies in $r$ and $N_s/N$.

## 3.6 Conclusion

In conclusion, we have demonstrated a method to obtain homogeneous atom-cavity coupling. We select atoms that are near-maximally coupled to the cavity with the help of a Stark shift

beam that is one FSR away from the cavity mode used to probe the atoms. In this way, we could always keep the atoms trapped in the Lamb-Dicke regime and retain the optical lattice wavelength as a tunable degree of freedom, which opens the route for state-dependent trapping, magic wavelength trapping and other wavelength-dependent tricks. We have also shown that this method helps suppress the optomechanical oscillations, which was a main obstacle for achieving a large amount of squeezing for inhomogenous atom-cavity coupling systems [27]. We believe the method demonstrated in this thesis could benefit experiments based on atom-cavity interactions in a broad sense.

## 3.7 Discussions

### 3.7.1 Simulations in Sec. 3.3

The simulations in Sec. 3.3 are done with the Rabi spin flip probability function Eq. (3.6), where free space scattering is ignored.

I will take one selection pulse with $\delta_m = 0$ as an example. The probability density function of the atoms in terms of $\eta$ is $P(\eta) = \frac{1}{\pi\sqrt{1-\eta}\sqrt{\eta}}$. We could calculate $N_s/N$, $\bar{\eta}$ and $\Delta\eta$ with $P(\eta)$.

$$\frac{N_s}{N} = \int_0^1 P(\eta) F(0, \eta, \Omega_m, \delta_s) d\eta \tag{3.8}$$

$$\bar{\eta} = \frac{\int_0^1 P(\eta)\eta F(0, \eta, \Omega_m, \delta_s) d\eta}{Ns/N} \tag{3.9}$$

$$\Delta\eta = \sqrt{\frac{\int_0^1 P(\eta)\eta^2 F(0, \eta, \Omega_m, \delta_s) d\eta}{Ns/N} - \bar{\eta}^2} \tag{3.10}$$

All of theses quantities can be numerically calculated with a well-defined ratio of $\Omega_m/\delta_s$. We are then able to get the curves in Fig. 3.6. Results for two or more selection pulses can be obtained similarly.

### 3.7.2 Effects from Finite Atomic Radial Extent

The distributions of the atoms in x and y directions are both Gaussian distributions with standard deviations $\sigma_x = \sigma_y$ =8 $\mu$m. As an atom goes off the cavity axis, its coupling to the cavity will be decreased because of the Gaussian profile of the cavity mode. To take into account the effects from finite atomic radial extent, we just need to integrate over the distribution in x and y in Eq. (3.8), Eq. (3.9) and Eq. (3.10).

For $\Omega_m/\delta_s = 0.08$, $\bar{\eta}$ is estimated to decrease by about 2%.

### 3.7.3 Factors Affecting the Microwave Spectrums

The simulation done as discussed in Sec. 3.9 shows that the peak of the microwave spectrum with the Stark shift beam on is located at about $\eta = 0.97$, as shown by the blue curve in Fig. 3.10, while the peak of the spectrum we measured as shown in Fig. 3.7a and also in Fig. 3.9 was located at about $\eta = 0.92$. I will discuss possible factors that could lead to such a discrepancy.

#### 3.7.3.1 Imperfect $\pi$-pulses

The effects of imperfect $\pi$-pulses can be found in Fig. 3.10. If we use 0.9 $\pi$-pulse, the peak can be shifted slightly to about $\eta = 0.96$. 0.5 $\pi$-pulse is able to displace the peak to about $\eta = 0.93$, and the corresponding lineshape actually matches the experimental data better. However, it was impossible to have such a big discrepancy in the calibration of the $\pi$-time, which was measured to be 0.245(3) ms with Rabi flopping.

#### 3.7.3.2 Error in $\Omega_m$

The effects of error in $\Omega_m$ is presented in Fig. 3.11. If I make $\Omega_m$ twice as large, the theory predictions are more close to the spectrum we got experimentally. However, we measured $\Omega_m = 2\pi \times 2.04(2)$ kHz, so the error in $\Omega_m$ is minor, and such a small error is not enough to explain the deviations of the data from the prediction. I just present this discussion here for completeness.

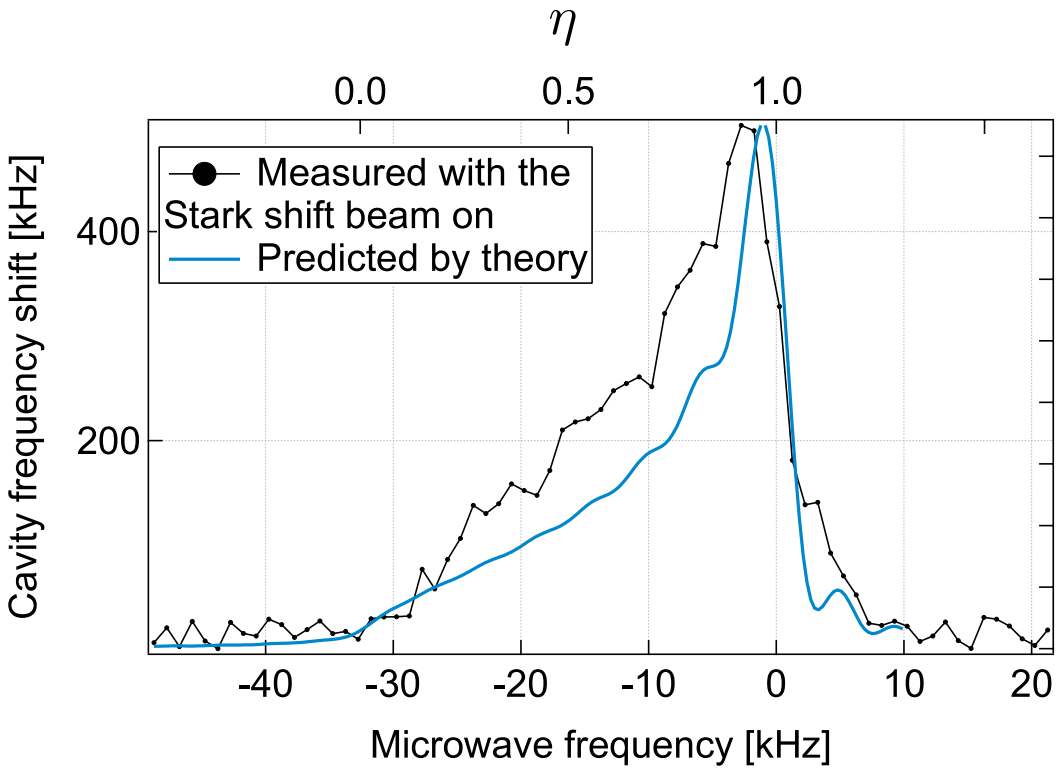


Figure 3.9: Comparison between measured microwave spectrum (black) and that predicted by theory (blue). The vertical axis of the theory plot is in a.u., and is rescaled for comparison with the experimental data. Both are with the Stark shift beam on.

#### 3.7.3.3 Error in $\delta_s$, the Peak AC Stark Shift

The effects of error in $\delta_s$ is presented in Fig. 3.12. The x-axis of Fig. 3.12 is in units of microwave frequency rather than $\eta$ because $\eta$ is dependent on $\delta_s$ as discussed in Sec. 3.4. Changing $\delta_s$ only changes the peak transfer probability, instead of the position where the peak is located.

#### 3.7.3.4 Non AC Stark shift Induced Homogeneous Brodening of the Microwave Transition

Empirically, the non AC Stark shift induced broadening of the microwave transition, if we denote its HWHM as $\gamma_{nAC}$, will modify the Rabi spin flip probability Eq. (3.6) into

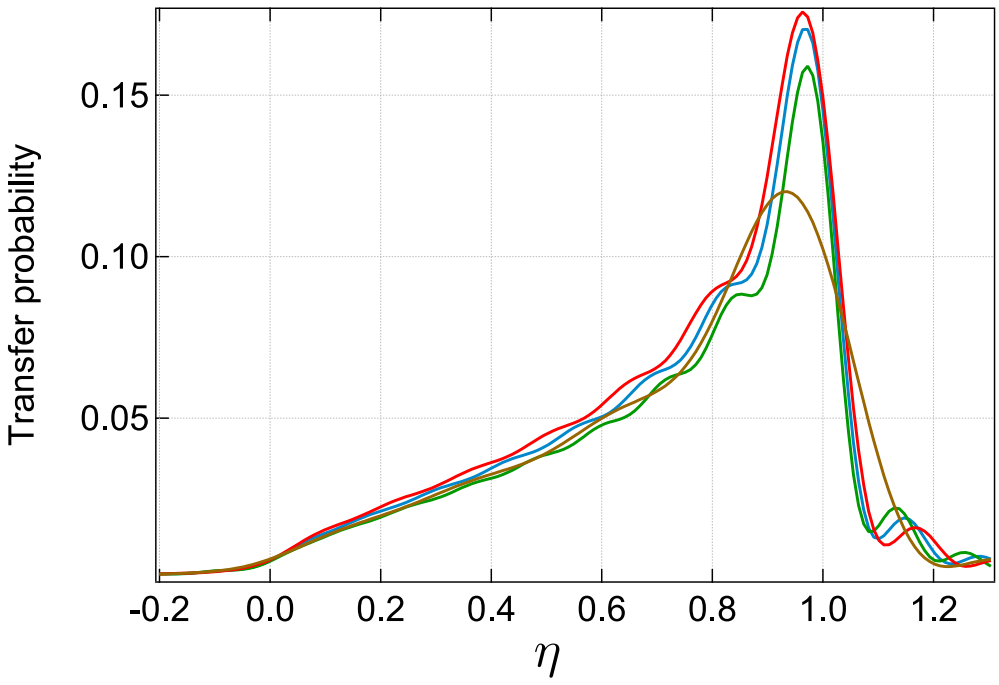


Figure 3.10: Effect of imperfect $\pi$-pulse. The blue trace is the result with a perfect $\pi$-pulse. The brown, red and green traces are the results with 0.5 $\pi$-pulse, 0.9 $\pi$-pulse and 1.1 $\pi$-pulse.

$$F_b\left(\eta_c,\eta,\Omega_m,\delta_s\right)=\frac{\Omega_m^2}{\Omega_m^2+\left(\left(\eta_c-\eta\right)\delta_s\right)^2+\left(\gamma_{nAC}\right)^2}\sin^2\left(\frac{\pi}{2}\frac{\sqrt{\Omega_m^2+\left(\left(\eta_c-\eta\right)\delta_s\right)^2}}{\Omega_m}\right). \tag{3.11}$$

We measured $\gamma_{nAC}$=1.1(2) kHz, by measuring the long-time Rabi flopping spectrum with the Rabi frequency as small as possible. As a reference, the Rabi frequency used is estimated to be smaller than 400 Hz.

Fig. 3.13 shows the effects of non AC Stark shift induced broadening of the microwave transition. A larger broadening will decrease the transition probability, but only shift the position of the peak slightly. With 5.5 kHz of broadening, the peak of the spectrum is displaced to $\eta \approx 0.95$, which is not enough to explain the discrepancy.

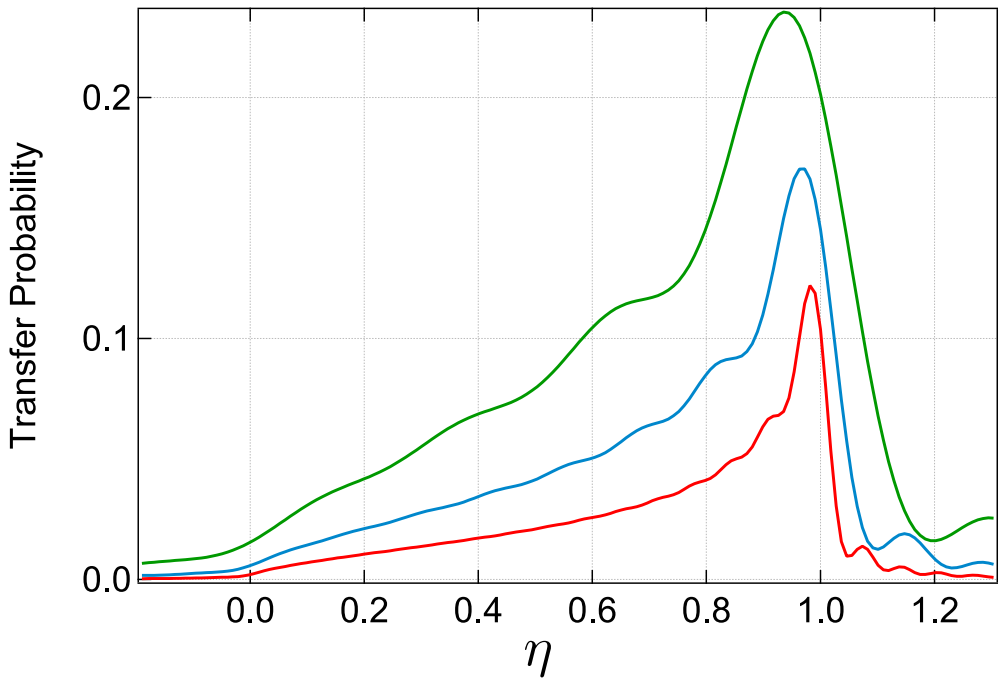


Figure 3.11: Effect of varying $\Omega_m$. The blue trace is the result with $\Omega_{m,0}$=2.04 kHz, which we used for all the analysis in this chapter. The red and green traces are the results with 0.5 $\Omega_{m,0}$ and 2 $\Omega_{m,0}$.

#### 3.7.3.5 Inhomogeneous Broadening of the Microwave Transition

Consider some type of inhomogeneous broadening $\delta_{in}$ that is subject to a Gaussian distribution $\frac{1}{\sqrt{2\pi}\sigma} e^{\frac{-\delta_{in}^2}{2\sigma^2}}$, with $\sigma$ the standard deviation of the distribution. The Rabi spin flip probability Eq. (3.6) will be modified into

$$F_b\left(\eta_c, \eta, \Omega_m, \delta_s\right) = \frac{\Omega_m^2}{\Omega_m^2 + \left(\left(\eta_c - \eta\right)\delta_s - \delta_{in}\right)^2} \sin^2\left(\frac{\pi}{2}\frac{\sqrt{\Omega_m^2 + \left(\left(\eta_c - \eta\right)\delta_s - \delta_{in}\right)^2}}{\Omega_m}\right). \tag{3.12}$$

To calculate the expected spectrums, the integral over $\delta_{in}$ weighted by the Gaussian distribution is required.

Fig. 3.14 shows the effects of the inhomogeneous broadening of the microwave transition. With $\sigma$ =3.5 kHz, the peak of the spectrum is displaced to $\eta \approx 0.92$, which is adequate to explain the discrepancy. The next question is what mechanism could induce such a broadening, which I

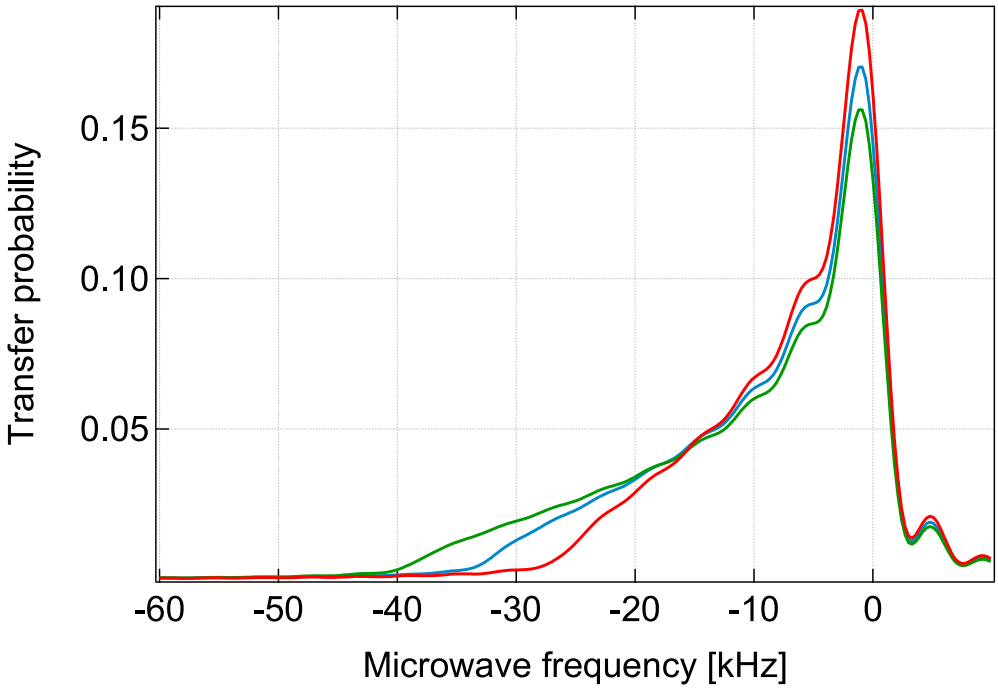


Figure 3.12: Effect of varying $\delta_s$. The blue trace is the result with $\delta_{s,0}$=32.6 kHz, which we used for all the analysis in this chapter. The red and green traces are the results with 0.8 $\delta_{s0}$ and 1.2 $\delta_{s,0}$.

will discuss below in Sec. 3.7.3.6.

#### 3.7.3.6 Finite Extent of the Axial Wavefunction

The inhomogeneous broadening of the microwave transition required in Sec. 3.7.3.5 seems large, so we are motivated to think about possible broadening mechanisms from the Stark shift beam. I will estimate how large the broadening induced by the finite extent of the axial wavefunction is.

The wavelength of our lattice is 813 nm. The trap depth is 150 $\mu$K. We could estimate the square of Lamb-Dicke parameter for the ground state, $LD^2$ ≈0.018. The ground state broadening approximates $LD^2\delta_s$, which is about 0.6 kHz.

The axial temperature of the atomic ensemble is about 1/10 of the trap depth, from which we could estimate the average occupation number in the harmonic trap, $\bar{n}$ ≈2. The square of the

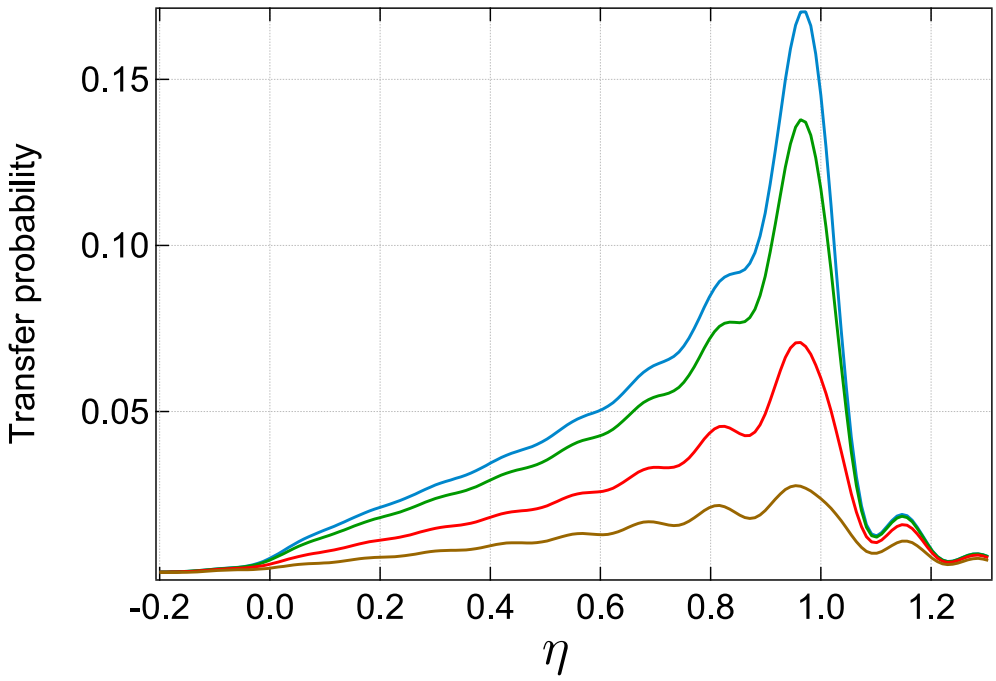


Figure 3.13: Effect of non AC Stark shift induced broadening of the microwave transition. The blue trace is the result without any broadening. The green trace is the result with broadening $\gamma_{nAC}$=1.1 kHz. The red and brown traces are the results with $2.5\gamma_{nAC}$ and $5\gamma_{nAC}$.

Lamb-Dicke parameter is related to the energy level n in the harmonic trap as $LD^2(n) \propto 2n+1$. For $n$=2, the broadening is about 3 kHz. This broadening is close to the expected value to explain the discrepancy in the microwave spectrum we saw on its own.

#### 3.7.3.7 Summary

To summarize, we have considered the effects on the microwave spectrums from imperfect $\pi$-pulses, errors in $\Omega_m$ and $\delta_s$, non AC Stark shift induced homogeneous broadening of the microwave transition and inhomogeneous broadening of the microwave transition. Finite extent of the axial wavefunction induces an inhomogeneous broadening with $\sigma \approx$3 kHz, which is close to the value needed (about 3.5 kHz) for explaining the discrepancy. It is also possible that the discrepancy results from a combination of contributions, or some other sources that have not yet been identified.

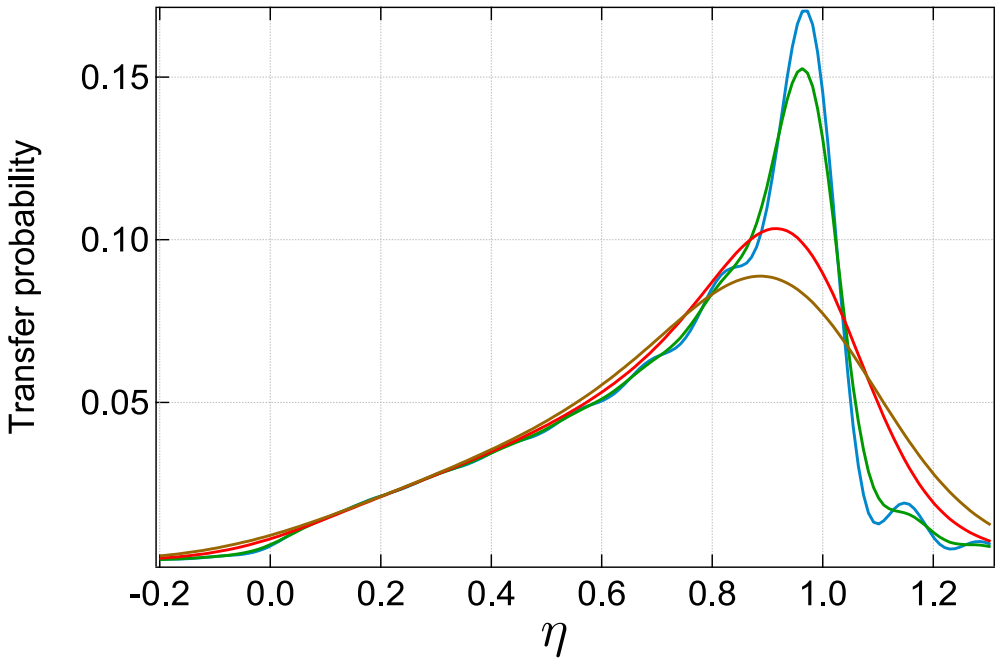


Figure 3.14: Effect of inhomogeneous broadening of the microwave transition. The blue trace is the result without any broadening. The green trace is the result with the standard deviation of the broadening $\sigma$ =1 kHz. The red and brown traces are the results with $\sigma$ =3.5 kHz and $\sigma$ =5 kHz.

### 3.7.4 Simulation of the Contribution of the Radial Oscillations to Cavity-Resonance Frequency in Fig. 3.8a

For an atom with initial position and momentum $x_0$ and $p_0$ in a harmonic trap, its position and momentum will evolve following Eq. (3.13) and Eq. (3.14)

$$x(t) = x_0 \cos(\omega t) + \frac{p_0}{m\omega} \sin(\omega t) \tag{3.13}$$

$$p(t) = -x_0 m\omega \sin(\omega t) + p_0 \cos(\omega t), \tag{3.14}$$

where $\omega$ is the trapping frequency of the harmonic trap.

If we define $p_n = p/m\omega$, the equations of motion will be modified into

$$x(t) = x_0 \cos(\omega t) + p_{n0} \sin(\omega t) \tag{3.15}$$

$$p_n(t) = -x_0 \sin(\omega t) + p_{n0} \cos(\omega t). \tag{3.16}$$

When we have an ensemble of atoms in a harmonic trap, the standard deviation in $x$ and $p_n$ will evolve following Eq. (3.17) and Eq. (3.18)

$$\Delta x(t) = \sqrt{(\Delta x_0 \cos(\omega t))^2 + (\Delta p_{n0} \sin(\omega t))^2} \tag{3.17}$$

$$\Delta p_n(t) = \sqrt{(\Delta x_0 \sin(\omega t))^2 + (\Delta p_{n0} \cos(\omega t))^2}. \tag{3.18}$$

If the trap depth changes abruptly, we just need to rescale $p_n$ and the following evolution will be governed by the same set of equations, i.e., Eq. (3.17) and Eq. (3.18).

### 3.7.5 Calculating $r$ for a Certain Distribution of Atoms

We have talked about how to extract the distribution of atoms in Sec. 3.7.1. For a certain distribution of atoms, $r$ can be estimated as follows.

The gradient force from the lattice is

$$F_g = -\frac{d}{dz} U_L \cos(k_L z)^2 = U_L k_L \sin(2k_L z) \tag{3.19}$$

where $U_L$ and $k_L = 2\pi/\lambda_L$ are the trap depth and the wavevector of the lattice.

We could then calculate the displacement $z_d$ of the $i$-th atom with the following equation of motion,

$$m\ddot{z} + U_L k_L \sin(2k_L z_d) + U_A k_A \sin(2k_A(z_d + z_i)) = 0 \tag{3.20}$$

where $U_A$ and $k_A = 2\pi/\lambda_A$ are the equivalent trap depth and the wavevector of the atomic probe, $z_i$ is the initial position of the $i$-th atom, and $m$ is the mass of an atom.

The change of the effective coupling of the $i$-th atom to the cavity can be calculated after we know its displacement, which simply changes from $\cos(k_A(z_i))^2$ to $\cos(k_A(z_d + z_i))^2$. The ratio $r$ as we toggle the power of atomic probe can be extracted from the effective total atom number change induced by the displacement.

### 3.7.6 Electronic Block Diagram for Probing the Optomechanically-induced Oscillations

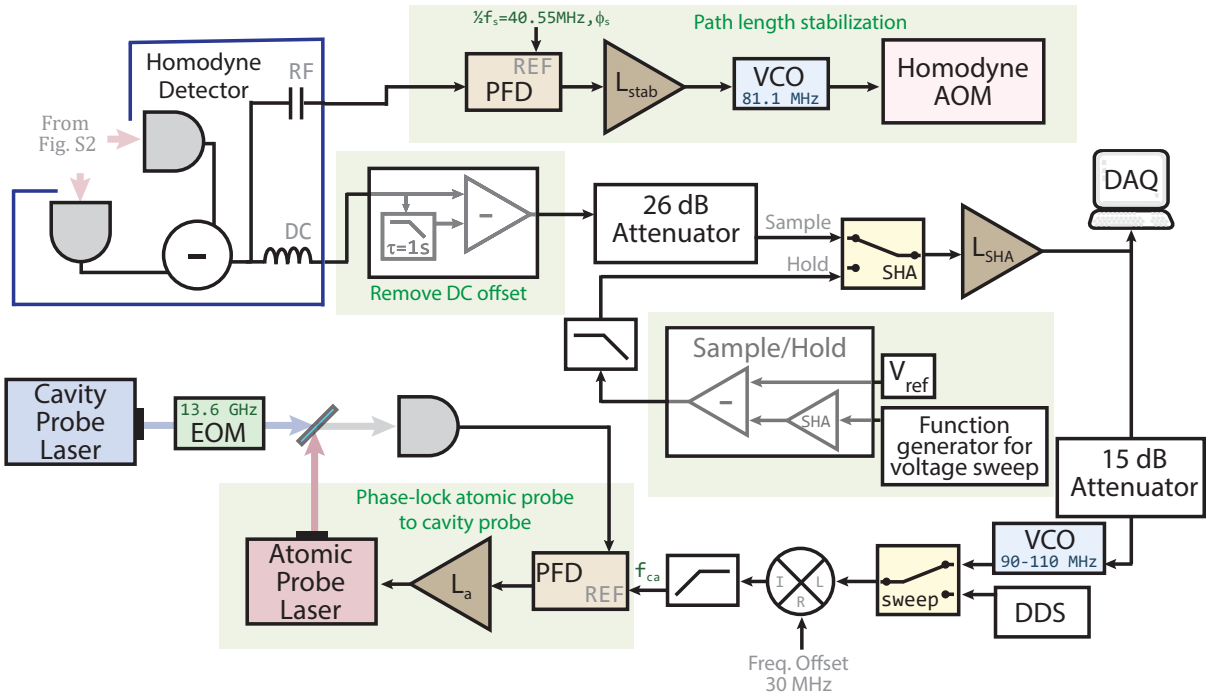


Figure 3.15: Electronic block diagram for probing the optomechanically-induced oscillations

Fig. 3.15 shows the electronic block diagram for probing the optomechanically-induced oscillations. It is pretty similar to what we used before [27]. The changes are mainly about how we look for the resonance of the cavity and hold the output voltage of the loop filter, and how to make the lock to the held DC voltage and the lock of the atomic probe to the cavity resonance compatible.

We look for the resonance of the cavity by actively scanning the input voltage of the VCO with a function generator. $V_{ref}$ is a tunable reference voltage. When the cavity resonance is found,

we will hold the VCO input voltage with the help of the sample/hold. The held voltage is what the DC lock is locked to, so that we could jump the output frequency of the VCO, and thus the frequency of the atomic probe to the cavity resonance when needed. The lock of the atomic probe to the cavity resonance is used to probe the cavity resonance with high precision. We want to make these two locks compatible so that the lock of the atomic probe to the cavity resonance is close to its lock point, when we switch the feedback path. The DC lock requires two integrator stages, however, our cavity linewidth is about 50 kHz, which works like a built-in integrator in terms of the shape of its transfer function. We thus add a low-pass filter in the DC lock path, and turn on only one integrator stage of the loop filter. The differential gains required by the two locks are bridged with the 26-dB attenuator. The 15-dB attenuator is meant for improving the precision of the measurement of the control voltage of the VCO for cavity resonance frequency readout.

# Chapter 4

## Squeezed Atom Interferometry: Scheme and Progress

In this chapter, I will explain what squeezed atom interferometry is, introduce our scheme for building an intracavity, guided squeezed atom interferometer and report our current progress. I have explained what the Mach-Zehnder type atom interferometer is in Sec. 1.3. I will keep taking the Mach-Zehnder type squeezed atom interferometer as an example here. The spin-squeezing generated for an atom interferometer needs to be homogeneously distributed between all the atoms, which is guaranteed by time-averaged probing of falling atoms in this context [28].

### 4.1 Introduction to Squeezed Atom Interferometry

In Sec. 1.3, I mapped the process of the Mach-Zehnder type atom interferometer onto Bloch spheres, as shown in Fig. 1.6. If we replace the coherent spin state with a squeezed state, we get a squeezed Mach-Zehnder type atom interferometer, as shown in Fig. 4.1.

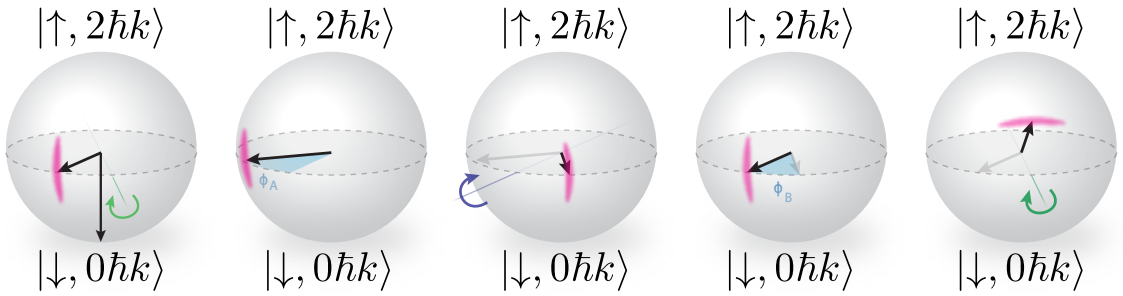


Figure 4.1: Squeezed Mach-Zehnder type atom interferometer. The only difference from a normal atom interferometer is that the coherent spin state is replaced with a squeezed state.

The squeezed state in the initialization step is a phase-squeezed state, meaning that the noise in the phase quadrature is reduced, while that in the atom number quadrature is increased. It can be transformed from the number-squeezed state introduced in Sec. 1.1 with a $\pi/2$-pulse whose rotation axis is aligned with the Bloch vector. As discussed in Sec. 1.3, the atom numbers in $|\uparrow\rangle$ and $|\downarrow\rangle$ after interference are proportional to $\cos^2(\Delta\Phi/2)$ and $\sin^2(\Delta\Phi/2)$ respectively. The definition of $\Delta\Phi$ can be found in Sec. 1.3. It is clear that the noise in the final readout depends on the precision of the quantum phase, and that is why we have to use a phase squeezed state.

## 4.2 Ingredients for Intracavity, Guided Squeezed Atom Interferometry

We mainly need three ingredients, that is, generating squeezed states, driving two-photon transitions along the cavity axis and guiding the falling of the atoms. I have described how generation of squeezed states with quantum nondemolition measurement works in Sec. 3.1.1.1, and we will keep using the same technique. I will explain the other two ingredients in this section.

### 4.2.1 Two-photon Transitions along the Cavity Axis

Consider a two-photon transition in free space between $|\downarrow, 0\hbar k\rangle$ and $|\uparrow, 2\hbar k\rangle$ driven by two counter-propagating beams at frequencies $\omega_1$ and $\omega_2$, as shown in Fig. 4.2. The atoms will be transferred from $|\downarrow\rangle$ to $|\uparrow\rangle$, and get $2\hbar k$ momentum kicks along the z-direction, if they start in $|\downarrow\rangle$ and the two beams are propagating as shown. Here $k$ is the wavevector of the lasers, $k = \omega_1/c \approx \omega_2/c$, with $c$ the speed of light. We could make the momentum kicks the atoms received $-2\hbar k$ by switching the propagation direction of the two beams or pumping atoms into $|\uparrow\rangle$ initially.

However, the modes supported by the cavity are standing waves, that is, if we inject two tones at $\omega_1$ and $\omega_2$ into the cavity, we will get both upwards-propagating and downwards-propagating beams at $\omega_1$ and $\omega_2$, as shown in Fig. 4.3. This is bad because the direction of the momentum kicks imparted becomes ambiguous. It is necessary to lift the degeneracy between the upward and downward beams.

Our method to lift the degeneracy is to allow the atoms to fall to gain an initial velocity

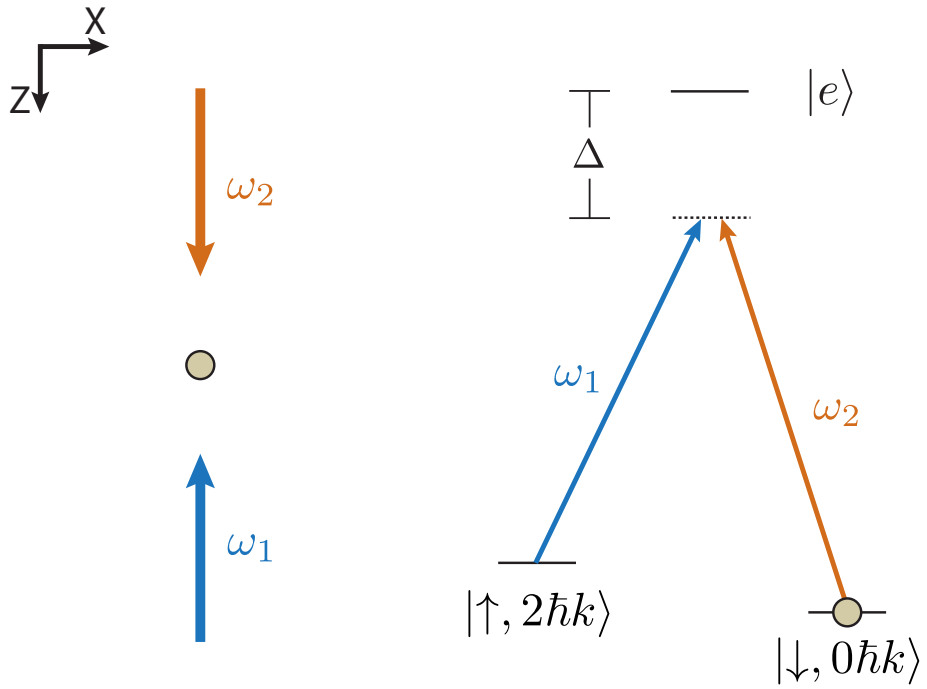


Figure 4.2: Two-photon transitions in free space. The transitions are driven by two counter-propagating beams at frequencies $\omega_1$ and $\omega_2$. Atoms are pumped into $|\downarrow\rangle$ initially.


Figure 4.3: Standing waves of cavity modes

$v$, and take advantage of the Doppler shift, as shown in Fig. 4.4. Beams co-propagating with or counter-propagating against the atoms will be shifted to the red or to the blue by $kv$. We plan to take $|\downarrow\rangle \equiv |F = 1, m_F = 0\rangle$ and $|\uparrow\rangle \equiv |F = 2, m_F = 0\rangle$ of $^{87}$Rb, so the detuning between $|\downarrow\rangle$ and $|\uparrow\rangle$ is about $\omega_{HF}$, the hyperfine splitting between F=1 and F=2 manifolds. If we choose to make the pair with frequencies $\omega_1 + kv$ and $\omega_2 - kv$ on resonance with the two-photon transition, the other pair will be detuned by $4kv$. Momentum kicks in deterministic directions are now enabled.

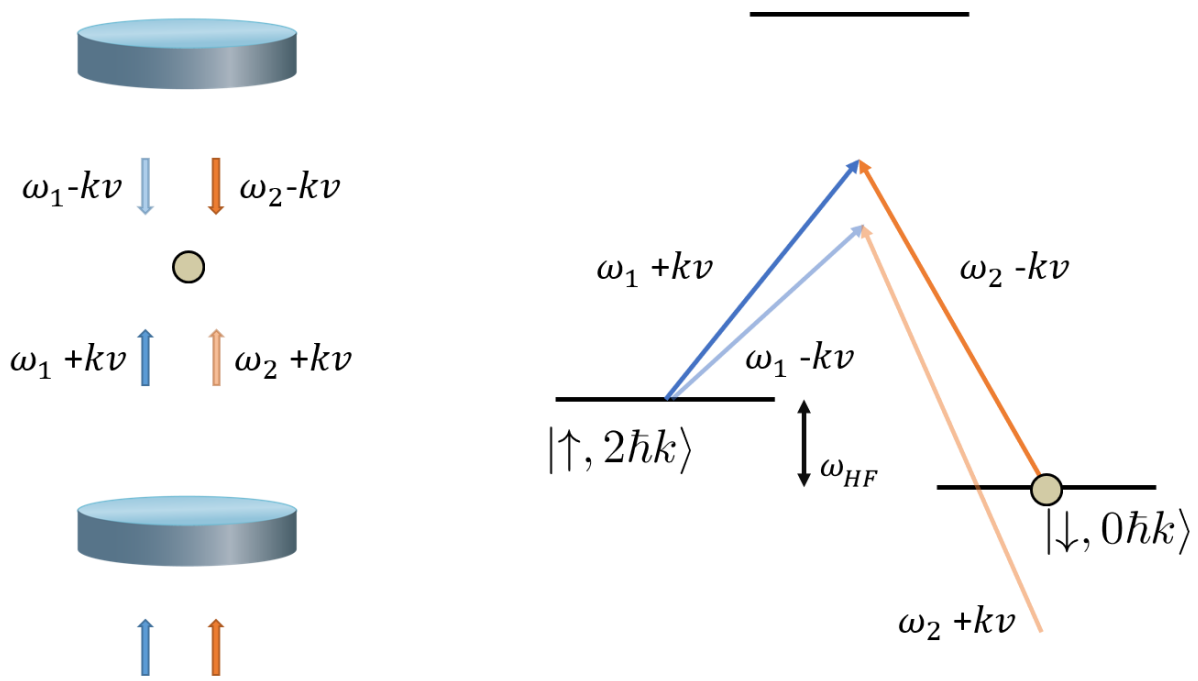


Figure 4.4: Degeneracy of counter-propagating beams lifted. Left figure shows the frequencies of the counter-propagating beams in the atom's rest frame. Right figure explains how we could deterministically apply two-photon momentum kicks in certain directions.

In Sec. 2.2, we mentioned that the desired FSR of the science cavity is 10-47 MHz detuned from the hyperfine spliting of $^{87}$Rb, $\omega_{HF}$. The reason is that we want the FSR to be close enough to $\omega_{HF}$, so that the two beams with frequencies $\omega_1$ and $\omega_2$ can be injected into adjacent cavity modes, while we also want the FSR to be far enough from $\omega_{HF}$, so that the vacuum fields of adjacent cavity modes will not make significant contributions to the two-photon transitions, and to avoid strong

conversion of laser frequency noise into intensity noise which can then drive Bragg transitions to other momentum states.

In the experiment, we generate the two tones by phase modulating the Raman laser with modulation frequency of about $\omega_{HF}/2$. The carrier of the Raman laser is locked to the cavity probe. The frequency of the Raman laser is thus indirectly stabilized to the science cavity since the cavity probe is locked to the science cavity. The arrangement is that the $\pm 1$ sidebands of the Raman laser are detuned to their nearest cavity modes by about $\pm\Delta_r = \pm(\omega_{HF} - FSR)/2 = \pm 21$ MHz, respectively.

### 4.2.2 Guided Falling of the Atoms

We need to create a spin-squeezed state that is homogeneously shared by all the atoms, which is obtained by time-averaged probing of falling atoms. The guided falling of the atoms is achieved with a dipole trap, whose axial trapping potential becomes flat but radial trapping potential is still maintained [28]. The creation of the dipole trap is illustrated in Fig. 4.5. The adjacent cavity modes have different symmetries near the center of the cavity, i.e., if the intensity pattern of one mode is described by $\cos^2(kz)$, with $k$ the wavevector of the laser and $z$ the position from the cavity center, the intensity patterns of its two adjacent modes will be approximately $\sin^2(kz)$. I take the wavevector of all three modes to be k, because FSR of the cavity is much smaller than the frequency of the laser. By injecting the lattice laser and its $\pm 1$ sidebands into the cavity and tuning the relative intensities right, we get a flat axial potential near the center of the cavity because $\cos^2(kz) + \sin^2(kz) = 1$.

We were creating the dipole trap with Hermite-Gaussian $HG_{00}$ mode of the cavity. To further reduce the bumpiness along the cavity axis, we decide to use Laguerre-Gaussian $LG_{01}$ mode, i.e., the donut beam, as shown in Fig. 4.6 Left. The $LG_{01}$ mode is generated by diffracting a Gaussian beam (the 760 nm blue lattice laser) off a phase plate, whose pattern is shown in Fig. 4.6 Right. The diffraction efficiency is about 10%. The phase plate was fabricated by the JILA Keck lab by chromium deposition.

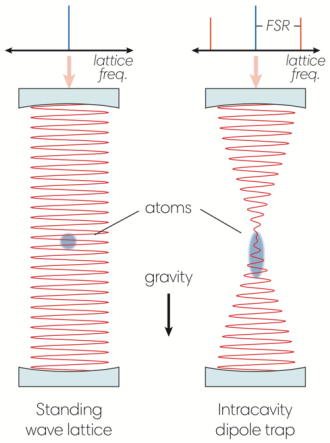


Figure 4.5: Creation of the dipole trap. What is shown in the figure is the axial intensity pattern of the intracavity optical trap.

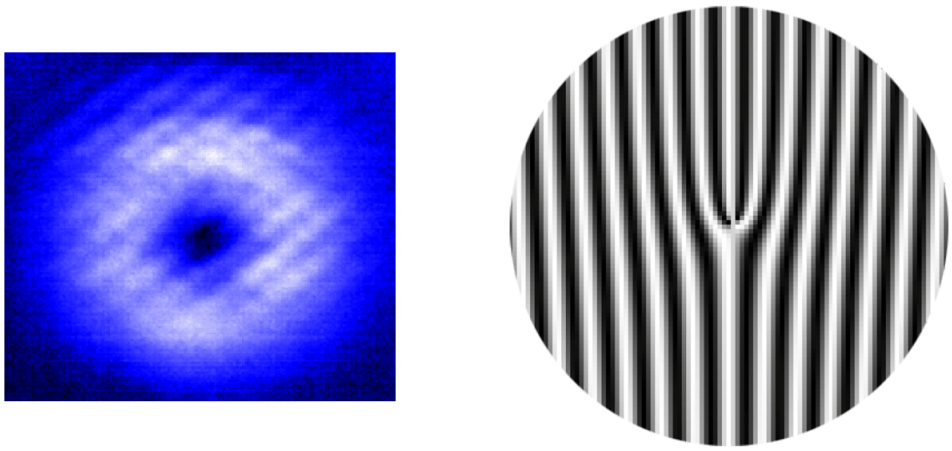

Figure 4.6: Intensity pattern of $LG_{01}$ mode and phase plate pattern for generating it. Left is the intensity pattern of $LG_{01}$ mode measured with a camera. Right is the pattern of the phase plate for generating $LG_{01}$ mode, which we learnt how to make and is reprinted from ref. [101].

## 4.3 Progress

In Sec. 4.2.1, we explained how to make the two beams with frequencies $\omega_1+kv$ and $\omega_2-kv$ on resonance with the two-photon transition for atoms moving at velocity $v$. It is natural to think that if we change the detuning between $\omega_1$ and $\omega_2$, we could interact with atoms with different velocities, and thus map out the velocity distribution of the atoms. We call such a spectrum velocimetry. The

sequence for velocimetry is as follows, we first allow atoms to fall along the cavity axis to gain some initial velocity and pump all the atoms into $|\downarrow\rangle$, then we apply a two-photon $\pi$-pulse to transfer atoms into $|\uparrow\rangle$ as we vary the detuning between $\omega_1$ and $\omega_2$, and we finally measure the atom number in $|\uparrow\rangle$. One example velocimetry is shown in Fig. 4.7. The huge peak around 0 kHz corresponds to the Doppler-free transition, which is driven by either $\omega_1 + kv$ and $\omega_2 + kv$, or $\omega_1 - kv$ and $\omega_2 - kv$. No momentum kicks are imparted on the Doppler-free transition.

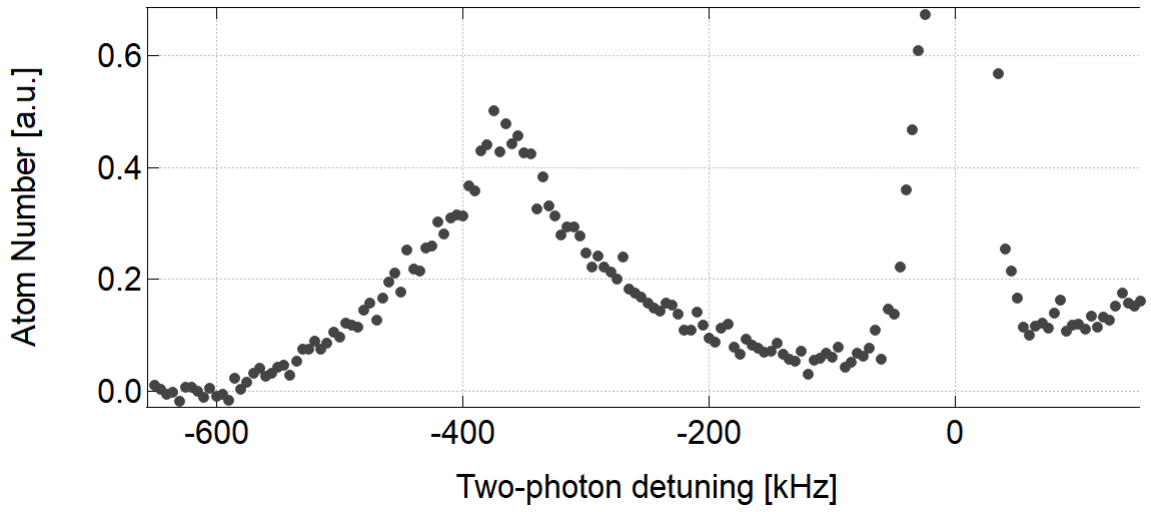


Figure 4.7: Velocimetry. The horizontal axis is the two-photon detuning $(\omega_1 - \omega_2)/2\pi$ in kHz. The vertical axis is the measured atom number in arbitrary unit (a.u.).

We could measure that the HWHM of the distribution of the Doppler shift is about 100 kHz from the velocimetry. We need velocity selections to select a group of atoms with a much narrower velocity distrbution. Velocity selections are done simply by two-photon $\pi$-pulses with a small Rabi frequency, followed by a blow-away pulse to remove those atoms that are not selected. We are able to select atoms with 1 kHz HWHM out after two selection $\pi$-pulses with 1.4 kHz of Rabi frequency.

With the atoms after velocity selections, we are able to drive the two-photon Rabi flopping, as shown in Fig. 4.8. The decoherence is dominated by the ratio of the Rabi frequency for the Rabi flopping to the HWHM of the corresponding Doppler shift of the velocity distribution in the short time limit, and the radial temperature, or radial spread of the atomic cloud in other words, in the

long time limit.

This summarizes the progress made as of Dec. 2020. We expect preliminary results by summer 2021.

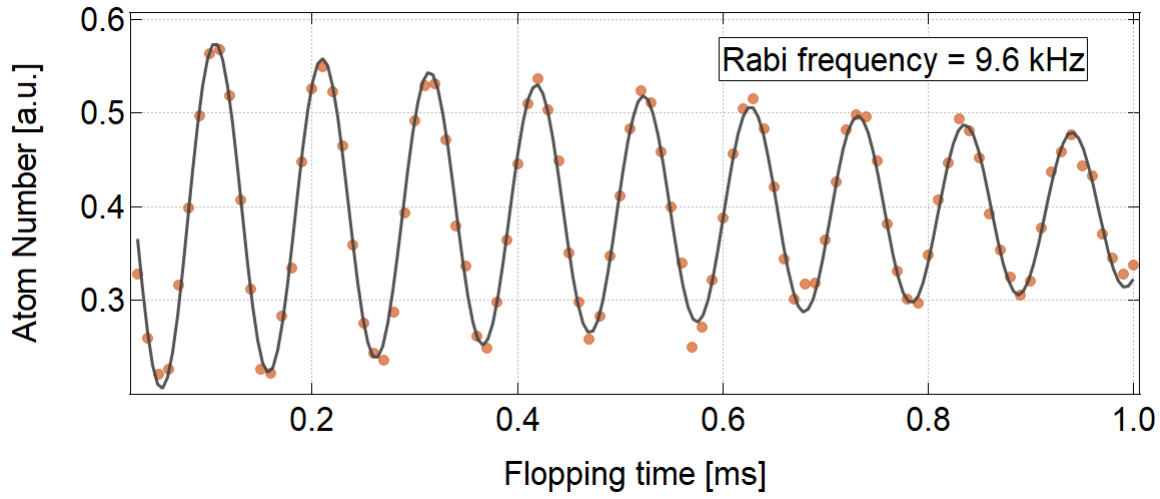


Figure 4.8: Two-photon Rabi flopping. The horizontal axis is time in ms. The vertical axis is the measured atom number in a.u.

## 4.4 Sequence for Squeezed Atom Interferometry

We plan to try a sequence as follows. First, we will load atoms into the red lattice, cool the atoms to about 7 $\mu K$ axially and about 1.5 $\mu$K radially. Then atoms will be transferred into the blue dipole trap, and allowed to fall for about 15 ms. Next, velocity selections will be applied and all the selected atoms will be optically pumped into $|\downarrow\rangle$. Afterwards, we will apply a two-photon $\pi/2$-pulse to transfer the atoms into a superposition state $|\psi\rangle = \frac{1}{\sqrt{2}}(|\downarrow, 0\hbar k\rangle + |\uparrow, 2\hbar k\rangle)$. The following quantum nondemolition measurement will create a spin squeezed state in the atom number quadrature, and we can apply an aligned $\pi/2$-pulse to transform the number squeezed state into phase squeezed state. Now we arrive at the first state shown in Fig. 4.1. All steps left will follow what is presented in Fig. 4.1.

## 4.5 Discussions

### 4.5.1 Two-photon Rabi Frequency for Atom Interferometry

I mentioned that the short-time decoherence of the Rabi flopping shown in Fig. 4.8 was dominated by the ratio of the Rabi frequency for the Rabi flopping to the HWHM of the corresponding Doppler shift of the velocity distribution. I will explain why the Rabi frequency for the Rabi flopping cannot be made arbitrarily large.

For an atom in free space, the transition frequency between two states equals the frequency change in the internal states plus that in the motional states. Consider an atom in $|\downarrow\rangle$ moving downwards at velocity $v$, whose state we label as $|\downarrow, 0\hbar k\rangle$, as shown in Fig. 4.2. The transition frequency $\delta\omega_{20}$ between $|\downarrow, 0\hbar k\rangle$ and $|\uparrow, 2\hbar k\rangle$ in the lab frame takes the form

$$\delta\omega_{20} = \delta\omega_{\uparrow\downarrow} + \left( \frac{(mv + 2\hbar k)^2}{2m} - \frac{1}{2}mv^2 \right) /\hbar, \tag{4.1}$$

$\delta\omega_{\uparrow\downarrow}$ is the transition frequency between the two internal states, $|\downarrow\rangle$ to $|\uparrow\rangle$, and $m$ is the mass of the atom. After simplification of Eq. (4.1), we get

$$\delta\omega_{20} = \delta\omega_{\uparrow\downarrow} + \left( \frac{2\hbar k^2}{m} + 2kv \right). \tag{4.2}$$

Likewise, the transition frequency between $|\downarrow, 0\hbar k\rangle$ and $|\uparrow, -2\hbar k\rangle$ is

$$\delta\omega_{-20} = \delta\omega_{\uparrow\downarrow} + \left( \frac{-2\hbar k^2}{m} + 2kv \right), \tag{4.3}$$

and the transition frequency between $|\downarrow, 4\hbar k\rangle$ and $|\uparrow, 2\hbar k\rangle$ is

$$\delta\omega_{24} = \delta\omega_{\uparrow\downarrow} + \left( \frac{6\hbar k^2}{m} + 2kv \right). \tag{4.4}$$

For $^{87}$Rb, we have $\delta\omega_{24} - \delta\omega_{20} = \delta\omega_{20} - \delta\omega_{-20} = \frac{4\hbar k^2}{m} \approx 2\pi \times 30.0$ kHz. That is to say, if the two-photon transition driven by the two lasers is on resonance with the transition between $|\downarrow, 0\hbar k\rangle$ and $|\uparrow, 2\hbar k\rangle$, it will be off resonance from the transition between $|\downarrow, 0\hbar k\rangle$ and $|\uparrow, -2\hbar k\rangle$ and the

transition between $|\downarrow, 4\hbar k\rangle$ and $|\uparrow, 2\hbar k\rangle$ by 30 kHz, as shown in Fig. 4.9, where we set $\delta\omega_{\uparrow\downarrow} = 0$ for simplicity.

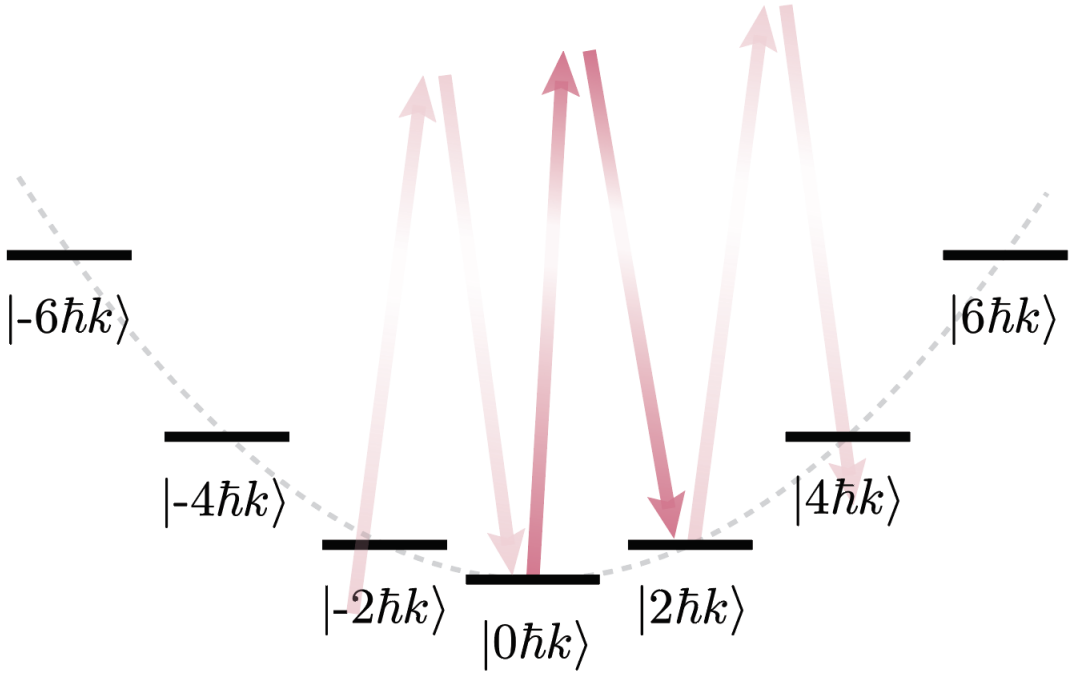


Figure 4.9: Transition frequency between adjacent momentum states. If a two-photon transition is on resonance with the transition between $|\downarrow, 0\hbar k\rangle$ and $|\uparrow, 2\hbar k\rangle$, it will be off resonance from the transition between $|\downarrow, 0\hbar k\rangle$ and $|\uparrow, -2\hbar k\rangle$ and the transition between $|\downarrow, 4\hbar k\rangle$ and $|\uparrow, 2\hbar k\rangle$.

It is clear now that if the square of the Rabi frequency for the Rabi flopping becomes comparable to $(30 \text{ kHz})^2$, the probability of the transitions into $|\downarrow, 4\hbar k\rangle$ and $|\uparrow, -2\hbar k\rangle$ become significant and we no long have well-defined two-level systems. We typically use about 9.5 kHz of Rabi frequency.

### 4.5.2 Frequency Sweep of the Two Tones for Two-photon Transitions

We need to sweep the frequencies of the two tones to compensate for the change of the Doppler shift from the free-falling of the atoms. As mentioned previously, the two tones are generated by phase modulating the Raman laser. The sweep rate of the modulation frequency is $\dot{f_m} = g/\lambda_r = 12.56$ kHz/ms, in which $\lambda_r$ is the wavelength of the Raman laser.

### 4.5.3 Amount of Squeezing Available

The maximum amount of squeezing available $\xi_m$ on clock transitions scales as $\xi_m = \sqrt{8/(qNC)}$, where q is the total quantum efficiency, N is the total atom number and C=2.06 is the single atom cooperativity [21]. Definition of C can be found in Table. 2.1.

We plan to use N=1000 for the interferometry. The total quantum efficiency is about 10%. The maximum amount of squeezing available is estimated to be 7.1 dB.

The standard quantum limit with 1000 atoms is $\Delta\phi_{SQL} = 1/\sqrt{1000} \approx 3.2 \times 10^{-2}$. With maximum amount of squeezing available, the phase resolution is improved into $\Delta\phi_M \approx 1.4 \times 10^{-2}$. This is the number that we should compare all the potential noise sources with in order to see if they will limit our ability to observe that we are generating a squeezed state that can be observed to pass through the interferometer.

### 4.5.4 Change in Effective Gravitational Acceleration $g$

The change in effective gravitational acceleration $g$ can arise from the tilt of the cavity, and the axial potential from the blue optical dipole trap.

#### 4.5.4.1 Tilt of the Cavity

We measured the tilt of the cavity with a dial gauge and were able to bound the tilt of the cavity to less than $\phi_t$=3 mrad.

The effective acceleration $g' = g\cos(\phi_t) \approx g\left(1 - (\phi_t)^2/2\right)$. This will induce a $10^{-5}$ fractional error on $g$ and thus give a small correction to the sweep rate of the modulation frequency which was discussed in Sec. 4.5.2.

#### 4.5.4.2 Axial Potential from the Blue Optical Dipole Trap

In a dipole trap, the beam diverges so that the intensity changes. Just as in previous sections discussing optomechanical forces, the gradient of this intensity change leads to a force along the axis of the cavity. For atoms at zero radial temperature, the blue guiding potential has zero intensity

on axis so there is no force. However, the atoms are at finite temperature and so here we estimate the size of the acceleration due to the finite axial gradient in the intensity of the blue optical dipole trap for the finite temperature atoms. The radial mode pattern of the $LG_{01}$ mode in the plane of the mode waist is

$$I(r) = I_0 \frac{2r^2}{w_0^2} e^{-\frac{2r^2}{w_0^2}}. \tag{4.5}$$

The trap depth of the blue optical dipole trap is more than 50 $\mu$K, while the radial temperature of the atoms is $T_a \approx$1.5 $\mu$K, so the standard deviation of the radial distribution of the atoms is at most $\sigma_r = 5.2$ $\mu$m.

I will try to estimate the effective change in $g$ for the atoms sitting $\sigma_r$ off the cavity axis. The axial potential these atoms see takes the form

$$V(z) = \frac{k_B T_a}{1 + (z/z_R)^2}, \tag{4.6}$$

where $z$ is the displacement from the cavity center, $k_B$ is the Boltzmann constant, and $z_R \approx 1.97$ cm is the Rayleigh range of the blue optical dipole trap.

The acceleration induced by the gradient of the axial potential is

$$|a(z)| = \left| \frac{d}{dz} \frac{k_B T_a}{1 + (z/z_R)^2} \right|, \tag{4.7}$$

where we take the absolute value of a(z) for simplicity. The maximum of $|a(z)|$ is estimated to be $a_m = 3.6 \times 10^{-3}$ m/s$^2$. We have $a_m/g = 3.7 \times 10^{-4}$, which is significant and we should be careful if we want to have accuracy in measurement of $g$.

### 4.5.5 Relative Phase Shift of the Two Tones Induced by Frequency Jittering of the Raman Laser

The phase of the two photon coupling is set by the difference phase between the two tones that drive the two-photon Raman transition. Anything that changes the relative phase in an uncontrolled way during an interferometer sequence will add phase noise to the atom interferometer (kind of

like vibrating mirrors in an optical interferometer) and obscure our ability to see that a squeezed state has passed through the interferometer. Here, we consider how laser frequency noise might be converted into a phase difference between the two tones. Ideally, the two tones are $\pm\Delta_r \approx \pm 21$ MHz detuned from their nearest cavity modes respectively. Consider a small frequency shift $\delta_r$ of the Raman laser, the detunings of the two tones from their nearest cavity modes becomes $\Delta_r + \delta_r$ and $-\Delta_r + \delta_r$.

To calculate the relative phase shift of the two tones, we need the transfer function of the cavity. For an incident field $E_{inc}(t) = E_{inc}e^{-i\omega t}$, and a circulating field inside the cavity $E_{cav}(t) = E_{cav}e^{-i\omega t}$, the following relation always hold,

$$E_{inc}t_1 + E_{cav}r_2r_1e^{i2L\omega/c} = E_{cav}, \tag{4.8}$$

where $t_1$ and $r_1$, and $t_2$ and $r_2$ are the transmission and reflection coefficients of the input and ouput mirror, L is the length of the cavity, and c is speed of light.

In the limit $|\omega - \omega_c| \ll \frac{c}{2L}$, the transfer function is

$$T(\omega) = \frac{E_{cav}}{E_{inc}} = \frac{F\sqrt{T_1}}{\pi}\frac{1}{1 - i\frac{\omega-\omega_c}{\kappa_c/2}}, \tag{4.9}$$

in which $\omega_c$ is the cavity resonant frequency, $F$ is the finesse of the cavity, $T_1 = |t_1|^2$, and $\kappa_c$ is the linewidth of the cavity. We then have $arg(T(\omega)) = \tan^{-1}(\frac{\Delta}{\kappa_c/2})$, where $\Delta = \omega - \omega_c$ is the detuning.

Let's now estimate the change in the difference phase if during the interferometer sequence, the central laser frequency used to create the two laser tones shifts by $\delta_r$. The change in the difference phase is

$$\delta\phi = (\tan^{-1}(\frac{\Delta_r}{\kappa/2}) - \tan^{-1}(\frac{-\Delta_r}{\kappa/2})) - (\tan^{-1}(\frac{\Delta_r + \delta_r}{\kappa/2}) - \tan^{-1}(\frac{-\Delta_r + \delta_r}{\kappa/2})), \tag{4.10}$$

where $\kappa$ =52.1 kHz is the linewidth of the science cavity. In the limit $\Delta_r \gg \delta_r, \kappa$, Eq. (4.10) can be approximated as $\delta\phi \approx -\frac{\kappa\delta_r^2}{\Delta_r^3}$.

$\delta_r$ can be suppressed below $\kappa$ easily, so we have $\delta\phi < 6.2 \times 10^{-6} \ll \Delta\phi_M$. So, by operating

at large detuning, the laser frequency noise will not hamper our ability to see the squeezed state pass through the interferometer.

### 4.5.6 Cavity Induced Phase to Amplitude Noise Conversion

When the frequency of the laser for driving two-photon transitions jitters, the coupling of the driving tones to the cavity will change, so there will be amplitude noise on the two photon Rabi frequency $\Omega_{2ph}$ due to the laser frequency jittering. Luckily, there will be first order cancellation of the amplitude noise induced by frequency jittering, because the two-photon Rabi frequency $\Omega_{2ph}$ scales as $\Omega_{2ph} \propto \sqrt{\frac{1}{1+\frac{(\Delta_r+\delta\Delta)^2}{(\kappa/2)^2}}\frac{1}{1+\frac{(\Delta_r-\delta\Delta)^2}{(\kappa/2)^2}}}$, where $\delta\Delta$ denotes the frequency jittering. In the limit $\Delta_r \gg \delta\Delta, \kappa$, we have $\Omega_{2ph} \propto \frac{(\kappa/2)^2}{\Delta_r^2}\left(1-\frac{\delta\Delta^2}{\Delta_r^2}\right)$. We will focus on the amplitude noise converted from the phase noise with the help of the cavity here.

The phase noise of a laser is presented as the finite linewidth of the laser. With the help of the cavity, the phase noise can be converted into amplitude noise, because the transfer function of the cavity is frequency-dependent. We will derive a formalism for estimating the converted amplitude noise and bound the amplitude noise in our interferometry experiment.

Consider a laser whose phase noise is modeled with a time-dependent phase fluctuation $\phi(t)$,

$$E_i(t) = E_{i,0}\cos(\omega_0 t + \phi(t)). \tag{4.11}$$

Apply Fourier transform to $\phi(t)$, and we get

$$E_i(t) = E_{i,0}\cos\left(\omega_0 t + \int_0^\infty \tilde{\phi}(\omega)\cos(\omega t)d\omega\right), \tag{4.12}$$

where we have assumed the lineshape of the laser is symmetric. If we discretize Eq. (4.12) and focus on a single frequency component $\omega = \omega_s$, we have

$$E_s(t) = E_{i,0}\cos\left(\omega_0 t + \tilde{\phi}(\omega_s)\cos(\omega_s t)\right), \tag{4.13}$$

where $\tilde{\phi}(\omega_s) = \sqrt{S_\phi df}$, with $S_\phi$ the power spectral density of phase fluctuation and $df$ an infinitesimal frequency range. For a Lorentzian lineshape, $S_\phi(f) = \frac{\Delta\nu}{\pi f^2}$, with $\Delta\nu$ the FWHM of the laser,

and $f$ the frequency component of the power spectral density. Eq. (4.12) is a standard form of the phase modulation, whose modulation index is $\beta = \tilde{\phi}(\omega_s) = \sqrt{\frac{2\pi\Delta\nu}{\pi\omega_s^2}d\omega}$, with $d\omega = 2\pi df$. In the limit $\beta$ is small, we have

$$E_s(t) = E_{i,0}[\cos(\omega_0) + \frac{\beta}{2}\cos(\omega_0+\omega_s) - \frac{\beta}{2}\cos(\omega_0-\omega_s)]. \tag{4.14}$$

We have derived the transfer function of the cavity as shown in Eq. (4.9). I will rewrite it as

$$T(\omega) = \frac{F\sqrt{T_1}}{\pi}\frac{1}{\sqrt{1+(\frac{\omega-\omega_c}{\kappa_c/2})^2}}e^{i\tan^{-1}(\frac{\omega-\omega_c}{\kappa_c/2})}. \tag{4.15}$$

The carrier of the field described by Eq. (4.14) after injected into the cavity becomes

$$E_{c,0} = \frac{1}{\sqrt{1+(\frac{\omega_0-\omega_c}{\kappa_c/2})^2}}e^{i\tan^{-1}(\frac{\omega_0-\omega_c}{\kappa_c/2})}E_{i,0}e^{i\omega_0 t}. \tag{4.16}$$

The two sidebands becomes

$$E_{c,+} = \frac{\beta}{2}\frac{1}{\sqrt{1+(\frac{\omega_0+\omega_s-\omega_c}{\kappa_c/2})^2}}e^{i\tan^{-1}(\frac{\omega_0+\omega_s-\omega_c}{\kappa_c/2})}E_{i,0}e^{i(\omega_0+\omega_s)t} \tag{4.17}$$

$$E_{c,-} = -\frac{\beta}{2}\frac{1}{\sqrt{1+(\frac{\omega_0-\omega_s-\omega_c}{\kappa_c/2})^2}}e^{i\tan^{-1}(\frac{\omega_0-\omega_s-\omega_c}{\kappa_c/2})}E_{i,0}e^{i(\omega_0-\omega_s)t}. \tag{4.18}$$

In the limit $\omega_0-\omega_c \gg \kappa_c/2$ and $\omega_0-\omega_c \gg \omega_s$, we get

$$E_{c,0} = \frac{\kappa_c/2}{\omega_0-\omega_c}e^{i(\frac{\pi}{2}-\frac{\kappa_c/2}{\omega_0-\omega_c})}E_{i,0}e^{i\omega_0 t} \tag{4.19}$$

$$E_{c,+} = \frac{\beta}{2}\frac{\kappa_c/2}{\omega_0+\omega_s-\omega_c}e^{i(\frac{\pi}{2}-\frac{\kappa_c/2}{\omega_0+\omega_s-\omega_c})}E_{i,0}e^{i(\omega_0+\omega_s)t} \tag{4.20}$$

$$E_{c,-} = -\frac{\beta}{2}\frac{\kappa_c/2}{\omega_0-\omega_s-\omega_c}e^{i(\frac{\pi}{2}-\frac{\kappa_c/2}{\omega_0-\omega_s-\omega_c})}E_{i,0}e^{i(\omega_0-\omega_s)t}. \tag{4.21}$$

We could then express $\frac{E_{c,+}}{E_{c,0}}$ and $\frac{E_{c,-}}{E_{c,0}}$ as follows

$$\frac{E_{c,+}}{E_{c,0}} = (1 - \frac{\omega_s}{\omega_0 - \omega_c}) e^{i\frac{\omega_s \kappa/2}{(\omega_0-\omega_c)^2}} \frac{\beta}{2} e^{i\omega_s t} \tag{4.22}$$

$$\frac{E_{c,-}}{E_{c,0}} = -(1 + \frac{\omega_s}{\omega_0 - \omega_c}) e^{-i\frac{\omega_s \kappa/2}{(\omega_0-\omega_c)^2}} \frac{\beta}{2} e^{-i\omega_s t}. \tag{4.23}$$

If we decompose $\frac{E_{c,+}}{E_{c,0}} + \frac{E_{c,-}}{E_{c,0}}$ into amplitude modulation and phase modulation basis, with the form

$$\frac{E_{c,+}}{E_{c,0}} + \frac{E_{c,-}}{E_{c,0}} = (Pe^{i(\omega_s t+\psi)} - Pe^{-i(\omega_s t+\psi)}) + (Ae^{i(\omega_s t+\eta)} + Ae^{-i(\omega_s t+\eta)}), \tag{4.24}$$

we find that $2A = -\beta\frac{\omega_s}{\omega_0-\omega_c} = -\sqrt{\frac{2\pi\Delta\nu d\omega}{\pi}}\frac{1}{\omega_0-\omega_c}$. In the limit 2A is small, the time-dependent form of the amplitude modulation component of the cavity field can be written as

$$E_a(t) = E_{i,0}(1 + \Sigma_s 2A\cos(\omega_s t + \phi_s)), \tag{4.25}$$

where we sum over noise frequency $\omega_s$ which goes from 0 to $\infty$ with step size $d\omega$.

For a two-photon transition driven by two tones generated from phase modulations, the instantaneous two-photon Rabi frequency $\Omega_{tp}(t)$ follows the relationship shown in Eq. (4.26),

$$\Omega_{tp}(t) \propto (1 + \Sigma_s 2A\cos(\omega_s t + \phi_s))(1 - \Sigma_s 2A\cos(\omega_s t + \phi_s)). \tag{4.26}$$

If we denote ensemble average with $\langle\rangle$, time average with $\bar{}$ and assume that the frequency of the phase modulated carrier is perfectly centered between two adjacent cavity modes, we get the form of the amplitude noise

$$\frac{\sqrt{\langle\bar{\Omega}_{tp}^2\rangle - \langle\bar{\Omega}_{tp}\rangle^2}}{\langle\bar{\Omega}_{tp}\rangle} = \frac{\sqrt{\Sigma_s (A)^4 \frac{1-\cos(2\omega_s T)}{(T\omega_s)^2}}}{1 - 2A^2}, \tag{4.27}$$

where T is the $\pi$-time of the two-photon Rabi flopping, which is the period that the time-average is done over.

Notice that only the term containing $A^4 \propto (d\omega)^2$ survives, so the amplitude noise converted from phase noise is also subject to first order cancellation.

# Chapter 5

## Laser Cooling with Adiabatic Transfer on Raman Transitions

In this chapter, I will review a 1D sub-Doppler cooling technique via adiabatic transfer on Raman transitions. This technique was inspired by Sawtooth Wave Adiabatic Passage (SWAP) laser cooling demonstrated using a narrow-linewidth single-photon optical transition in $^{88}$Sr [81, 3], and in $^{163}$Dy [83]. Here we demonstrate that two-photon Raman transitions with arbitrarily-tunable linewidths of $^{87}$Rb can be used to achieve 1D SWAP cooling without significantly populating the intermediate excited state. Unlike SWAP cooling on a narrow transition, Raman SWAP cooling allows for a final 1D temperature well below the Doppler cooling limit (here, 25 times lower), and the effective excited state decay rate can be modified in time, presenting another degree of freedom during the cooling process. Here, I reproduce the work published in ref. [41] with little modification.

### 5.1 Introduction

Advances in laser cooling techniques have opened new scientific vistas for neutral atoms, ions, and mechanical resonators [22, 32, 18]. Doppler cooling techniques have been widely applied to produce atoms at mK to sub-$\mu$K temperatures and high phase-space density [100, 34, 54, 67, 103, 5, 104, 58, 6]. However, standard Doppler cooling is limited in both final temperature and maximum force by the linewidth $\Gamma$ and wavelength $\lambda \equiv 2\pi/k$ of the available optical transitions – properties that are provided by nature and not under control of the experimentalist. Understanding methods and limitations for removing entropy from a system is of fundamental interest and continues to be widely explored [102, 18, 50, 25, 88, 84, 35].

Recently, a new mechanism called Sawtooth Wave Adiabatic Passage (SWAP) cooling was observed using a narrow-linewidth optical transition in $^{88}$Sr atoms [81], and a related deflection force was previously reported in He atoms [73]. The forces that give rise to SWAP cooling rely on adiabatic transitions back and forth between a ground state $|a\rangle$ and a long-lived optically excited state $|b\rangle$ with lifetime $\tau = 1/\Gamma$. This allows for many photon-recoils worth of momentum reduction before spontaneous emission occurs, but so far, SWAP cooling has been limited to single-photon transitions.

In this chapter, we present proof-of-principle experiments in $^{87}$Rb to demonstrate that the SWAP cooling mechanism does not require a closed, single-photon transition. Rather, it is amenable to atoms and molecules with at least two long-lived ground states. The core idea is to dress these ground states (here labeled $|a\rangle$ and $|b\rangle$) using externally applied lasers tuned off-resonance from an intermediate optically excited state $|i\rangle$. This permits us to engineer effective optically excited states with tunable lifetimes or, equivalently, linewidths instead of relying on the properties of the optical transitions $|a, b\rangle \leftrightarrow |i\rangle$ (Fig. 5.1(a)). Unlike the previous report of SWAP cooling with $^{88}$Sr, we achieve an equilibrium temperature in 1D that is 25 times lower than the usual $T_D \approx \frac{\hbar\Gamma}{2k_B} = 146\ \mu$K cooling limit for standard Doppler cooling in $^{87}$Rb.

In SWAP cooling using a single-photon transition, the magnetic field gradients, laser directions, and polarizations are essentially identical to those of standard Doppler cooling except that the pair of counter-propagating laser beams are ramped in frequency in a sawtooth pattern from below to above the transition frequency $\omega_a$ (Fig. 5.1(c and e)). The relative Doppler shift of the two laser beams causes the beam counter-propagating to the atom's motion to pass through resonance before the co-propagating beam. As a result, the counter-propagating beam drives an adiabatic transition from $|a\rangle$ to $|b\rangle$ along with a momentum kick due to photon absorption that opposes the atomic motion. The co-propagating beam then drives an adiabatic transition back from $|b\rangle$ to $|a\rangle$ along with a momentum kick due to stimulated emission that, again, slows the atom. In net, each sweep ideally removes $2\hbar k$ of momentum, reducing the atom's speed regardless of the direction it is moving.

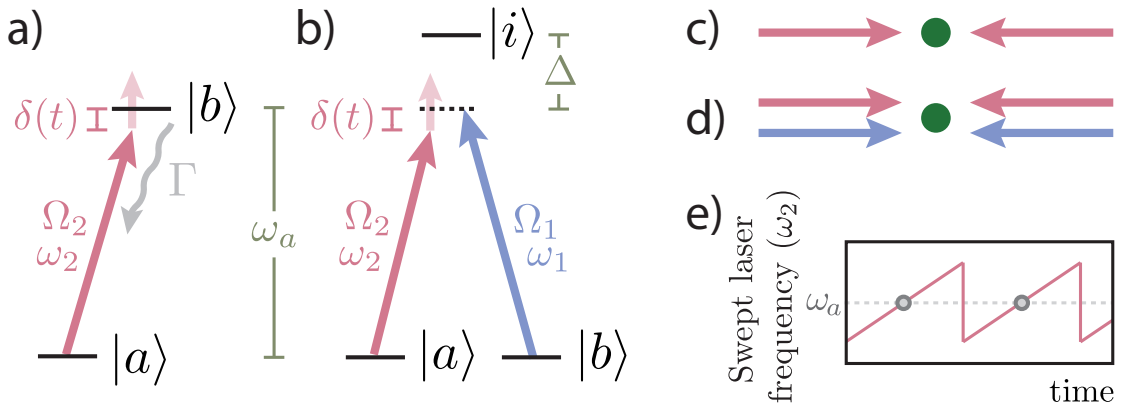


Figure 5.1: Comparison between Single-photon and Two-photon SWAP Cooling. (a) and (b) SWAP cooling level diagram for a single-photon narrow-linewidth transition and a two-photon Raman transition. In the Raman scheme, the large detuning $\Delta$ from the intermediate state ensures the effective lifetime of the excited state $|b\rangle$ is effectively infinite except when it is useful to induce decay back to $|a\rangle$ following each sweep. (c) In the single-photon case, the $\omega_2$ laser (red) is counter-propagating and incident upon an atom (green). (d) The two-photon case is identical except a second $\omega_1$ laser (blue) serves to dress the $|b\rangle$ state. (e) The frequency of $\omega_2$ is sawtooth-swept through the atomic transition frequency.

In SWAP cooling using a two-photon transition, the frequency of the laser dressing the ground state $|b\rangle$ is held fixed (figure. 5.1(d)). The laser dressing the ground state $|a\rangle$ is swept in an asymmetric sawtooth pattern through a two-photon resonance, driving adiabatic two-photon Raman transitions between the states $|a\rangle$ and $|b\rangle$. At the end of the sweep, optical pumping is briefly applied to transfer atoms erroneously remaining in $|b\rangle$ back to $|a\rangle$. In comparison to the work in strontium [81], this is equivalent to being able to set $\Gamma \approx 0$ during the frequency sweep, but then setting $\Gamma$ up to the lifetime of the intermediate state for a very brief period of time in between sweeps, potentially offering a different degree of freedom for optimizing cooling.

## 5.2 Laser Cooling $^{87}$Rb with Adiabatic Transfers

Fig. 5.2 shows the experimental setup for demonstrating 1D Raman SWAP cooling in $^{87}$Rb. The quantization axis is established by a uniform magnetic field applied along the propagation axis of the cooling beams. The two ground states are the hyperfine Zeeman states $|a\rangle \equiv |F = 2, m_F = 0\rangle$ and $|b\rangle \equiv |F = 1, m_F = 0\rangle$. These states are coupled by lasers at frequencies $\omega_1$ and $\omega_2$, both far-

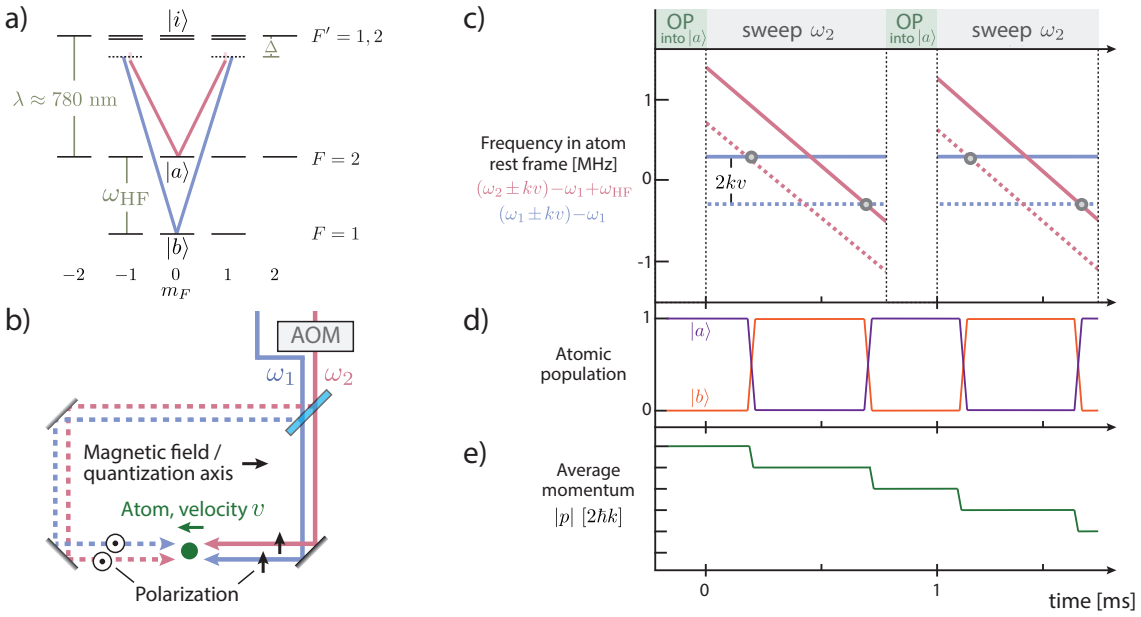


Figure 5.2: Experimental Setup and Cooling Procedure. (a) $^{87}$Rb level diagram. Two-photon transitions between $|a\rangle$ and $|b\rangle$ are induced by $\omega_1$ (blue) and $\omega_2$ (red). (b) Experimental layout. A moving atom (green) interacts with two pairs of counter-propagating laser beams (blue, red) with $\omega_2$ varied in a saw-tooth manner. (c) The four unique laser frequencies observed in the rest frame of the atom after including the Doppler shifts that separate counter-propagating lasers in frequency by $2kv$. Offsets have been subtracted so that points marked with circles correspond to allowed two-photon resonances which involve pairs of orthogonally-polarized, counter-propagating laser beams. (d) Two-photon Landau-Zener transitions transfer an atom from $|a\rangle$ to $|b\rangle$ and back to $|a\rangle$ each sweep. (e) The counter-propagating lasers and sweep direction ideally remove $4\hbar k$ momentum per cooling sweep.

detuned from the intermediate state $|i\rangle$ by an amount $\Delta \approx 2\pi \times 2$ GHz. The allowed two-photon transitions involve absorption and stimulated emission of pairs of orthogonal linearly polarized photons differing in frequency by the ground state hyperfine splitting of $\omega_{\mathrm{HF}} = 6.834$ GHz. The cooling beams incident from the left are vertically polarized and the beams incident from the right are horizontally polarized. Dipole selection rules disallow two-photon transitions with pairs of photons of the same linear polarization, *i.e.*, the only allowed two-photon Raman transitions are those that also impart a net photon recoil momentum $2\hbar k$ as the internal state changes.

Both beam directions have two distinct frequency components $\omega_1$ and $\omega_2$ (Fig. 5.2(b)) created by combining the output of two phase-locked lasers. We choose to hold the frequency $\omega_1$ fixed while the frequency component $\omega_2$ is swept linearly in time downward in frequency through the

two-photon atomic resonance at $\omega_1 - \omega_2 \approx \omega_{\mathrm{HF}}$.

Accounting for Doppler shifts of the laser frequencies as seen by an atom moving at speed $v$, there are two two-photon resonances that occur when $\delta(t) \equiv \omega_1 - \omega_2 - \omega_{\mathrm{HF}} = \pm 2kv$ (Fig. 5.2(c)). Ideal adiabatic passage through each resonance imparts a net momentum kick of $2\hbar k$ per transition, i.e., $4\hbar k$ per sweep. The direction of the frequency sweep is chosen such that the time ordering of the passage through the two resonance frequencies leads to a reduction of the atom's speed in the laboratory frame.

As the atom approaches zero speed and the Doppler shift is of the same order as $\Omega_{\mathrm{ab}}$, the time-ordering of the adiabatic transfers detailed above is invalid. Here, $\Omega_{\mathrm{ab}} \approx \frac{\Omega_1 \Omega_2}{2\Delta}$ is the two-photon Rabi frequency and $\Omega_1 \approx \Omega_2$ are the single photon Rabi frequencies of each frequency component. With the inevitable failure of a transfer, either due to broken time-ordering or imperfect adiabatic transfer, an atom can have considerable probability to be in $|b\rangle$ following a sweep so that the next iteration results in heating. We apply $\pi$-polarized optical pumping light for 100 $\mu$s to return any atoms remaining in $|b\rangle$ to $|a\rangle$ before the next frequency sweep. Optical pumping light is applied from a direction orthogonal to the cooling beams, and the duration could have been decreased.

In our experiment, around $10^7$ atoms are loaded into a magneto-optical trap (MOT) and pre-cooled to about 42 $\mu$K with polarization gradient cooling (PGC) to narrow the initial velocity distribution and lessen the requirements on the sweep's effective capture range. The atoms are optically pumped into $|a\rangle$. Frequency sweeps are then applied with typical sweep times of 1 ms and sweep range 1 MHz as shown in Fig. 5.2(c). The ideal internal state populations and change in momentum are shown in Fig. 5.2(d and e). This sequence of optical pumping and sweeping is repeated several times. The final 1D temperature of the atoms is measured by velocimetry. All atoms are optically pumped back to $|a\rangle$ and then velocity-selective Raman transitions drive atoms within a small velocity range into $|b\rangle$ [17]. The population in $|b\rangle$ is determined using fluorescence and the resulting Voigt profiles are fit to extract the temperature (Fig. 5.3(a)).

We observe cooling from an initial temperature of 42(3) $\mu$K to 10 $\mu$K after the application of 9 sweeps with fixed two-photon Rabi frequency $\Omega_{\mathrm{ab}} = 2\pi \times 22$ kHz and sweep range of $\Delta_{\mathrm{swp}} \equiv$

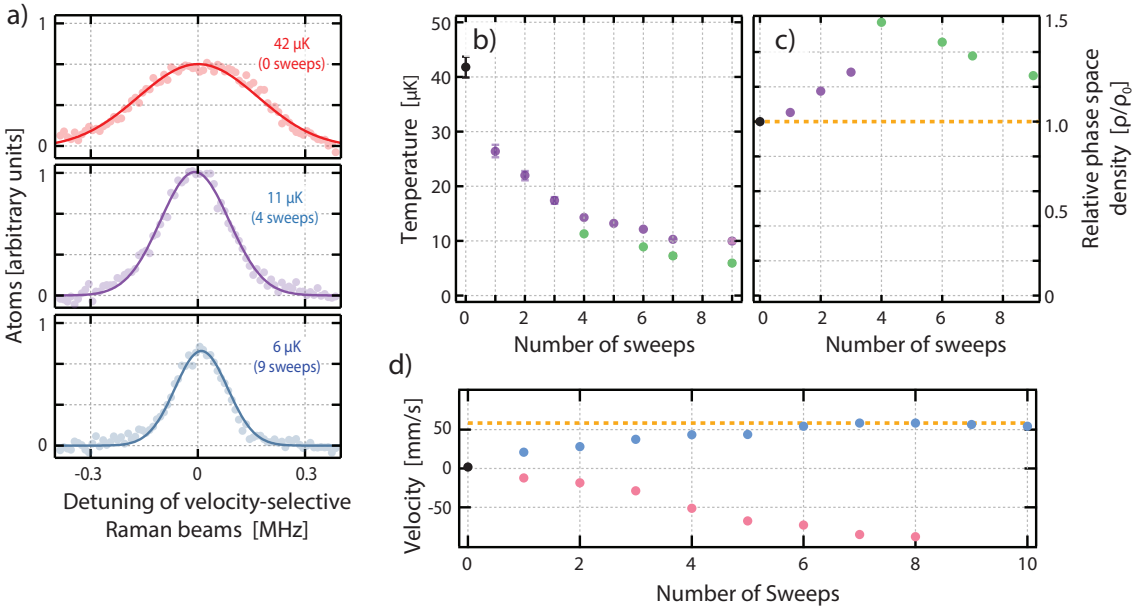


Figure 5.3: Performance of cooling. (a) The reduction in temperature is determined by measuring the initial velocity distribution (red) and the distribution after four and nine sweeps (purple and blue). The velocity distributions shown here are determined by driving Raman transitions that are only resonant for atoms in a narrow velocity-class whose center is set by the detuning of the Raman beams. (b) The atomic ensemble is cooled as low as 5.9 $\mu$K in one dimension over the course of several sweeps. For the purple points, all sweeps used a two-photon Rabi frequency $\Omega_{\mathrm{ab}} \approx 2\pi \times 22$ kHz and sweep range $\Delta_{\mathrm{swp}} = 2\pi \times 0.8$ MHz. For the green points, $\Omega_{\mathrm{ab}}$ and $\Delta_{\mathrm{swp}}$ were successively reduced between sweeps as described in the text. (c) The relative one-dimensional phase-space density for the corresponding purple or green points in (b). The phase-space density begins to decrease after four sweeps despite the decreasing temperature because atoms begin to leave the velocimetry beams. (d) To cool into a moving reference frame (blue points), we apply a frequency offset $\delta_{\mathrm{AOM}} = 2\pi \times 150$ kHz in the lab reference frame between the beams from opposite directions. By sweeping $\omega_2$ downwards, the atoms cool and equilibrate into a moving reference frame which has a velocity $v_F \equiv \delta_{\mathrm{AOM}}/2k$ (dashed orange line). If the sweep direction is reversed (pink points), the atoms accelerate in the opposite direction without being bound by $|v_F|$.

$2\pi \times 0.8\,\mathrm{MHz}$ (purple points in Fig. 5.3(b)). The sweep range is chosen to allow over 95% of the atoms to pass through two-photon resonance during the sweep when accounting for the Doppler shifts of the initial velocity distribution of the atoms.

The temperature can be reduced by progressively decreasing the two-photon Rabi frequency and the sweep range, as is done for the green points in Fig. 5.3(b). After the first three sweeps (purple points), the Rabi frequency is reduced to $\sqrt{0.5} \times \Omega_{\mathrm{ab}}$ and the the sweep range is reduced to $0.5 \times \Delta_{\mathrm{swp}}$ such that the Landau-Zener adiabaticity parameter $\xi$ (discussed below) is unchanged.

The sweep range can be reduced because the velocity distribution was reduced by the initial sweeps. After two sweeps, the remaining sweeps are performed with two-photon Rabi frequency $\sqrt{0.4}\times\Omega_{\mathrm{ab}}$ and sweep range $0.4\times\Delta_{\mathrm{swp}}$. After 9 total sweeps, the measured temperature reaches 5.9(3) $\mu$K.

An increase in phase-space density demonstrates a reduction of entropy and not merely a selective loss of atoms or a redistribution of the density in phase space. In Fig. 5.3(c), we see that the the relative 1D phase space density $\rho/\rho_0 = \Delta x_0 \Delta v_0/(\Delta x \Delta v)$ is increased, where $\Delta x$ and $\Delta v$ ($\Delta x_0$ and $\Delta v_0$) are the measured cloud size and velocity spread after (before) cooling.

Although the polarization scheme is reminiscent of polarization gradient cooling [30], here there is a large magnetic field present that breaks the degeneracy of the ground states that is typically required for polarization gradient cooling to such a low temperature. In addition, when the sweep direction was reversed, we observed heating as expected in the SWAP model of cooling.

To further emphasize the critical role of the sweep direction in the present work, we apply a fixed relative offset frequency $\delta_{\mathrm{AOM}}$ between the counter-propagating beams such that one would expect that atoms are cooled into a moving reference frame with velocity $v_F = \delta_{\mathrm{AOM}}/2k$. If the laser frequency is swept downward as was done for the cooling experiments above, we observe that the atoms are accelerated into and equilibrate into the moving frame (blue points in Fig. 5.3(d)). The orange dashed line indicates the velocity of the predicted moving frame for the applied frequency offset $\delta_{\mathrm{AOM}} = 2\pi \times 150\,\mathrm{kHz}$. In contrast, if we simply reverse the frequency sweep direction, we observe that the atoms are accelerated in the opposite direction despite the direction of the moving reference frame remaining unchanged (pink points of Fig. 5.3(d)). The atoms are accelerated to speeds larger than the calculated $|v_F|$ as expected.

## 5.3 Adiabatic Transfer in the Presence of Scattering

It is important to understand the possible limitations of using Raman transitions associated with the sweep rate $\alpha \equiv \mathrm{d}\omega_2/\mathrm{d}t$ being too fast or too slow. To achieve high quality adiabatic transfer, one would like to sweep slowly such that the ideal Landau-Zener diabatic transition probability is small, $P_d = e^{-\xi} \ll 1$ where $\xi = \frac{\pi}{2}\Omega_{\mathrm{ab}}^2/\alpha$. To avoid off-resonant spontaneous scattering of

light from the applied cooling laser beams, one would like the probability to have not scattered a photon during the total sweep time to be close to unity, $P_{\mathrm{sc}} = e^{-R_{\mathrm{sc}}\Delta_{\mathrm{swp}}/\alpha} \approx 1$. $R_{\mathrm{sc}}$ is the total spontaneous scattering rate from the far-from-resonance intermediate state(s).

In Fig. 5.4(a) (circles), we measure the probability to successfully transfer from $|a\rangle$ to $|b\rangle$ after a single adiabatic transfer using $\sigma^+$ polarized beams from a single direction and such that the two-photon Rabi frequency is the same as for the data in Fig. 5.3(b). The data shows that there is an optimum sweep rate $\alpha$ that maximizes the transfer efficiency as desired for efficient cooling. For comparison, the red dashed line is the predicted transfer efficiency $1 - P_{\mathrm{d}}$ ignoring free space scattering. The measurements qualitatively match predictions from numerically integrating optical-Bloch equations including spontaneous emission (Fig. 5.4(a) orange).

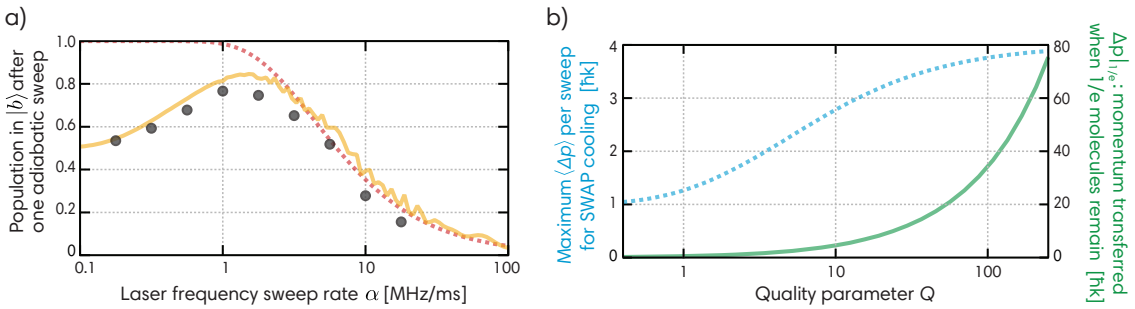


Figure 5.4: Characterization of adiabatic transfer and discussion of quanlity parameter Q. (a) Population in $|b\rangle$ after one adiabatic transfer attempt, measured using fluorescence detection (black points). Here, transitions were driven using co-propagating $\sigma^+$-polarized light with frequencies $\omega_1$ and $\omega_2$. $\omega_1$ was constant and $\omega_2$ was swept through resonance at different sweep rates $\alpha = \mathrm{d}\omega_2/\mathrm{d}t$. Transfers were performed with $(\Omega_{\mathrm{ab}}, \Gamma, \Delta, \Delta_{\mathrm{swp}}) = 2\pi \times (20\,\mathrm{kHz}, 6\,\mathrm{MHz}, 2\,\mathrm{GHz}, 0.8\,\mathrm{MHz})$. The familiar Landau-Zener prediction (red dashed) fails at low sweep rate due to off-resonant scattering from the intermediate state $|i\rangle$. A numerical simulation using the experimental parameters and including off-resonant scattering shows qualitative agreement (orange) with the data. (b, left) The achievable momentum transfer per SWAP cooling sweep (blue dashed) approaches the ideal $4\hbar k$ at large quality parameter $Q \equiv \frac{\pi}{2}\frac{\Omega^2}{\Gamma\Delta_{\mathrm{swp}}}$. (b, right) For SWAP cooling of molecules, we consider a worst-case scenario in which a molecule is lost if it undergoes a single spontaneous emission event. The predicted achievable momentum transfer when $1/e$ molecules remain (green) is shown versus the quality parameter $Q$.

To generalize predictions for how scattering will limit SWAP cooling, we consider the three-level system shown in Fig. 5.1(b). We will assume that the intermediate state $|i\rangle$ decays with equal

rates of $\Gamma/2$ into both $|b\rangle$ and $|a\rangle$. We also assume $\Omega_1 = \Omega_2 = \Omega$, and that the large detuning limit $\Delta \gg \Gamma, \Omega$ is satisfied. The two photon Rabi frequency is then $\Omega_{\rm ab} = \frac{\Omega^2}{2\Delta}$, and the total scattering rate is $R_{\rm sc} = \frac{\Gamma\Omega^2}{4\Delta^2}$. More details about the following treatment are provided in the Sec. 5.5.

We use this simplified system to find the optimum momentum transferred $\Delta p$ during a cooling sweep after optimizing for sweep rate $\alpha$. In Fig. 5.4(b, blue), we plot $\Delta p$ against a dimensionless quality parameter $Q \equiv \ln P_{\rm d}/\ln P_{\rm sc} \approx \frac{\pi}{2}\frac{\Omega^2}{\Gamma\Delta_{\rm swp}}$. When $Q \gg 1$, the momentum transfer per sweep saturates to the ideal value $4\hbar k$, and the effective force is $4\hbar k/t_{\rm swp}$, where the time to complete each sweep is $t_{\rm swp}$. At the optimized sweep rate, $t_{\rm swp} = \frac{8\ln(2Q)}{\pi}\frac{\Delta^2}{\Omega^4}\Delta_{\rm swp}$. In terms of experimentally controllable parameters, the quality factor scales with laser intensity $I$ and wavelength as $Q \propto I\lambda^3$, but does not depend on the dipole matrix element $M$ between the states $|b\rangle$, $|a\rangle$ and the intermediate state $|i\rangle$. The sweep time scales as roughly $t_{\rm swp} \propto \frac{\Delta^2}{M^4 I^2}\Delta_{\rm swp}$.

For cooling molecules, where avoiding spontaneous emission is of chief importance, one must understand how much momentum can be removed before the molecule is lost. We take the worst case scenario, where every molecule that spontaneously emits a photon is completely lost. In Fig. 5.4(b, green), we plot $\Delta p|_{1/e}$, the average momentum transfer when $1/e$ molecules remain, again numerically optimizing the sweep rate. For $Q \gg 1$, the numerical result is well approximated by $\Delta p|_{1/e} \approx \frac{2.1Q}{\ln(4(Q+14))}\hbar k$. By engineering systems with high quality parameter $Q$, one can remove many photon recoils of momentum from a molecule before it is likely to be lost. The optimized sweep time is nicely approximated by $t_{\rm swp} \approx \frac{\ln(4(14+Q))}{3.2}\frac{\Delta^2}{\Omega^4}\Delta_{\rm swp}$.

## 5.4 Conclusion

We have demonstrated that Raman transitions may be employed for SWAP cooling atoms without a single-photon narrow transition, achieving final temperatures well below the Doppler cooling limit. The technique is straightforward to implement, is amenable towards working in the presence of a large magnetic field, is robust against small changes in atomic transition frequency, and might prove useful for cooling molecules. Future work may look towards using the technique to cool in more dimensions or to manipulate ensembles via accelerations and decelerations. More

complex waveforms for the laser intensity and detuning could potentially decrease the required sweep range, increasing the effective cooling rate [4]. We have also identified a quality parameter $Q$ that provides guidance as to what experimental systems are needed for Raman SWAP cooling to work efficiently.

## 5.5 Discussions

As discussed in the main text, adiabatic transfer in the presence of scattering is optimized by a balance between the need to sweep slowly to preserve adiabaticity and the need to sweep fast enough to avoid significant scattering. Numerical simulations were used to better understand the dynamics and limitations of adiabatic passage. Here we consider a slightly simplified model: this atom (Fig. 5.5(a)) has stable ground states $|a\rangle$ and $|b\rangle$ and an optically excited state $|i\rangle$ that decays into them with equal probability at total rate $\Gamma$. The energy of these states are $\hbar\omega_{\mathrm{a}}$, $\hbar\omega_{\mathrm{b}}$, and $\hbar\omega_{\mathrm{i}}$. A laser at frequency $\omega_1(t)$ couples $|a\rangle \leftrightarrow |i\rangle$ with single-photon Rabi frequency $\Omega_1$, and a laser at frequency $\omega_2(t)$ couples $|b\rangle \leftrightarrow |i\rangle$ with Rabi frequency $\Omega_2$. The average detuning $\Delta$ of these lasers from the excited state is large compared to the two-photon detuning $\delta(t)$.

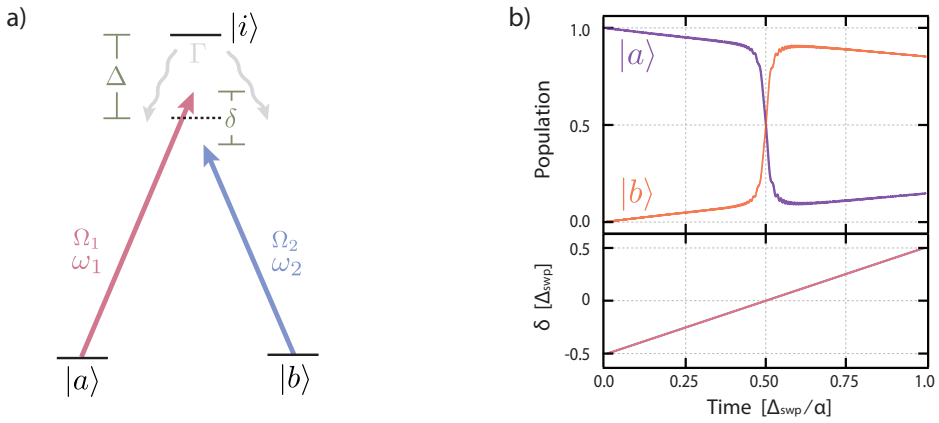


Figure 5.5: Simulated time dynamics of adiabatic transfer on a three-level system. (a) Diagram for simplified three-level system. An excited state $|i\rangle$ spontaneously decays equally to $|a\rangle$ and $|b\rangle$ at total decay rate $\Gamma$. Lasers connect $|a\rangle$ and $|b\rangle$ to a state detuned from $|i\rangle$ by $\Delta$. (b) Simulated time dynamics of adiabatic transfer, ignoring momentum states. In units of the scattering rate, the sweep range is $\Delta_{\mathrm{swp}} = \Gamma/3$, $\Delta = 300\Gamma$, $\Omega_{\mathrm{ab}} = \Gamma/150$. The scattering rate $\Gamma$ is responsible for the coherence decay.

### 5.5.1 Optical Bloch Equations and Adiabatic Elimination for a Three-Level Raman System

The density matrix describing this three-level system is

$$\rho = \begin{pmatrix} \rho_{\mathrm{ii}} & \rho_{\mathrm{ia}} & \rho_{\mathrm{ib}} \\ \rho_{\mathrm{ai}} & \rho_{\mathrm{aa}} & \rho_{\mathrm{ab}} \\ \rho_{\mathrm{bi}} & \rho_{\mathrm{ba}} & \rho_{\mathrm{bb}} \end{pmatrix}$$

and the Hamiltonian for this system can be written $\mathcal{H} = \mathcal{H}_A + V_1 + V_2$, with the interaction between an atom and a field provided by

$$\begin{aligned} V_1 &= -\mathbf{d}\cdot\mathbf{E}_1 \cos\left(\int_0^t \omega_1(t')dt'\right) \\ &= \frac{\hbar\Omega_1}{2}\left(|i\rangle\langle a|\left(e^{-i\int_0^t \omega_1(t')\,\mathrm{d}t'} + e^{i\int_0^t \omega_1(t')\,\mathrm{d}t'}\right) + |a\rangle\langle i|\left(e^{-i\int_0^t \omega_1(t')\,\mathrm{d}t'} + e^{i\int_0^t \omega_1(t')\,\mathrm{d}t'}\right)\right) \\ &\approx \frac{\hbar\Omega_1}{2}\left(|i\rangle\langle a|\, e^{i\int_0^t \omega_1(t')\,\mathrm{d}t'} + |g\rangle\langle i|\, e^{-i\int_0^t \omega_1(t')\,\mathrm{d}t'}\right) \\ \text{and} \qquad V_2 &\approx \frac{\hbar\Omega_2}{2}\left(|i\rangle\langle b|\, e^{i\int_0^t \omega_2(t')\,\mathrm{d}t'} + |b\rangle\langle i|\, e^{-i\int_0^t \omega_2(t')\,\mathrm{d}t'}\right) \end{aligned}$$

after making the rotating wave approximation, with $\hbar\Omega_1 \equiv -\langle g\,|\,\mathbf{d}\cdot\mathbf{E}_1\,|\,i\rangle$ and $\hbar\Omega_2 \equiv -\langle e\,|\,\mathbf{d}\cdot\mathbf{E}_2\,|\,i\rangle$ where

$$\begin{aligned} \omega_1(t) &= \omega_{\mathrm{i}} - \omega_{\mathrm{a}} + \Delta(t) + \frac{\delta(t)}{2} \\ \omega_2(t) &= \omega_{\mathrm{i}} - \omega_{\mathrm{b}} + \Delta(t) - \frac{\delta(t)}{2} \end{aligned}$$

such that $\Delta(t)$ is the average detuning of the lasers from their respective transitions. In our experiment and simulations, $\delta(t) = \alpha t - \frac{\Delta_{\mathrm{swp}}}{2}$ is swept linearly in time.

From the Liouville equation, $\dot{\rho} = \frac{i}{\hbar}[\rho, \mathcal{H}] - \gamma\rho$, with the dissipation term $\gamma$ representing population relaxation, the equations of motion for the coherences are

$$\dot{\rho}_{\mathrm{ia}} = -\left(i(\omega_{\mathrm{i}} - \omega_{\mathrm{a}}) + \frac{\Gamma}{2}\right)\rho_{\mathrm{ia}} + \frac{i\Omega_1 e^{-i\int_0^t \omega_1(t')\,\mathrm{d}t'}}{2}(\rho_{\mathrm{ii}} - \rho_{\mathrm{aa}}) - \frac{i\Omega_2 e^{-i\int_0^t \omega_2(t')\,\mathrm{d}t'}}{2}\rho_{\mathrm{ba}}, \tag{5.1}$$

$$\dot{\rho}_{\mathrm{ib}} = -\left(i(\omega_{\mathrm{i}} - \omega_{\mathrm{b}}) + \frac{\Gamma}{2}\right)\rho_{\mathrm{ib}} + \frac{i\Omega_2 e^{-i\int_0^t \omega_2(t')\,\mathrm{d}t'}}{2}(\rho_{\mathrm{ii}} - \rho_{\mathrm{bb}}) - \frac{i\Omega_1 e^{-i\int_0^t \omega_1(t')\,\mathrm{d}t'}}{2}\rho_{\mathrm{ab}}, \tag{5.2}$$

$$\dot{\rho}_{\mathrm{ba}} = -i\left(\omega_{\mathrm{b}} - \omega_{\mathrm{a}}\right)\rho_{\mathrm{ba}} + \frac{i\Omega_1 e^{-i\int_0^t \omega_1(t')\,\mathrm{d}t'}}{2}\rho_{\mathrm{bi}} - \frac{i\Omega_2 e^{i\int_0^t \omega_2(t')\,\mathrm{d}t'}}{2}\rho_{\mathrm{ia}}, \tag{5.3}$$

and for the populations, because the branching ratios from the intermediate state are balanced,

$$\dot{\rho}_{\mathrm{ii}} = \frac{i\Omega_1}{2}\left(e^{i\int_0^t \omega_1(t')\,\mathrm{d}t'}\rho_{\mathrm{ia}} - e^{-i\int_0^t \omega_1(t')\,\mathrm{d}t'}\rho_{\mathrm{ai}}\right) + \frac{i\Omega_2}{2}\left(e^{i\int_0^t \omega_2(t')\,\mathrm{d}t'}\rho_{\mathrm{ib}} - e^{-i\int_0^t \omega_2(t')\,\mathrm{d}t'}\rho_{\mathrm{bi}}\right) - \Gamma\rho_{\mathrm{ii}}, \tag{5.4}$$

$$\dot{\rho}_{\mathrm{aa}} = \frac{i\Omega_1}{2}\left(e^{-i\int_0^t \omega_1(t')\,\mathrm{d}t'}\rho_{\mathrm{ai}} - e^{i\int_0^t \omega_1(t')\,\mathrm{d}t'}\rho_{\mathrm{ia}}\right) + \frac{\Gamma}{2}\rho_{\mathrm{ii}}, \tag{5.5}$$

$$\dot{\rho}_{\mathrm{bb}} = \frac{i\Omega_2}{2}\left(e^{-i\int_0^t \omega_2(t')\,\mathrm{d}t'}\rho_{\mathrm{bi}} - e^{i\int_0^t \omega_2(t')\,\mathrm{d}t'}\rho_{\mathrm{ib}}\right) + \frac{\Gamma}{2}\rho_{\mathrm{ii}}. \tag{5.6}$$

To enter the rotating (natural) frame, the transformation to "slow" variables is used:

$$\rho_{\mathrm{ia}} = \tilde{\rho}_{\mathrm{ia}} e^{-i\int_0^t \omega_1(t')\,\mathrm{d}t'},$$

$$\rho_{\mathrm{ib}} = \tilde{\rho}_{\mathrm{ib}} e^{-i\int_0^t \omega_2(t')\,\mathrm{d}t'},$$

$$\rho_{\mathrm{ba}} = \tilde{\rho}_{\mathrm{ba}} e^{-i\left(\int_0^t \omega_1(t') - \omega_2(t')\,\mathrm{d}t'\right)}$$

Substituting these into Eqns. 5.1-5.3, the coherences in this frame become

$$\dot{\tilde{\rho}}_{\mathrm{ia}} = \left[i\left(\Delta(t) + \frac{\delta(t)}{2}\right) - \frac{\Gamma}{2}\right]\tilde{\rho}_{\mathrm{ia}} + \frac{i\Omega_1}{2}(\rho_{\mathrm{ii}} - \rho_{\mathrm{aa}}) - \frac{i\Omega_2}{2}\tilde{\rho}_{\mathrm{ba}},$$

$$\dot{\tilde{\rho}}_{\mathrm{ib}} = \left[i\left(\Delta(t) - \frac{\delta(t)}{2}\right) - \frac{\Gamma}{2}\right]\tilde{\rho}_{\mathrm{ib}} + \frac{i\Omega_2}{2}(\rho_{\mathrm{ii}} - \rho_{\mathrm{bb}}) - \frac{i\Omega_1}{2}\tilde{\rho}_{\mathrm{ab}},$$

$$\dot{\tilde{\rho}}_{\mathrm{ba}} = \frac{i\Omega_1}{2}\tilde{\rho}_{\mathrm{bi}} - \frac{i\Omega_2}{2}\tilde{\rho}_{\mathrm{ia}} + i\delta(t)\tilde{\rho}_{\mathrm{ba}}.$$

The populations of Eqns. 5.4-5.6 can be rewritten

$$\dot{\rho}_{\mathrm{ii}} = \frac{i\Omega_1}{2}\left(\tilde{\rho}_{\mathrm{ia}} - \tilde{\rho}_{\mathrm{ai}}\right) + \frac{i\Omega_2}{2}\left(\tilde{\rho}_{\mathrm{ib}} - \tilde{\rho}_{\mathrm{bi}}\right) - \Gamma\rho_{\mathrm{ii}}, \tag{5.7}$$

$$\dot{\rho}_{\mathrm{aa}} = \frac{i\Omega_1}{2}\left(\tilde{\rho}_{\mathrm{ai}} - \tilde{\rho}_{\mathrm{ia}}\right) + \frac{\Gamma}{2}\rho_{\mathrm{ii}}, \tag{5.8}$$

$$\dot{\rho}_{\mathrm{bb}} = \frac{i\Omega_2}{2}\left(\tilde{\rho}_{\mathrm{bi}} - \tilde{\rho}_{\mathrm{ib}}\right) + \frac{\Gamma}{2}\rho_{\mathrm{ii}}. \tag{5.9}$$

We now reduce the equations of motion to an effective two-level system by adiabatically eliminating $\rho_{\mathrm{ia}}$ and $\rho_{\mathrm{ib}}$. This is justified when the population of the intermediate state is small, which is valid when $\Delta \gg \Gamma, \delta$. The time derivatives $\dot{\tilde{\rho}}_{\mathrm{ia}}$, $\dot{\tilde{\rho}}_{\mathrm{ii}}$, and $\dot{\tilde{\rho}}_{\mathrm{ib}}$ are set to zero, and hence

$$\tilde{\rho}_{\mathrm{ia}} = \frac{i\Omega_1}{\Gamma + 2i\Delta(t) - i\delta(t)}\left(\rho_{\mathrm{ii}} - \rho_{\mathrm{aa}}\right) - \frac{i\Omega_2}{\Gamma + 2i\Delta(t) - i\delta(t)}\tilde{\rho}_{\mathrm{ba}},$$

$$\tilde{\rho}_{\mathrm{ib}} = \frac{\Omega_2}{\Gamma + 2i\Delta(t) + i\delta(t)}\left(\rho_{\mathrm{ii}} - \rho_{\mathrm{bb}}\right) - \frac{\Omega_1}{\Gamma + 2i\Delta(t) + i\delta(t)}\tilde{\rho}_{\mathrm{ab}}.$$

These coherences are substituted into Eqns. 5.7-5.9, and after transforming back into the original coordinates, we arrive at the final set of Bloch equations

$$\dot{\rho}_{\mathrm{aa}} = \frac{\Gamma\rho_{\mathrm{ii}}}{2} + \frac{\Gamma\Omega_1^2\left(\rho_{\mathrm{ii}} - \rho_{\mathrm{aa}}\right)}{\Gamma^2 + (2\Delta(t) + \delta(t))^2} - \frac{\Omega_1\Omega_2}{2}\left(\frac{\tilde{\rho}_{\mathrm{ba}}}{\Gamma - 2i\Delta(t) - i\delta(t)} + \frac{\tilde{\rho}_{\mathrm{ab}}}{\Gamma + 2i\Delta(t) + i\delta(t)}\right),$$

$$\dot{\rho}_{\mathrm{bb}} = \frac{\Gamma\rho_{\mathrm{ii}}}{2} + \frac{\Gamma\Omega_2^2\left(\rho_{\mathrm{ii}} - \rho_{\mathrm{bb}}\right)}{\Gamma^2 + (2\Delta(t) - \delta(t))^2} - \frac{\Omega_1\Omega_2}{2}\left(\frac{\tilde{\rho}_{\mathrm{ba}}}{\Gamma + 2i\Delta(t) - i\delta(t)} + \frac{\tilde{\rho}_{\mathrm{ab}}}{\Gamma - 2i\Delta(t) + i\delta(t)}\right),$$

$$\dot{\tilde{\rho}}_{\mathrm{ba}} = i\delta(t)\tilde{\rho}_{\mathrm{ba}} - \frac{\tilde{\rho}_{\mathrm{ba}}}{2}\left(\frac{\Omega_1^2}{\Gamma + 2i\Delta(t) - i\delta(t)} + \frac{\Omega_2^2}{\Gamma - 2i\Delta(t) - i\delta(t)}\right) - \frac{\Omega_1\Omega_2}{2}\left(\frac{\rho_{\mathrm{bb}} - \rho_{\mathrm{ii}}}{\Gamma + 2i\Delta(t) - i\delta(t)} + \frac{\rho_{\mathrm{aa}} - \rho_{\mathrm{ii}}}{\Gamma - 2i\Delta(t) - i\delta(t)}\right)$$

with

$$\rho_{\mathrm{ii}} \approx \frac{\Omega_1^2\rho_{\mathrm{aa}} + \Omega_2^2\rho_{\mathrm{bb}} + \Omega_1\Omega_2\tilde{\rho}_{\mathrm{ba}} + \Omega_1\Omega_2\tilde{\rho}_{\mathrm{ab}}}{\Gamma^2 + 4\Delta(t)^2 + \Omega_1^2 + \Omega_2^2}. \tag{5.10}$$

Equation 5.10 has been greatly simplified by the assumption that $\delta(t) \ll \Delta(t), \Omega_1, \Omega_2$.

### 5.5.2 Including Internal Momentum States

We now include the momentum states of an atom, using a second label such as $|a, 0\hbar k\rangle$. The basis of states is truncated to only include $0\hbar k, 1\hbar k, 2\hbar k, \ldots, (m-1)\hbar k$ momentum states, so the density matrix becomes $2m \times 2m$. Terms that are non-physical, involving a momentum transfer with no change of state, can also be negated:

$$\rho = \begin{pmatrix}
\ddots & \vdots & & \vdots & \ddots & \vdots & & \vdots & \\
\cdots & \rho_{\mathrm{aa}00} & 0 & 0 & \cdots & \rho_{\mathrm{ab}00} & \rho_{\mathrm{ab}01} & \rho_{\mathrm{ab}02} & \cdots \\
 & 0 & \rho_{\mathrm{aa}11} & 0 & & \rho_{\mathrm{ab}10} & \rho_{\mathrm{ab}11} & \rho_{\mathrm{ab}12} & \\
\cdots & 0 & 0 & \rho_{\mathrm{aa}22} & \cdots & \rho_{\mathrm{ab}20} & \rho_{\mathrm{ab}21} & \rho_{\mathrm{ab}22} & \cdots \\
\ddots & \vdots & & \vdots & \ddots & \vdots & & \vdots & \ddots \\
\cdots & \rho_{\mathrm{ba}00} & \rho_{\mathrm{ba}01} & \rho_{\mathrm{ba}02} & \cdots & \rho_{\mathrm{bb}00} & 0 & 0 & \cdots \\
 & \rho_{\mathrm{ba}10} & \rho_{\mathrm{ba}11} & \rho_{\mathrm{ba}12} & & 0 & \rho_{\mathrm{bb}11} & 0 & \\
\cdots & \rho_{\mathrm{ba}20} & \rho_{\mathrm{ba}21} & \rho_{\mathrm{ba}22} & \cdots & 0 & 0 & \rho_{\mathrm{bb}22} & \cdots \\
 & \vdots & & \vdots & \ddots & \vdots & & \vdots & \ddots
\end{pmatrix}$$

Normal adiabatic passage from $|a, 0\hbar k\rangle$ through $|i, 1\hbar k\rangle$ to $|b, 2\hbar k\rangle$ is represented in the matrix elements

$$\dot{\rho}_{\mathrm{aa00}} = \frac{\Gamma\rho_{\mathrm{ii00}}}{2} + \frac{\Gamma\Omega_1^2\left(\rho_{\mathrm{ii11}} - \rho_{\mathrm{aa00}}\right)}{\Gamma^2 + (2\Delta(t) + \delta(t))^2} - \frac{\Omega_1\Omega_2}{2}\left(\frac{\tilde{\rho}_{\mathrm{ba20}}}{\Gamma - 2i\Delta(t) - i\delta(t)} + \frac{\tilde{\rho}_{\mathrm{ab02}}}{\Gamma + 2i\Delta(t) + i\delta(t)}\right),$$

$$\dot{\rho}_{\mathrm{bb22}} = \frac{\Gamma\rho_{\mathrm{ii22}}}{2} + \frac{\Gamma\Omega_2^2\left(\rho_{\mathrm{ii11}} - \rho_{\mathrm{bb22}}\right)}{\Gamma^2 + (2\Delta(t) - \delta(t))^2} - \frac{\Omega_1\Omega_2}{2}\left(\frac{\tilde{\rho}_{\mathrm{ba20}}}{\Gamma + 2i\Delta(t) - i\delta(t)} + \frac{\tilde{\rho}_{\mathrm{ab02}}}{\Gamma - 2i\Delta(t) + i\delta(t)}\right),$$

$$\dot{\tilde{\rho}}_{\mathrm{ba20}} = \frac{\tilde{\rho}_{\mathrm{ba20}}}{2}\left(2i\delta(t) - \frac{\Omega_1^2}{\Gamma + 2i\Delta(t) - i\delta(t)} - \frac{\Omega_2^2}{\Gamma - 2i\Delta(t) - i\delta(t)}\right) - \frac{\Omega_1\Omega_2}{2}\left(\frac{\rho_{\mathrm{bb22}} - \rho_{\mathrm{ii11}}}{\Gamma + 2i\Delta(t) - i\delta(t)} + \frac{\rho_{\mathrm{aa00}} - \rho_{\mathrm{ii11}}}{\Gamma - 2i\Delta(t) - i\delta(t)}\right)$$

with

$$\rho_{\mathrm{ii11}} \approx \frac{\Omega_1^2\rho_{\mathrm{aa00}} + \Omega_2^2\rho_{\mathrm{bb22}} + \Omega_1\Omega_2\tilde{\rho}_{\mathrm{ba20}} + \Omega_1\Omega_2\tilde{\rho}_{\mathrm{ab02}}}{\Gamma^2 + 4\Delta(t)^2 + \Omega_1^2 + \Omega_2^2}.$$

Other momentum states are coupled in due to the scattering terms. For example, $|b, 2\hbar k\rangle$ may absorb a photon, losing $\hbar k$ of momenta, and enter $|a, 1\hbar k\rangle$. This state may in turn decay incoherently to $|a, 1\hbar k\rangle$ or $|b, 1\hbar k\rangle$.

Because the momentum states are now distinguishable within the density matrix, we can separate atoms that undergo adiabatic passage without scattering from other possibilities (Fig. 5.6). We can also construct expectation values for the momentum change.

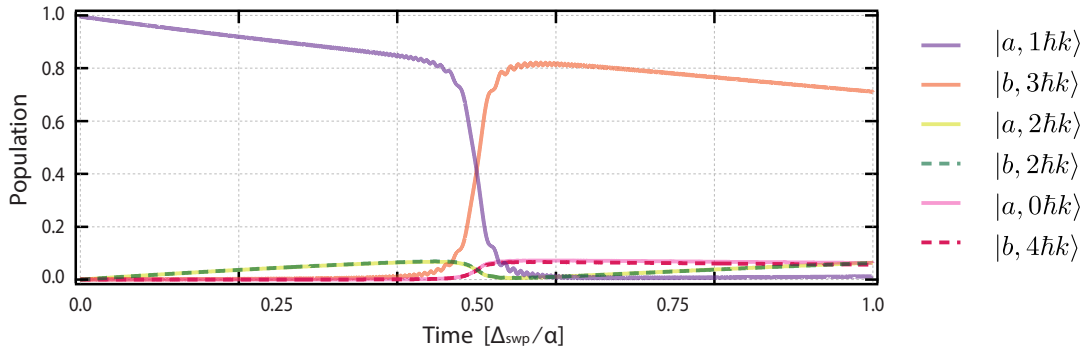


Figure 5.6: Simulation of populations including momentum labels during adiabatic transfer. The parameters used match those of Fig. 5.5(b). The expected change in momentum at the end of the adiabatic transfer is $1.71\hbar k$.

A Runge-Kutta fourth-order numerical integration method is used to simulate adiabatic transfer (Fig. 5.5(b)). In practice, we find a $10 \times 10$ density matrix is sufficient, and population

starts in $|a, 1\hbar k\rangle$ ($\rho_{\mathrm{aa11}}$). When determining final populations, oscillations in the simulation can become significant, so we take the average of during the last 1/30th of time steps. This leads to a slight error due to the average slope during this time. To find the expected change of momentum, we compute

$$\langle \Delta p(\Gamma, \Delta, \Omega, \Delta_{\mathrm{swp}})_{\mathrm{AT}} \rangle = \left[ \sum_n n\, \hbar k \left( \rho_{bbnn} + \rho_{aann} \right) \right] - 1\hbar k.$$

Finally, this model ignores effects such as laser noise and atomic dephasing which can set substantial limitations on transfer fidelity [63, 78]. In Fig. 5.4(a), a separate two-level simulation was used which allowed us to enter this dephasing by hand. However, these details are beyond the scope of this model.

### 5.5.3 Probabilitistic Model for Raman SWAP Cooling

Adiabatic transfer from $|a\rangle$ to $|b\rangle$ adds $2\hbar k$ momentum from an atom, and transfer from $|b\rangle$ to $|a\rangle$ removes $2\hbar k$ momentum. If we assume that during a scattering process, absorption from $|a\rangle$ adds one photon's worth of momentum, and absorption from $|b\rangle$ removes one photon's worth momentum, but decay into either state causes no coherent momentum change, then to first-order, the possible change in momentum is detailed in Table. 5.1. The first-order expected change in momentum, from summing the tabulated momentum changes multiplied by the probability of that trajectory, is found to be

$$\langle \Delta p_{\mathrm{AT}} \rangle = \left(1 + x - 2x^{1+Q}\right) \times \hbar k$$

with $x \equiv e^{-R_{\mathrm{sc}} \frac{\Delta_{\mathrm{swp}}}{\alpha}}$, $R_{\mathrm{sc}} = \frac{\Gamma\Omega^2}{\Gamma^2 + 4\Delta^2 + 2\Omega^2} \approx \frac{\Gamma\Omega^2}{4\Delta^2}$, and $Q \equiv \frac{\pi}{2} \frac{\Omega^2}{\Gamma \Delta_{\mathrm{swp}}}$. Numerical simulations of the previous section serve to validate this model exceptionally well.

The momentum transfer during a full SWAP cooling sweep comes from cooling during the first half of the sweep, and cooling or heating during the second half depending on if an atom successfully transferred from $|a\rangle$ to $|b\rangle$. The expected momentum transfer during a full cooling

| **Row** | **Before** $T/2$ | **At** $T/2$ | **After** $T/2$ | **Probability** | $\Delta p$ |
|---|---|---|---|---|---|
| 1 | Scatter to $\|b\rangle$ | Transfer to $\|a\rangle$ | Scatter | $\frac{1}{2}SAS$ | $0\,\hbar k$ |
| 2 | Scatter to $\|b\rangle$ | Transfer to $\|a\rangle$ | No scatter | $\frac{1}{2}SA(1-S)$ | $-1\,\hbar k$ |
| 3 | Scatter to $\|b\rangle$ | No transfer | Scatter | $\frac{1}{2}S(1-A)S$ | $0\,\hbar k$ |
| 4 | Scatter to $\|b\rangle$ | No transfer | No scatter | $\frac{1}{2}S(1-A)(1-S)$ | $1\,\hbar k$ |
| 5 | Scatter to $\|a\rangle$ | Transfer to $\|b\rangle$ | Scatter | $\frac{1}{2}SAS$ | $2\,\hbar k$ |
| 6 | Scatter to $\|a\rangle$ | Transfer to $\|b\rangle$ | No scatter | $\frac{1}{2}SA(1-S)$ | $3\,\hbar k$ |
| 7 | Scatter to $\|a\rangle$ | No transfer | Scatter | $\frac{1}{2}S(1-A)S$ | $2\,\hbar k$ |
| 8 | Scatter to $\|a\rangle$ | No transfer | No scatter | $\frac{1}{2}S(1-A)(1-S)$ | $1\,\hbar k$ |
| 9 | No scatter | Transfer to $\|b\rangle$ | Scatter | $(1-S)AS$ | $1\,\hbar k$ |
| 10 | No scatter | Transfer to $\|b\rangle$ | No scatter | $(1-S)A(1-S)$ | $2\,\hbar k$ |
| 11 | No scatter | No transfer | Scatter | $(1-S)(1-A)S$ | $1\,\hbar k$ |
| 12 | No scatter | No transfer | No scatter | $(1-S)(1-A)(1-S)$ | $0\,\hbar k$ |

Table 5.1: First-order possibilities for atom state trajectories. An atom starts in $|a\rangle$ and may scatter before time $T/2$. At time $T/2$, adiabatic transfer may occur. From $T/2$ to $T$, the atom may scatter again. The probability to undergo adiabatic transfer is $A \equiv 1-\exp\left(-\frac{\pi}{2}\frac{\Omega_{\rm ab}^2}{\alpha}\right)$, and the probability to scatter is $S \equiv 1-\exp\left(-R_{\rm sc}\frac{\Delta_{\rm swp}}{2\alpha}\right)$ with scattering rate $R_{\rm sc} = \frac{\Gamma\Omega^2}{\Gamma^2+4\Delta^2+2\Omega^2} \approx \frac{\Gamma\Omega^2}{4\Delta^2}$.

sweep is then $\langle\Delta p_{\rm SWAP}\rangle = \langle\Delta p_{\rm AT}\rangle\,(1+(P(e)-P(g)))$. The fraction of atoms cooled vs. heated in the second half of the sweep is represented by $(P(e)-P(g))$, where $P(a)$ is the probability to be in state $|a\rangle$ at the conclusion of the first half of the sweep. We find

$$\langle\Delta p_{\rm SWAP}\rangle = \langle\Delta p_{\rm AT}\rangle\left(1+x(1-2x^Q)\right). \tag{5.11}$$

To evaluate the benefits of SWAP cooling over Doppler cooling, we would like to know how much momentum could be removed before an atom (or molecule) detrimentally scatters a photon. Although we assumed equal branching ratios up until now, suppose that every scattering event causes an atom to be lost. We assume each atom scatters one photon from optical repumping if it finishes the cooling sweep in $|b\rangle$. The expected change in momentum per sweep comes entirely from the events of Table. 5.1 row 10 and 12:

$$\left\langle\Delta p'_{\rm AT}\right\rangle = (1-S)A(1-S)\times 2\hbar k = x(1-x^Q)\times 2\hbar k.$$

To be consistent, we need to normalize this to the number of atoms remaining in the system:

$$\begin{aligned}
\langle \Delta p_{\mathrm{AT}} \rangle &= \frac{\langle \Delta p'_{\mathrm{AT}} \rangle}{(1-S)A(1-S) + (1-S)(1-A)(1-S)} \\
&= (1 - x^Q) \times 2\hbar k \\
\langle \Delta p_{\mathrm{SWAP}} \rangle &= \langle \Delta p_{\mathrm{AT}} \rangle \times [1 + ((1-S)A(1-S) - (1-S)(1-A)(1-S))] \\
&= \left(1 + x - x^Q - 3x^{1+Q} + 2x^{1+2Q}\right) \times 2\hbar k
\end{aligned}$$

Next we choose to find the average momentum transferred per atom at a time when $1/e$ atoms remain, with the assumption that any scattering event will cause the atom to be lost. The two ways an atom does not scatter a photon (during the sweep or from optical repumping) come again from rows 10 and 12:

$$P(\text{no scatter}) = \left[(1-S)A(1-S)\right]^2 + \left[(1-S)(1-A)(1-S)\right]^2.$$

Let the probability that an atom survives $n$ sweeps be $1/e$; then the momentum change for an atom at the point when it has probability $1/e$ not to be lost is

$$\begin{aligned}
n \langle \Delta p_{\mathrm{SWAP}} \rangle &= \frac{\langle \Delta p_{\mathrm{SWAP}} \rangle}{-\ln\left(P(\text{no scatter})\right)} \\
&= \left( \frac{(1-x^Q)(x(2x^Q-1)-1)}{\ln\left(x^2 + 2x^{Q+2}(x^Q-1)\right)} \right) \times 2\hbar k. \qquad (5.12)
\end{aligned}$$

This function is plotted in Fig. 5.7(b) for $Q = 25$ and maximized with respect to sweep rate in Fig. 5.4(b).

The optimal sweep rate for transferring momentum in the model where scattering is unimportant is found by taking the derivative of Eq. (5.11) with respect to $\alpha$ and equating it to zero:

$$\alpha_{\mathrm{opt}} \approx \frac{\pi}{2} \frac{\Omega^4}{4\Delta^2} \frac{1}{\ln\left[2\left(1+Q\right)\right]}. \qquad (5.13)$$

However, the optimal sweep rate for transferring momentum before atoms are lost to recoiled photons Eq. (5.12) could only be found numerically (Fig. 5.7(a)). The scaling at significant $Q$

remains the same as in Eq. (5.13) – the optimal sweep rate can be increased as roughly $\Omega^4/\Delta^2$ (though $Q$ also changes as $\Omega^2$).

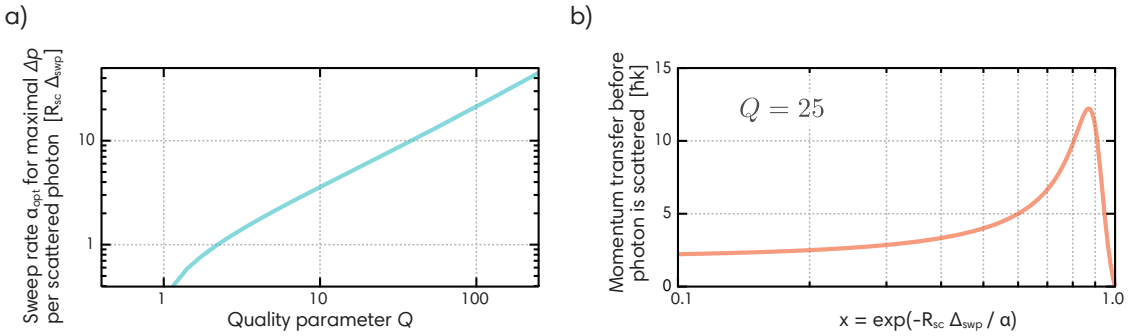


Figure 5.7: Optimization of experimental parameters with Q. (a) The momentum transferred during a single simulated SWAP cooling sweep was found and maximized with respect to the sweep rate $\alpha$. When the quality parameter $Q$ is very small, the ideal strategy is to sweep very slowly in order to coherently scatter once. When $Q$ is large, efficient adiabatic sweeps are possible. (b) The maximum momentum transferable before a photon scatters due to Raman cooling beams or optical pumping beams.

# Chapter 6

# Continuous Real-time Tracking of a Quantum Phase below the Standard Quantum Limit

In this chapter, I will present a theoretical proposal for countinuous tracking of a quantum phase, which could function as an alternative to the Ramsey sequence. Quantum nondemolition measurements of a lossy cavity mode interacting with an atomic ensemble are used to directly probe the quantum phase of the collective atomic spin without converting it into a population difference. Spin-squeezed states in phase quadrature develop naturally with long enough measurement time [99]. This work is in collaboration with Dr. Athreya Shankar and Prof. Murray Holland. I will reproduce the text of ref. [99] closely in Sec. 6.1 to introduce the background and summarize the main conclusions, but then go on to discuss a mean-field picture to provide some additional intuition. I will focus on a proposed implementation in $^{87}$Rb and technical requirements needed to implement the scheme later.

## 6.1 Introduction

Quantum systems have become robust platforms for metrology and tests of fundamental physics. Many applications rely on the dynamics of pseudospin-1/2 systems with two long-lived quantum states, $|\uparrow\rangle$ and $|\downarrow\rangle$. After preparing an equal superposition of these two states, a physical interaction is studied by investigating its effect on the relative phase $\phi(t)$, with the state of each spin evolving in time as $|\psi(t)\rangle = \left(|\downarrow\rangle + e^{i\phi(t)}|\uparrow\rangle\right)/\sqrt{2}$. We propose a novel scheme that enables continuous tracking of this relative phase. Our scheme continuously and directly measures the

real-time phase $\phi(t)$ unlike the widely used Ramsey sequence [86, 77, 49, 56, 2, 89, 98, 105, 87, 45, 40, 37], which indirectly measures the net accumulated phase $\phi(T)$ during an interrogation time $T$. The typically destructive readout in a Ramsey sequence requires multiple state resets, rotations and repetitions of the sequence to infer the phase at different times from a population difference. In contrast, a single run of our protocol yields a continuous time series of phase measurements. Therefore, our scheme enables real-time tracking of time-varying signals that are not reproducible.

As an added benefit, our scheme yields continuous phase estimates with precision well beyond the standard quantum limit (SQL) of $\Delta\phi_{\mathrm{SQL}} = 1/\sqrt{N}$ radians that limits readout precision with $N$ unentangled spins. In comparison to several proposals and experiments [61, 65, 96, 62, 11, 27, 51] that have demonstrated squeezed states with precision beyond the SQL, our scheme enjoys the advantage that the squeezing is produced, the phase accumulated, and the readout performed, all in the same spin quadrature.

Recent experiments have demonstrated phase tracking of a spin using quantum nondemolition (QND) measurements via a Faraday rotation angle [24]. In contrast, our proposal is based on interfering Raman transitions in a cavity and enables an intuitive interpretation of phase tracking in terms of elementary atom-cavity interactions that nearly balance one another. Our scheme directly reveals a phasor precessing in the equatorial plane of a Bloch sphere, in the spirit of the "hand on a clock" analogy at the core of quantum metrology.

## 6.2 Overview of Theoretical Proposal

We represent the collective angular momentum of $N$ atomic spins by a classical Bloch vector of length $N/2$ with components $J_x$, $J_y$, $J_z$ (Fig. 6.1(d, left)). With all spins initially in the same equal superposition state, the Bloch vector lies in the equatorial plane along a direction that we define as the $y$-axis. As the phase evolves, the Bloch vector acquires a small $x$-component, $J_x = \frac{N}{2}\sin\phi(t) \approx \frac{N}{2}\phi(t)$, for small deflections, and we propose a straightforward extension to large deflections in the conclusion. We arrange atom-cavity interactions wherein a cavity field quadrature is sourced by $J_x$. Continuous homodyne detection of this quadrature amounts to real-

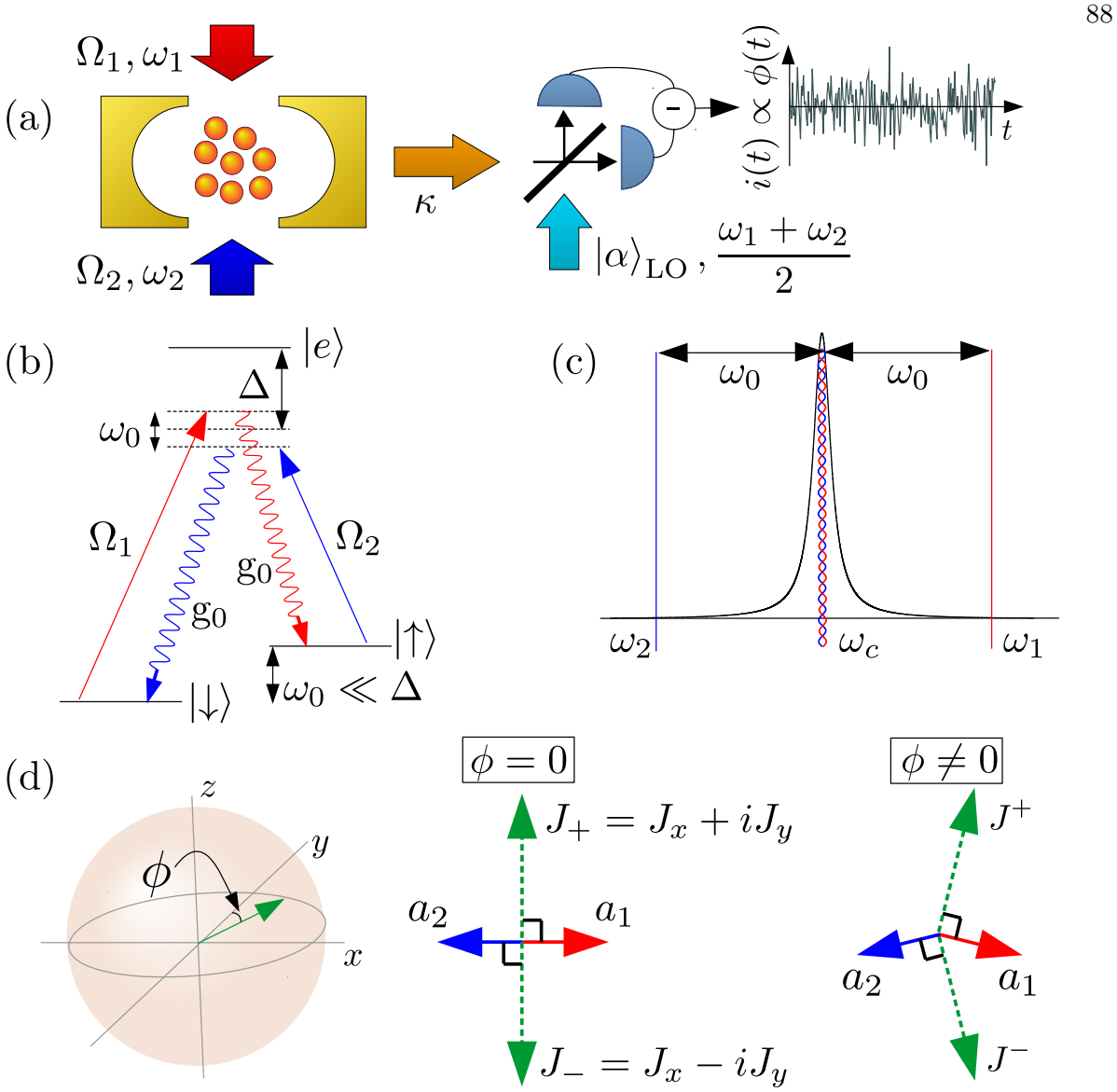


Figure 6.1: Schematic and working principle. (a) Two lasers drive a collection of atoms to interact with a cavity mode. The relative phase $\phi(t)$ can be continuously tracked by homodyne detection of the field leaking out. (b) Cavity-assisted Raman transitions: The red (blue) pathway leads to the emission of a cavity photon accompanied by a spin flip $|\downarrow\rangle \to |\uparrow\rangle$ ($|\uparrow\rangle \to |\downarrow\rangle$). (c) Hierarchy of frequencies. (d) Classical Bloch vector picture: The red and blue pathways set up balanced, opposing superradiance pathways that lead to a coherent cancellation of the intracavity field when the Bloch vector (green) is along the $y$-axis ($\phi = 0$). When the Bloch vector has a small $x$-component ($\phi \neq 0$), the intracavity field from the two pathways add constructively, giving rise to non-zero output field.

time, continuous, QND measurement of $\phi(t)$.

We consider $N$ atoms trapped at the antinodes of a cavity with resonance frequency $\omega_c$ and

decay rate $\kappa$, as shown in Fig. 6.1(a). The states $|\downarrow\rangle$ and $|\uparrow\rangle$ have an energy separation $\hbar\omega_0 \gg \hbar\kappa$ and form a pseudospin-1/2 system described by the Pauli spin operators $\hat{\sigma}_i$, $i = x, y, z$, with raising (lowering) operators $\hat{\sigma}_+$ ($\hat{\sigma}_-$). The $N$ atoms form a collective spin with total angular momentum components $\hat{J}_x, \hat{J}_y, \hat{J}_z$, with $\hat{J}_i = \sum_{j=1}^{N} \hat{\sigma}_i^j/2$. We assume the dipole-allowed transitions $|\downarrow\rangle \leftrightarrow |e\rangle$ and $|\uparrow\rangle \leftrightarrow |e\rangle$ with frequencies $\omega_{\downarrow e}$ and $\omega_{\uparrow e}$ to be respectively driven using lasers with frequencies $\omega_1$ and $\omega_2$ in a far-detuned regime with detuning $\Delta \gg \omega_0, \kappa$, allowing for the adiabatic elimination of $|e\rangle$ [55]. The two drive lasers differ by a frequency $2\omega_0$ (Fig. 6.1(c)) and do not by themselves drive $|\downarrow\rangle \leftrightarrow |\uparrow\rangle$ Raman transitions; however, they are symmetrically detuned by $\omega_0$ from $\omega_c$ and participate in cavity-assisted Raman transitions as illustrated in Fig. 6.1(b). When the Rabi frequencies of the two drive lasers are balanced, i.e. $\Omega_1 = \Omega_2 = \Omega_0$, the atom-cavity Hamiltonian, to leading order in $1/\Delta$, is simply the sum of a Jaynes-Cummings and an anti-Jaynes-Cummings interaction and is given by

$$\hat{H}_{\mathrm{QND}} = \frac{\hbar\Omega_{\mathrm{QND}}}{2}\hat{X}\hat{J}_x. \tag{6.1}$$

Here $\hat{X} = (\hat{a} + \hat{a}^\dagger)/\sqrt{2}$ is the amplitude quadrature, with $\hat{a}, \hat{a}^\dagger$ the annihilation and creation operators for the cavity mode, and $\hat{Y} = (\hat{a} - \hat{a}^\dagger)/\sqrt{2}i$ is the conjugate phase quadrature such that $[\hat{X}, \hat{Y}] = i$. The atom-cavity interaction strength is $\Omega_{\mathrm{QND}} = \sqrt{2}\Omega_0 g_0/\Delta$ with $g_0$ the single atom-cavity vacuum Rabi frequency. If the two drive lasers have initial phases $\psi_1$ and $\psi_2$, the cavity quadrature $\left(\hat{a}^\dagger e^{i(\psi_1+\psi_2)/2} + \text{ H.c.}\right)$ is coupled to the spin component $\left(\hat{J}_+ e^{i(\psi_1-\psi_2)/2} + \text{ H.c.}\right)$, where $\hat{J}_+ = \hat{J}_x + i\hat{J}_y$. Here we assume $\psi_1 = \psi_2 = 0$ without loss of generality.

Classically, the intracavity fields established by the two balanced drives exactly cancel when $J_x = 0$ (Fig. 6.1(d)). However, even with $\left\langle \hat{J}_x \right\rangle = 0$, $\left\langle \hat{J}_x^2 \right\rangle \neq 0$, i.e. quantum fluctuations source the $Y$ quadrature of the cavity field. In the regime $\kappa^2 \gg N\Omega_{\mathrm{QND}}^2$, $\hat{Y}$ is slaved to $\hat{J}_x$ as

$$\hat{Y}(t) \approx -\frac{\Omega_{\mathrm{QND}}}{\kappa}\hat{J}_x(t) + \hat{\mathcal{F}}(t), \tag{6.2}$$

where the noise operator $\hat{\mathcal{F}}(t)$ arises from coupling of the cavity mode to external modes through the lossy mirror (Fig. 6.1(a)) [107, 72]. The field leaking out is to be monitored via balanced homodyne detection using a local oscillator at frequency $(\omega_1 + \omega_2)/2$ with phase tuned to detect

the output field quadrature that is sourced by the intracavity $Y$ quadrature. The photocurrent thus recorded is a measurement of the $Y$ quadrature which, from Eq. (6.2), amounts to measuring $J_x$.

The precision of the phase estimate in a window is determined by the window duration. A characteristic time, $T_0 = (\eta C \gamma_{\rm sc})^{-1}/(N/4)$, is the time required to average down the measurement noise of $J_x$ to the standard quantum limit $\Delta J^2_{x,\rm SQL} = N/4$, with $\eta$ the quantum efficiency of the detection system. In principle, we could improve the precision with longer measurement window duration, until free space scattering becomes significant and degrades the precision by inducing random rotation about the z-axis, Raman spin flips and atom loss.

## 6.3 Mean-field Picture

We try to understand the mechanism in a mean-field picture. Consider a cavity-assisted superradiance process on a Raman transition as shown in Fig. 6.2 [10]. After loading atoms into $|\uparrow\rangle$, we could expect cavity-assisted superradiance[1] if the frequency of the cavity is tuned such that the cavity vacuum field and the dressing laser (indicated by the straight line) is on resonance with a two-photon Raman transition from $|\uparrow\rangle$ to $|\downarrow\rangle$.

The Hamiltonian of the Raman superradiance process is [12]

$$\begin{aligned}\hat{H} &= \hbar\omega_c \hat{c}^\dagger \hat{c} + \hbar\omega_e \hat{N}_e + \hbar\omega_\uparrow \hat{N}_\uparrow + \hbar\omega_\downarrow \hat{N}_\downarrow \\ &\quad + \hbar\frac{\Omega}{2}\left(\hat{J}_{e\uparrow} e^{-i\omega_1 t - \psi_1} + \text{H.C.}\right) + \hbar g\left(\hat{c}^\dagger \hat{J}_{\downarrow e} + \text{H.C.}\right), \end{aligned} \tag{6.3}$$

where $\hat{c}$ and $\hat{c}^\dagger$ are creation and annihilation operators of the cavity field, $\hbar\omega_e$, $\hbar\omega_\uparrow$ and $\hbar\omega_\downarrow$ are the energy of $|e\rangle$, $|\uparrow\rangle$ and $|\downarrow\rangle$, $\hat{N}_e$, $\hat{N}_\uparrow$ and $\hat{N}_\downarrow$ are the number operators of $|e\rangle$, $|\uparrow\rangle$ and $|\downarrow\rangle$, $\Omega$ is the Rabi frequency of the driving laser, $2g$ is the cavity vacuum Rabi frequency, $\hat{J}_{e\uparrow} = |e\rangle\langle\uparrow|$ and $\hat{J}_{\downarrow e} = |\downarrow\rangle\langle e|$.

[1] The collective emission rate must also be larger than atomic decoherence rates.

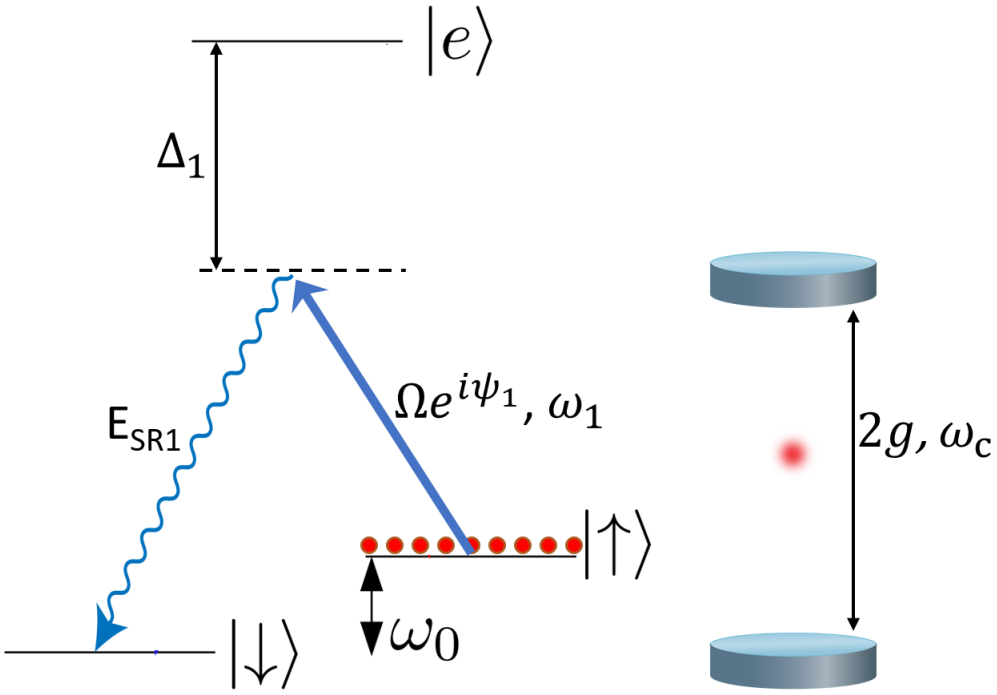


Figure 6.2: Cavity-assisted Raman superradiance. The red dots represent atoms. The dressing laser ($\Omega e^{i\psi_1}$) and the emission light ($E_{SR1}$) are indicated by the straight and wavy lines respectively. The cavity resonance is tuned near the frequency of the emission light. The frequency of the dressing laser is $\omega_1$. The cavity resonance is $\omega_c$. The cavity vacuum Rabi frequency is $2g$. The energy splitting between $|\downarrow\rangle$ and $|\uparrow\rangle$ is $\hbar\omega_0$.

After adiabatic elimination, with the help of Heisenberg equations of motion and assuming that atoms in $|\uparrow\rangle$ don't interact with the emission cavity mode, we get

$$\dot{\hat{c}} = \left(-\frac{\kappa}{2} - i\left(\frac{g^2}{\Delta_1}N_\downarrow + \omega_c\right)\right)\hat{c} - i\frac{g\Omega}{2\Delta_1}\hat{J}_- e^{-i\omega_1 t - \psi_1}, \tag{6.4}$$

where $\hat{J}_- = |\downarrow\rangle\langle\uparrow|$ and $\kappa$ is the linewidth of the cavity.

When the cavity field and the driving laser are on resonance with the two-photon Raman transition, we have

$$\hat{\mathcal{C}} = -i\frac{g\Omega/2\Delta_1}{\kappa/2}\hat{\mathcal{J}}_- e^{-i\psi_1}, \tag{6.5}$$

where $\hat{\mathcal{C}} = \hat{c}e^{-i\omega_c t}$ and $\hat{\mathcal{J}}_- = \hat{J}_- e^{-i\omega_c t}$, in steady state $\dot{\mathcal{C}} = 0$.

Now we consider the case when we drive two paths of superradiance from $|\uparrow\rangle$ to $|\downarrow\rangle$ and from $|\downarrow\rangle$ to $|\uparrow\rangle$ at the same time as shown in Fig. 6.3.

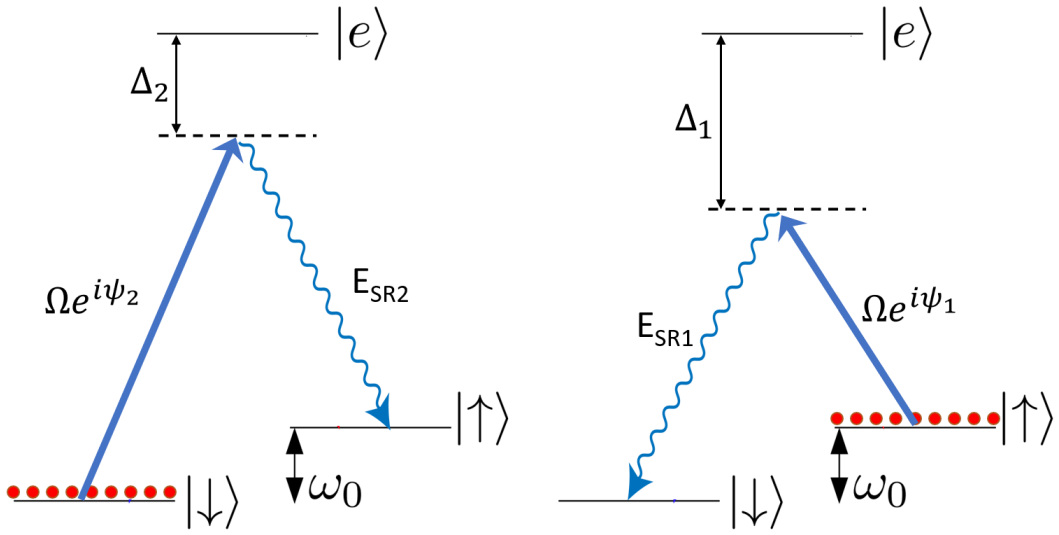


Figure 6.3: Driving two paths of superraidance at the same time. Left is the superradiance from $|\downarrow\rangle$ to $|\uparrow\rangle$. Right is the superradiance from $|\uparrow\rangle$ to $|\downarrow\rangle$.

For the superradiance from $|\downarrow\rangle$ to $|\uparrow\rangle$, we have $\hat{\mathcal{C}}^\dagger = -i\frac{g\Omega/2\Delta_2}{\kappa/2}\hat{\mathcal{J}}_+ e^{-i\psi_2}$.

In the limit $\Delta_1 \approx \Delta_2 \approx \Delta \gg \omega_0$, the total emission field $E_{tot} = E_{SR1} + E_{SR2}$ takes the form

$$E_{tot} = -i\frac{g\Omega/2\Delta}{\kappa/2}e^{-i\frac{\psi_1+\psi_2}{2}}(e^{i\frac{\psi_1-\psi_2}{2}}\hat{\mathcal{J}}_+ + e^{-i\frac{\psi_1-\psi_2}{2}}\hat{\mathcal{J}}_-), \tag{6.6}$$

which is the same as the general form discussed in the paragraph below Eq. (6.1). The field we want to monitor for continuous phase tracking results from the interference of the two superradiance paths from $|\uparrow\rangle$ to $|\downarrow\rangle$ and from $|\downarrow\rangle$ to $|\uparrow\rangle$ in the mean-field picture. Remember that $\hat{\mathcal{J}}_+ = \hat{\mathcal{J}}_x + i\hat{\mathcal{J}}_y$ and $\hat{\mathcal{J}}_- = \hat{\mathcal{J}}_x - i\hat{\mathcal{J}}_y$, Eq. (6.7) can be rewritten as

$$E_{tot} = -i\frac{g\Omega/2\Delta}{\kappa/2}e^{-i\frac{\psi_1+\psi_2}{2}}2\left(\cos\left(\frac{\psi_1-\psi_2}{2}\right)\hat{\mathcal{J}}_x - \sin\left(\frac{\psi_1-\psi_2}{2}\right)\hat{\mathcal{J}}_y\right), \tag{6.7}$$

which says that $\hat{\mathcal{J}}_x$ and $\hat{\mathcal{J}}_y$ couple to different quadratures of the emission field.

## 6.4 Implementation in $^{87}$Rb

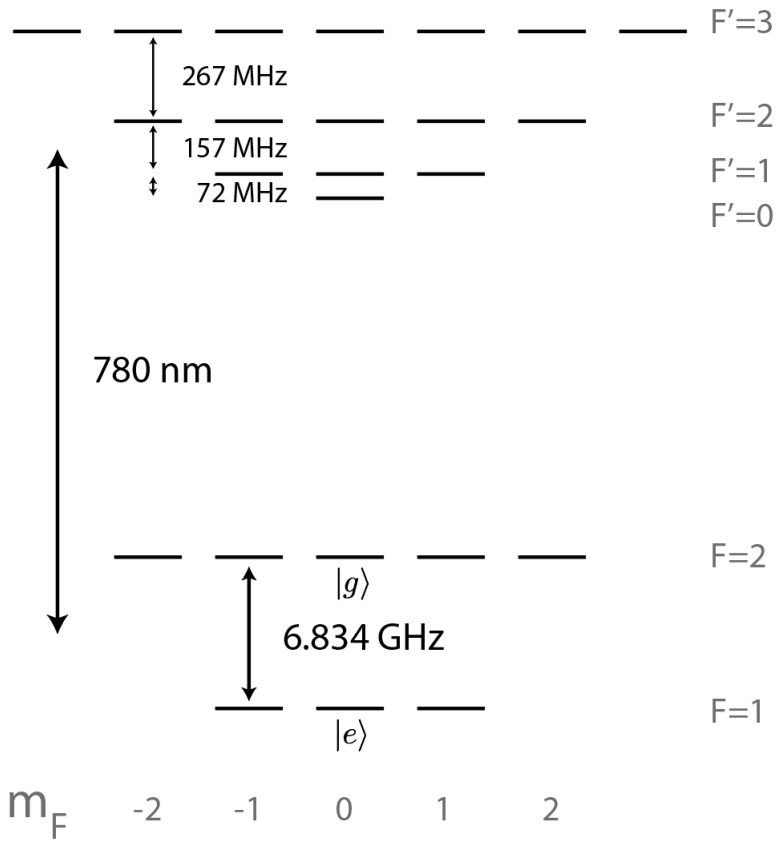


Figure 6.4: Level diagram for $^{87}$Rb D2 line

The level diagram of $^{87}$Rb D2 line is shown in Fig. 6.4. At first sight, one may expect to implement the phase tracking experiment with $|F=1, m_F=-1\rangle$ and $|F=1, m_F=1\rangle$ as $|\downarrow\rangle$ and $|\uparrow\rangle$. However this choice is difficult because the two-photon transition between the two states is forbidden in the limit the detuning from the excited state $\Delta \gg \omega_{HF,e}$, the excited hyperfine splitting of $^{87}$Rb. Instead, we propose an experiment based on spin-1 systems realized with the F=1 manifold.

I will first explain how to understand the quantum phase in spin-1 systems. I will then present our scheme, and give some numerical results with proposed parameters. Finally, I will discuss some technical requirements needed for the implementation.

### 6.4.1 Quantum Phase in Spin-1 Systems

Here we provide two ways to understand how the quantum phase $\phi$ appears in a spin 1 system.

#### 6.4.1.1 Understanding Quantum Phase with Wavefunctions

The wavefunction of a spin-1/2 system in an equal superposition state in the Dicke basis $|J, m_J\rangle$ is

$$|\theta = 90^\circ, \phi\rangle = \frac{1}{\sqrt{2}}(|1/2, -1/2\rangle + e^{-i\phi}\,|1/2, 1/2\rangle), \tag{6.8}$$

according to Eq. (3.1).

Likewise, in a spin-1 system, we have

$$|\theta = 90^\circ, \phi\rangle = \frac{1}{2}(|1, -1\rangle + \sqrt{2}e^{-i\phi}\,|1, 0\rangle + e^{-i2\phi}\,|1, 1\rangle), \tag{6.9}$$

so the quantum phase in spin-1 systems is just the phase difference between adjacent energy levels $\phi$ as shown in Eq. (6.9).

We can also reproduce the same sets of equations for spin-1 systems (see Fig. 6.5) as those for spin-1/2 system, from Eq. (6.3) to Eq. (6.5).

If the vacuum Rabi frequency for $|g_1\rangle$ to $|e_1\rangle$ transition is $2g_1$ and that for $|g_2\rangle$ to $|e_2\rangle$ transition is $2g_2$, the Hamiltonian for spin-1 Raman superradiance can be written as

$$\begin{aligned}\hat{H} = {} & \hbar\omega_c\hat{c}^\dagger\hat{c} + \hbar\omega_{e1}\hat{N}_{e1} + \hbar\omega_{e2}\hat{N}_{e2} + \hbar\omega_{g0}\hat{N}_{g0} + \hbar\omega_{g1}\hat{N}_{g1} + \hbar\omega_{g2}\hat{N}_{g2} \\ & + \hbar\frac{\Omega_1}{2}\left(\hat{J}_{e_1g_0}e^{-i\omega_1 t-\phi_1} + \text{H.C.}\right) + \hbar g_1\left(\hat{c}^\dagger\hat{J}_{g_1e_1} + \text{H.C.}\right) \\ & + \hbar\frac{\Omega_2}{2}\left(\hat{J}_{e_2g_1}e^{-i\omega_1 t-\phi_2} + \text{H.C.}\right) + \hbar g_2\left(\hat{c}^\dagger\hat{J}_{g_2e_2} + \text{H.C.}\right).\end{aligned} \tag{6.10}$$

After adiabatic elimination and assuming that atoms in $|g_0\rangle$ don't interact with the emission cavity mode, we get

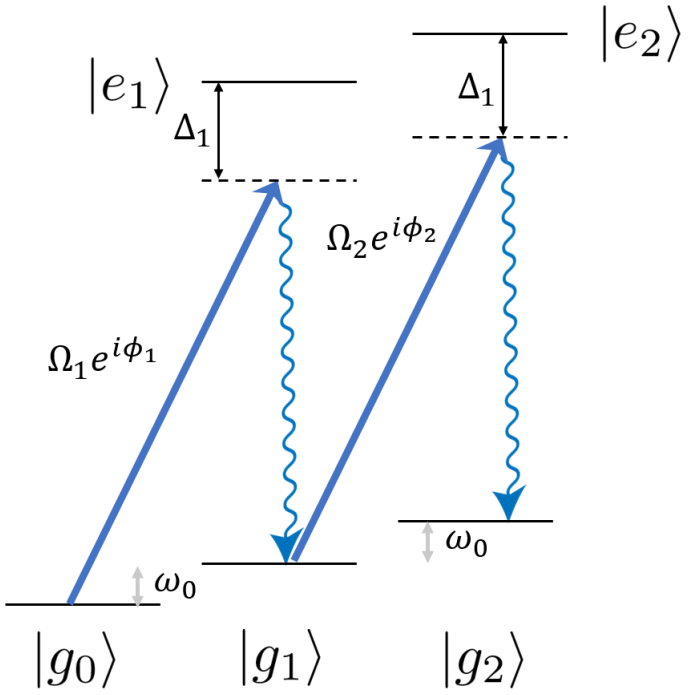


Figure 6.5: Raman superradiance in spin-1 systems

$$\dot{\hat{c}} = \left(-\frac{\kappa}{2} - i\left(\frac{g_1^2}{\Delta_1}N_{g_1} + \frac{g_2^2}{\Delta_1}N_{g_2} + \omega_c\right)\right)\hat{c} - i\frac{g_1\Omega_1}{2\Delta_1}\hat{J}_{g0g1}e^{-i\omega_1 t-\phi_1} - i\frac{g_2\Omega_2}{2\Delta_1}\hat{J}_{g1g2}e^{-i\omega_1 t-\phi_2}, \quad (6.11)$$

where $J_{g0g1} = |g0\rangle\langle g1|$ and $J_{g1g2} = |g1\rangle\langle g2|$. Notice that both $J_{g0g1}$ and $J_{g1g2}$ can be denoted with $J_-$.

If $g_1\Omega_1 = g_2\Omega_2$ and $\phi_1 = \phi_2$, we have

$$\hat{\mathcal{C}} = -2i\frac{g_1\Omega_1/2\Delta_1}{\kappa/2}\hat{\mathcal{J}}_- e^{-i\phi_1}, \quad (6.12)$$

where $\hat{\mathcal{C}} = \hat{c}e^{-i\omega_c t}$ and $\hat{\mathcal{J}}_- = \hat{J}_- e^{-i\omega_c t}$, in steady state $\dot{\mathcal{C}} = 0$, when the two-photon transition is driven resonantly.

Eq. (6.12) takes the same form as Eq. (6.5) up to numerical prefactors, so we should expect the same phase tracking performance for spin-1 systems as that in spin-1/2 systems.

#### 6.4.1.2 Understanding Quantum Phase with Spin Components

In spin-1/2 systems, the quantum phase $\phi$ can be defined with $\left\langle \hat{J}_x \right\rangle$ and $\left\langle \hat{J}_y \right\rangle$ as

$$\phi = \tan^{-1}\left(\left\langle \hat{J}_x \right\rangle / \left\langle \hat{J}_y \right\rangle\right), \tag{6.13}$$

where $\langle\rangle$ denotes expectation values, because the dynamics of the three spin components $\hat{J}_x$, $\hat{J}_y$ and $\hat{J}_z$ follow rigid body rotations on the Bloch sphere during Rabi flopping. I will show that the three spin components still follow rigid body rotations for spin-1 systems.

If we denote the three Zeeman sublevels of the spin-1 system in $^{87}$Rb as $|1\rangle$, $|2\rangle$ and $|3\rangle$, and represent a quantum state $|\phi\rangle = a\,|1\rangle + b\,|2\rangle + c\,|3\rangle$ with a vector $(a, b, c)$, we could represent the three spin components of spin-1 systems $\hat{L}_x$, $\hat{L}_y$ and $\hat{L}_z$ in matrix forms as shown below,

$$\hat{L}_x = \frac{1}{\sqrt{2}} \begin{pmatrix} 0 & 1 & 0 \\ 1 & 0 & 1 \\ 0 & 1 & 0 \end{pmatrix}, \tag{6.14}$$

$$\hat{L}_y = \frac{i}{\sqrt{2}} \begin{pmatrix} 0 & -1 & 0 \\ 1 & 0 & -1 \\ 0 & 1 & 0 \end{pmatrix}, \tag{6.15}$$

$$\hat{L}_z = \begin{pmatrix} 1 & 0 & 0 \\ 0 & 0 & 0 \\ 0 & 0 & -1 \end{pmatrix}. \tag{6.16}$$

The Hamiltonian describing the on-resonance Rabi flopping of a spin-1 system reads

$$\hat{H} = -\frac{\hbar\Omega}{2}\hat{L}_x = -\frac{\hbar\Omega}{2\sqrt{2}} \begin{pmatrix} 0 & 1 & 0 \\ 1 & 0 & 1 \\ 0 & 1 & 0 \end{pmatrix}. \tag{6.17}$$

From Eq. (6.17), we could get the the population evolution (Fig. 6.6).

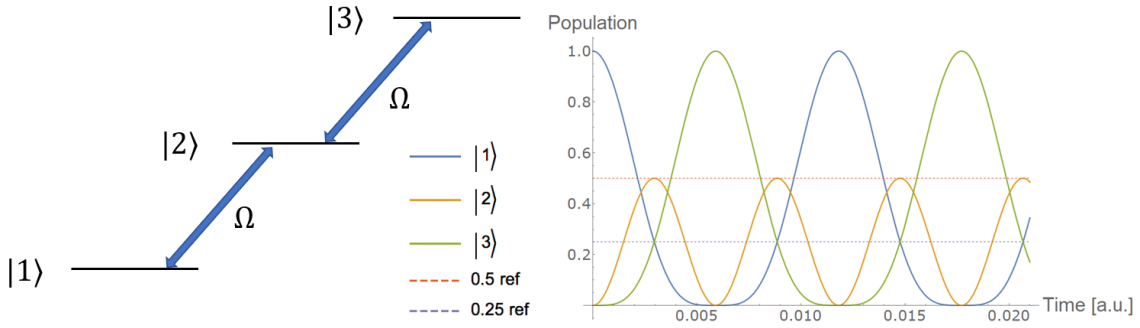


Figure 6.6: Population evolution of spin-1 systems. Horizontal axis is time. Vertical axis is population.

We could further get the evolution of the three spin components $\left\langle \hat{L}_x \right\rangle^2$, $\left\langle \hat{L}_y \right\rangle^2$ and $\left\langle \hat{L}_z \right\rangle^2$, as shown in Fig. 6.7. The rigid body rotation of the three spin components still holds for spin-1 systems, so we can still define the quantum phase as $\phi = \tan^{-1}\left(\langle L_x \rangle / \langle L_y \rangle\right)$.

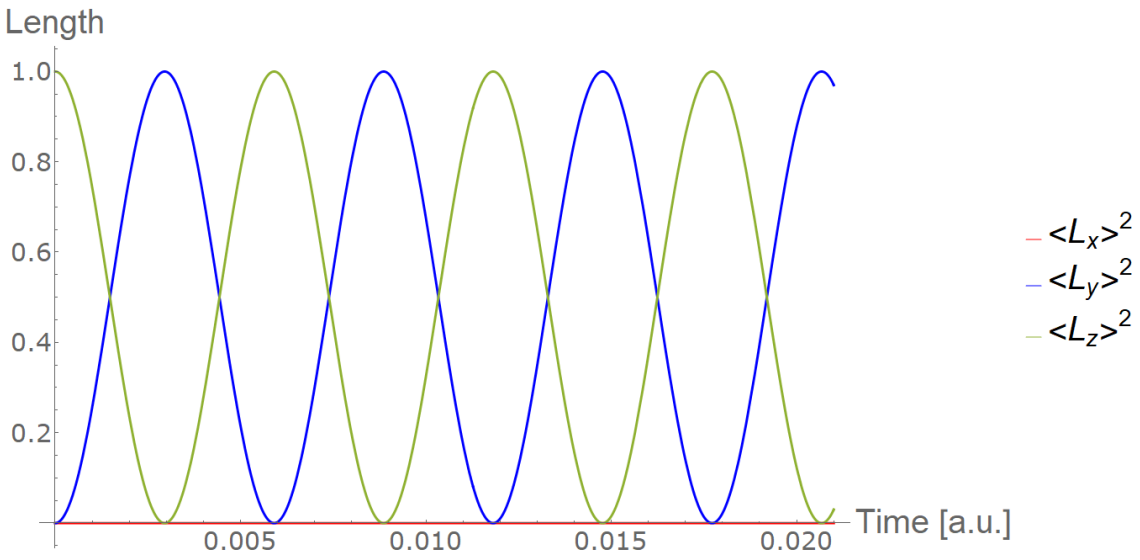


Figure 6.7: Evolution of the three spin components. Horizontal axis is time. Vertical axis is the length of the corresponding spin components.

### 6.4.2 Experimental Scheme and Numerical Results

The schematic diagram of continuous trakcing of a quantum phase with spin-1 systems implemented on $^{87}$Rb D2 line can be found in Fig. 6.8. We have a single ended cavity, whose transimission at the open port is more than 20 times that of the closed port. We plan to drive the Raman transitions through the open port at both $\omega_1$ and $\omega_2$, and detect the emitted field at the cavity resonance $\omega_c$ through the open port with homodyne detection (see Fig. 6.8c).

The quantization axis and the laser polarizations are shown in Fig. 6.8d. There will be off-resonant emissions from the $\sigma_-$ component of the blue driving tone and the $\sigma_+$ component of the orange driving tone. These off-resonance emissions, which are detuned by $\pm 2\omega_0$ from the cavity resonance, are suppressed by $(2\omega_0/(\kappa/2))^2$ from the resonant emission. The typical suppression is more than 5000 times, so we simply ignore it.

The parameters we propose to try are listed in Table. 6.1.

| Parameter | Description | Value |
|---|---|---|
| $\Delta$ | Detuning of the dressing laser from F' (see Eq. (6.7)) | 63 GHz |
| $\omega_0$ | Energy difference between adjacent Zeeman sublevels | 1 MHz |
| $P_1$ | Power in the blue driving tone at frequency $\omega_1$ | 10 $\mu$W |
| $P_2$ | Power in the orange driving tone at frequency $\omega_2$ | 10 $\mu$W |

Table 6.1: Proposed parameters for continuous phase tracking experiment

We could calculate the 4 two-photon Rabi frequencies from the proposed parameters, as shown in Eq. (6.18) to Eq. (6.21), the AC Stark shifts the three Zeeman sublevels get, as shown in Eq. (6.22) to Eq. (6.24), and the free space scattering rate, as shown in Eq. (6.25).

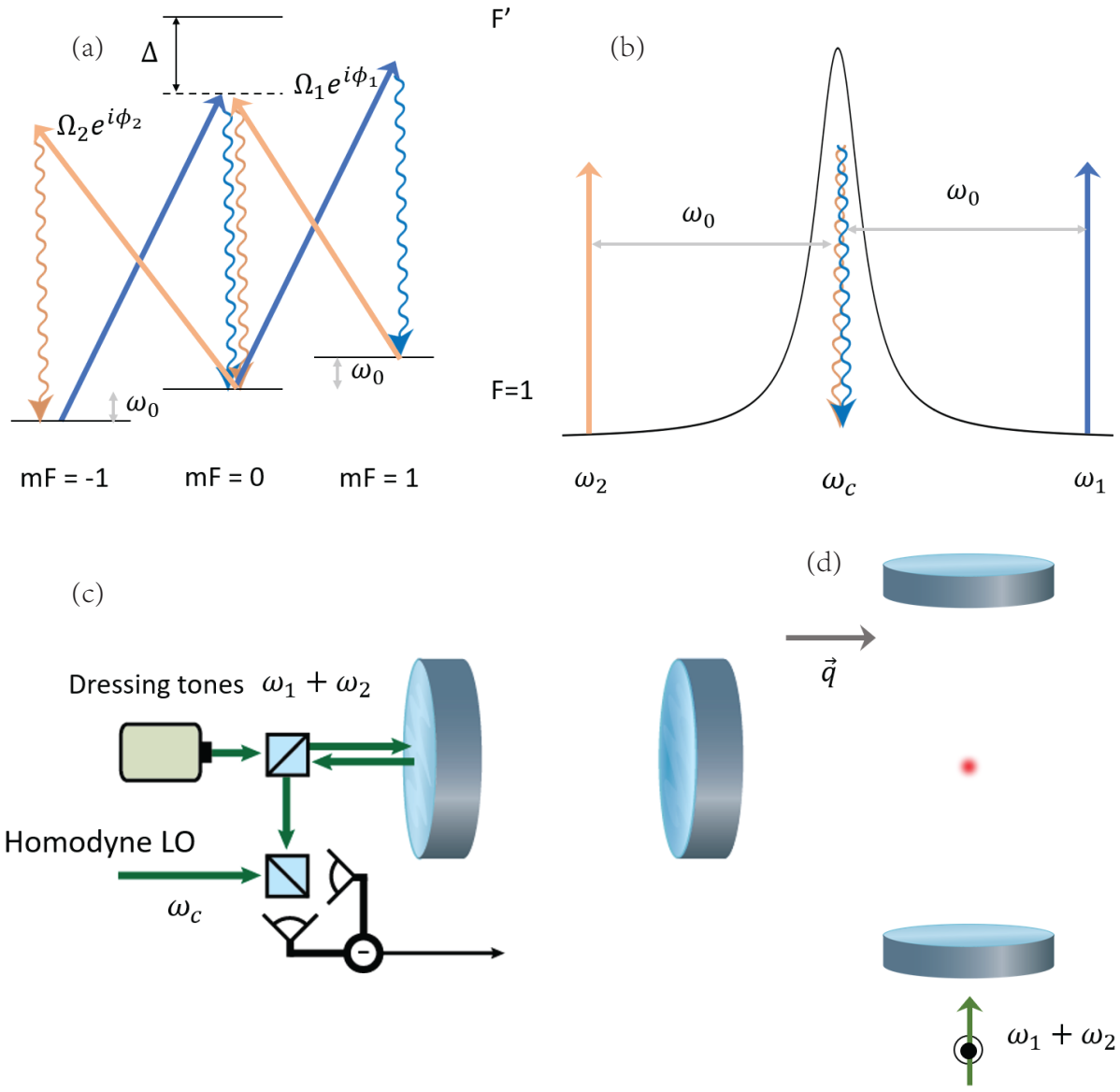


Figure 6.8: Schematic diagram of continuous trakcing of a quantum phase with spin-1 systems. (a) Relevant energy levels of $^{87}$Rb and two dressing lasers are presented. The emission field is indicated with wavy lines. (b) Hierarchy of frequencies. (c) Homodyne detection implementation is shown. The dressing tones have frequency components at $\omega_1$ and $\omega_2$. The frequency of the LO is at $\omega_c$, which is the average of the two frequencies in the dressing tones. (d) Quantization axis and laser polarizations are shown. The quantization axis is indicated by $\vec{q}$. The polarizations of the two beams are both perpendicular to the paper.

$$\Omega_{2ph,\ m_F=-1,\ m_F=0,\ \sigma_+} = 2\pi \times 119.2 \text{ Hz} \tag{6.18}$$

$$\Omega_{2ph,\ m_F=0,\ m_F=1,\ \sigma_+} = 2\pi \times 119.1 \text{ Hz} \tag{6.19}$$

$$\Omega_{2ph,\ m_F=1,\ m_F=0,\ \sigma_-} = 2\pi \times 119.2 \text{ Hz} \tag{6.20}$$

$$\Omega_{2ph,\ m_F=0,\ m_F=-1,\ \sigma_-} = 2\pi \times 119.1 \text{ Hz}. \tag{6.21}$$

$$\delta_{AC,\ m_F=-1} = 2\pi \times 8392.0 \text{ Hz} \tag{6.22}$$

$$\delta_{AC,\ m_F=0} = 2\pi \times 8391.4 \text{ Hz} \tag{6.23}$$

$$\delta_{AC,\ m_F=1} = 2\pi \times 8392.0 \text{ Hz}. \tag{6.24}$$

$$R_{FSS,\ m_F=-1} = R_{FSS,\ m_F=0} = R_{FSS,\ m_F=1} = 2\pi \times 2.15 \text{ Hz}. \tag{6.25}$$

The typical detection quantum efficiency is 10%, so the time for resolving the SQL is estimated to be $T_0 = 330.0$ $\mu$s. The time for creating 3 dB squeezing is thus $2T_0$. The decoherence from free space scattering during $2T_0$ is less than 3%, so we should be able to observe direct phase squeezing.

### 6.4.3 Technical Requirements

#### 6.4.3.1 Compensating Quadratic Zeeman Shift

The splitting between Zeeman sublevels is created with a bias magnetic field. However, it will also induce quadratic Zeeman shift which is proportional to $m_F^2$. As a result, the frequency splitting between adjacent Zeeman sublevels will not be the same anymore, which excites the nematic spin components and the rigid body rotation of $\hat{L}_x$, $\hat{L}_y$ and $\hat{L}_z$ no longer holds. The rotation for spin-1 system is described by SU(3) group, which has 8 infinitesimal generators. The spin components other than $\hat{L}_x$, $\hat{L}_y$ and $\hat{L}_z$ are called the nematic spin components.

The quadratic Zeeman shift between $|F = 1, m_F = 0\rangle$ and $|F = 1, m_F = \pm 1\rangle$ is estimated to be 64 Hz, if $\omega_0 = 2\pi \times 1$ MHz, comparable to the two-photon Rabi frequency which is about

120 Hz. We could take advantage of the differential AC Stark shift between $|F = 1, m_F = 0\rangle$ and $|F = 1, m_F = \pm 1\rangle$ from off-resonant $\pi$-polarized microwaves to compensate the quadratic Zeeman shift, which has been demontrated to be good to below 1 Hz level [38, 109].

#### 6.4.3.2 Phase Noise from the Driving Tones

Fig. 6.8b shows the hierarchy of frequencies. With perfect balance of the two superradiance paths, we don't expect any emission at $\omega_c$, so the output of the homodyne detector comes from the beating between the 1/2 vacuum photon at $\omega_c$ and the local oscillator (LO). However, because the finite linewidth of the driving tones and the LO, there is actually additional noise contributions to the homodyne detection from the beating between the driving tones and the LO, which is the source of noise of our detection. The number of vacuum noise photons is 1/2, so the quantum efficiency of the detection is QE=$\frac{1/2}{1/2+N_n}$, with $N_n$ the number of noise photons from the driving tones. We want a small $N_n$ to maintain a large quantum efficiency.

To understand why the beating between the driving tones and the LO matters, we will consider the case where we replace the cavity in Fig. 6.8c with a mirror first. As discussed in Sec. 4.5.6 (see Eq. (4.12)), the phase noise of a laser can be modeled as phase modulations of the carrier with different modulation frequencies. The modulation index $\beta$ depends on the power spectral density of instantaneous phase fluctuations. The electric field of the blue driving tone, the orange driving tone and the LO, including the carrier and the noise components at modulation frequency $\omega_0$ only, can be written as

$$E_b = E_{b0}\cos(\omega_c t + \phi_{c0} + \omega_0 t + \phi_0 + \beta\cos(\omega_0 t + \phi_p)) \tag{6.26}$$

$$E_o = -E_{o0}\cos(\omega_c t + \phi_{c0} - \omega_0 t - \phi_0 + \beta\cos(\omega_0 t + \phi_p)) \tag{6.27}$$

$$E_{LO} = E_{LO0}\cos(\omega_c t + \phi_{c0} + \phi_h + \beta\cos(\omega_0 t + \phi_p)), \tag{6.28}$$

in which we assume that all three tones are derived from the same master laser, and that the blue and orange driving tones are generated by phase modulating a laser so that $E_{b0} = E_{o0}$. $\omega_c t + \phi_{c0}$

is the phase of the master laser. $\omega_0 t + \phi_0$ is the phase of microwave tone for the phase modulation. $\phi_h$ is the additional phase gained by the LO. $\phi_p$ is the phase of the noise components.

In the limit $\beta$ is small, Eq. (6.26) can be rewritten as $E_b = E_{bc} + E_{b+} + E_{b-}$. The expressions for $E_{bc}$, $E_{b+}$ and $E_{b-}$ are

$$E_{bc} = E_{b0}\cos(\omega_c t + \phi_{c0} + \omega_0 t + \phi_0) \tag{6.29}$$

$$E_{b+} = \frac{\beta}{2} E_{b0}\cos(\omega_c t + \phi_{c0} + 2\omega_0 t + \phi_0 + \phi_p) \tag{6.30}$$

$$E_{b-} = -\frac{\beta}{2} E_{b0}\cos(\omega_c t + \phi_{c0} + \phi_0 - \phi_p). \tag{6.31}$$

$E_{bc}$, $E_{b+}$ and $E_{b-}$ are at $\omega_c + \omega_0$, $\omega_c + 2\omega_0$ and $\omega_c$ respectively.

Likewise, we could write $E_o = E_{oc} + E_{o+} + E_{o-}$, with $E_{oc}$, $E_{o+}$ and $E_{o-}$ are at $\omega_c - \omega_0$, $\omega_c$ and $\omega_c - 2\omega_0$ respectively, and $E_{LO} = E_{LOc} + E_{LO+} + E_{LO-}$, with $E_{LOc}$, $E_{LO+}$ and $E_{LO-}$ are at $\omega_c$, $\omega_c + \omega_0$ and $\omega_c - \omega_0$ respectively.

The beating between the components at the same frequency will potentially contribute to the output of the homodyne detector, that is, the beating between $E_{LO+}$ and $E_{bc}$, between $E_{LO-}$ and $E_{oc}$, between $E_{LOc}$ and $E_b-$, and between $E_{LOc}$ and $E_{o+}$.

The output voltage $v_h$ of the homodyne detector from the beating of the three electric field components is

$$v_h \propto \frac{1}{2\pi}\int_0^{\frac{2\pi}{\omega_c}} (E_{b-} + E_{o+}) \times E_{LOc} + E_{oc}E_{LO-} + E_{bc}E_{LO+} dt, \tag{6.32}$$

We in fact have $v_h = 0$ here, because the transfer function of a mirror is not frequency-dependent.

If we switch back to the configuration shown in Fig. 6.8c, where the two driving tones reflect off a cavity, the electric field of the blue driving tone, the orange driving tone and the LO, will be modified as

$$E_b = E_{bc} + E_{b+} - E_{b-} \tag{6.33}$$

$$E_o = E_{oc} - E_{o+} + E_{o-}, \tag{6.34}$$

Notice that the $E_{b-}$ and $E_{o+}$ gain a minus sign, because these two tones are on resonance with the cavity and will gain an additional phase shift of $\pi$ when reflecting off the cavity.

Now we get $v_h \propto 2\beta E_{b0} E_{LO0} \cos(\phi_h) \sin(\phi_p - \phi_0)$. Notice that $\phi_h = 0$ here, because according to the discussions below Eq. (6.1), $\phi_{c0} + \phi_h = \frac{\psi_1+\psi_2}{2} + \frac{\pi}{2}$ with $\psi_1 = \phi_{c0} + \phi_0$ and $\psi_2 = \phi_{c0} - \phi_0 - \pi$. As a result, $\cos(\phi_h) = 1$ holds.

If we generate the blue and orange driving tones with amplitude modulation, we then have $v_h \propto 2\beta E_{b0} E_{LO0} \sin(\phi_h) \sin(\phi_p - \phi_0)$. With the same argument above, we now have $\phi_h = \pi/2$, so $\sin(\phi_h) = 1$ still holds.

Next, I will estimate how large the noise component is in unit of photon numbers. For a laser with linewidth $\kappa_l$, the number of noise photons is

$$N_n = \frac{2}{\pi\kappa_l} \frac{1}{1 + \left(\frac{\omega_0}{\kappa_l/2}\right)^2} \frac{P_1 + P_2}{E_{ph}} PF, \tag{6.35}$$

where $E_{ph}$ is the single photon energy, and PF is a polarization filtering factor since the LO and the driving tones have orthogonal polarizations. Notice that in Eq. (6.35), $\frac{2}{\pi\kappa_l} \frac{1}{1+\left(\frac{\omega_0}{\kappa_l/2}\right)^2}$ is the Lorentzian profile of a laser, so Eq. (6.35) can be intuitively viewed as the number of photons in the mode $\omega_0$ away from the carrier with total laser power $P_1 + P_2$. The typical value of PF is $10^{-4}$, which we will use in the following discussions.

The typical laser linewidth of an ECDL is 200 kHz. The number of noise photons is estimated to be 246 according to Eq. (6.35), so QE=0.002, which is awful.

If we could narrow down the linewidth to 1 kHz, the number of noise photons will be decreased to 1.2. The quantum efficiency can be calculated as QE=$\frac{1/2}{1/2+1.2}$=0.29, which starts to be acceptable. Building lasers with 1 kHz intrinsic Lorentzian linewidth is challenging, but DBR lasers with external feedback could be a potential way to achieve that linewidth [93, 108]. Of course, there

could be other solutions to beat down the number of noise photons, for example, suppressing laser phase noise in a certain frequency range with a notch filter, but I will not extend the discussions here.

## 6.5 Conclusion

I have introduced a theoretical proposal for continuous tracking of a quantum phase and direct creation of phase squeezed states, and presented and analyzed a potential experimental implementation in $^{87}$Rb. The implementation is demanding on the laser linewidth, which is challenging, but started to be within reach.

# Chapter 7

# Conclusion and Outlooks

In this thesis, I have presented an experiment for creating homogeneous atom-cavity coupling with site-dependent selections, where we achieved an average coupling strength of more than 91% the peak coupling strength with 4% remaining atoms. I have described an ongoing project, where we apply homogeneous spin-squeezed states, created by time-averaged probing of falling atoms, to build a spin-squeezed atom interferometer. These efforts are projected to make atom-cavity systems more powerful and improve the precision of quantum metrology. I have demonstrated a new cooling scheme based on adiabatic transfer on artificial Raman transitions, where we achieved 1D equilibrium temperature 25 times below the Doppler cooling limit in $^{87}$Rb. This cooling method could potentially be helpful for cooling quantum systems without cycling transitions, say, molecules. I have also reviewed a continuous phase tracking scheme and discussed a possible experimental implementation. The scheme is promising and could especially find its applications in the measurement of non-replicable processes, for example, searches for magnetic monopoles. The implementation is challenging in terms of its technical requirements, but the development of narrow linewidth DBR lasers with external feedback starts to catch up. In this chapter, I will talk about some future directions we could pursue.

## 7.1 Creation of Dicke States by Quenching Superradiance

This idea first came from a discussion with Prof. Nicola Poli from University of Florence, Italy. The definition of Dicke states was discussed in Sec. 3.1.1.1. Consider a cavity-assisted

superradiance process on a Raman transition (see Fig. 6.2) [10], which we have discussed in Sec. 6.3. The superradiance process can be visualized on Bloch spheres as shown in Fig. 7.1. If we quench the superradiance process by turning off the Raman dressing laser and count the number of photons emitted, we will be able to learn about how many atoms are left in $|\downarrow\rangle$ and how many atoms are transferred into $|\uparrow\rangle$, without collapsing individual atomic wavefunctions. In the meantime, the Bloch vector is actually in a superposition state of all possible azimuthal angles, since no phase information is collected. A Dicke state is thus created. If single photon resolution is not achievable due to noise, a collection of Dicke states will be created, and I will discuss this case in detail in the next paragraph.

The detection of the emitted photons is subject to a binomial distribution. Let's assume that the probability that a photon is detected is $Q$, and that the probability that a photon is missed by the detector is $1-Q$. The spin projection of the created state along $z$ is $m_J = (J - N_d/Q) \pm \sqrt{N_d(1-Q)}/Q$ if we initialize the atomic ensemble in $|J, J\rangle$, and detect $N_d$ photons before quenching the superradiance. If we take $Q = 0.9$, $J = N/2$ and $N_d/0.9 = N/2$ (assume $N$ is an even number) as an example, the projection along $z$ is $m_J = 0 \pm 0.47\Delta N_{SQL}$, where $\Delta N_{SQL} = \sqrt{N}/2$ is the standard quantum limit in $m_J$ for a coherent spin state. The cavity cooperativity parameter C or the atom number should be large enough to ensure that the collective emission rate is larger than the atomic decoherence rates. Single particle decoherence will shorten the length of the Bloch vector, and increases the standard deviation of the polar angle distribution of the state.

To confirm a Dicke state or a collection of Dicke states has been created, we could measure the number of atoms in $|\uparrow\rangle$ following $\pi/2$-pulses with different phases on resonance with $|\uparrow\rangle$ to $|\downarrow\rangle$ transition.

## 7.2 Understanding Limitations on the Creation of Spin Squeezing

In the 18 dB spin squeezing experiment [27], we actually had a technical noise floor of 25 dB below the quantum projection noise. We believed that the failure in saturating the technical noise floor should be attributed to the optomechanically-induced oscillations of the cavity resonance.

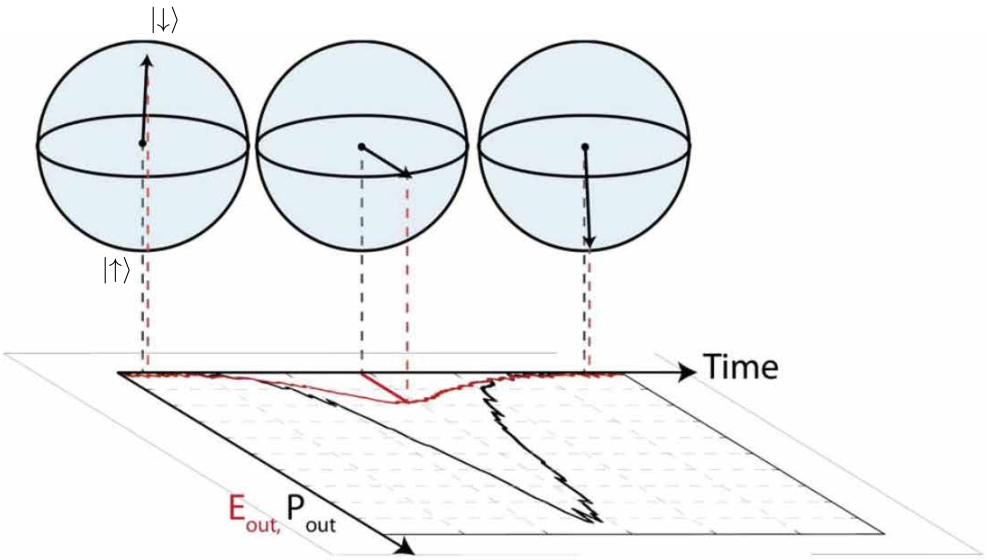


Figure 7.1: Raman superradiance visualized on Bloch spheres. The Bloch vector starts at the north pole ($|\downarrow\rangle$). Quantum fluctuations disturb the system from its unstable equilibrium transition, and eventually ends at the south pole. Reprinted from ref. [80]. To describe Raman superradiant decay in the Dicke basis, we should replace all the Bloch vectors with a superposition of Bloch vectors with all possible azimuthal angles and the same polar angle.

With the site-dependent selection technique, we expect to suppress the amplitude of the optomechanically-induced oscillations by more than a factor of 4 in the short time limit. We are now able to understand the limitations on the creation of spin squeezing better.

## 7.3 Closing Remarks

The early cQED experiments were done with Rydberg atoms flying through microwave cavities [46]. Nowadays, cQED experiments can be done with optical cavities, neutral atoms trapped in the Lamb-Dicke regime, and engineered homogeneous atom-cavity coupling, and thus enable explorations in spin-wave multiplexing [29], creation of atomic entanglement [51, 27, 44], cavity-mediated spin-spin interactions [79, 31], dynamical phase transitions [75] and synthetic quantum matter [23], to name a few.

Personally, the most fascinating application of cQED systems is still to precision measurements. Imagine that all you need to do to improve the precision of your quantum sensor is to

enclose it with two mirrors. That is how squeezed atomic clocks, squeezed atom interferometers, squeezed magnetometers, etc. can be built.

There are still more advanced ingredients that can be added to cQED systems, for example, high-order cavity modes [94] and atom assembly with optical-tweezer-arrays [33], to make the cQED systems more powerful. More exciting applications are yet to come.

## Bibliography


[1] H. Armandula and M. van Veggel. Silicate bonding procedure. LIGO Laboratory/LIGO Scientific Collaboration, Aug 2010.

[2] B. Barrett, A. Bertoldi, and P. Bouyer. Inertial quantum sensors using light and matter. Physica Scripta, 91(5):053006, 2016.

[3] John P. Bartolotta, Matthew A. Norcia, Julia R. K. Cline, James K. Thompson, and Murray J. Holland. Laser cooling by sawtooth-wave adiabatic passage. Phys. Rev. A, 98:023404, Aug 2018.

[4] James Bateman and Tim Freegarde. Fractional adiabatic passage in two-level systems: Mirrors and beam splitters for atomic interferometry. Phys. Rev. A, 76:013416, Jul 2007.

[5] Andrew J. Berglund, James L. Hanssen, and Jabez J. McClelland. Narrow-line magneto-optical cooling and trapping of strongly magnetic atoms. Phys. Rev. Lett., 100:113002, Mar 2008.

[6] T. Binnewies, G. Wilpers, U. Sterr, F. Riehle, J. Helmcke, T. E. Mehlstäubler, E. M. Rasel, and W. Ertmer. Doppler cooling and trapping on forbidden transitions. Phys. Rev. Lett., 87:123002, Aug 2001.

[7] Eric D. Black. An introduction to pound–drever–hall laser frequency stabilization. American Journal of Physics, 69(1):79–87, 2001.

[8] F. Bloch. Nuclear induction. Phys. Rev., 70:460–474, Oct 1946.

[9] [1] *Justin G. Bohnet. A superradiant laser and spin squeezed states: Collective phenomena in a rb cavity qed system for enhancing precision measurements. PhD thesis, JILA and University of Colorado at Boulder, 2014.

[10] *J. G. Bohnet, Z. Chen, J. M. Weiner, D. Meiser, M. J. Holland, and J. K. Thompson. A steady-state superradiant laser with less than one intracavity photon. Nature, 484:78, Apr 2012.

[11] *J. G. Bohnet, K. C. Cox, M. A. Norcia, J. M. Weiner, Z. Chen, and J. K. Thompson. Reduced spin measurement back-action for a phase sensitivity ten times beyond the standard quantum limit. Nature Photonics, 8(9):731–736, Sep 2014.


[1] * indicates the publication is from the Thompson group

[12] *Justin G. Bohnet, Zilong Chen, Joshua M. Weiner, Kevin C. Cox, and James K. Thompson. Linear-response theory for superradiant lasers. Phys. Rev. A, 89:013806, Jan 2014.

[13] Justin G. Bohnet, Brian C. Sawyer, Joseph W. Britton, Michael L. Wall, Ana Maria Rey, Michael Foss-Feig, and John J. Bollinger. Quantum spin dynamics and entanglement generation with hundreds of trapped ions. Science, 352(6291):1297–1301, 2016.

[14] Boris Braverman, Akio Kawasaki, Edwin Pedrozo-Peñafiel, Simone Colombo, Chi Shu, Zeyang Li, Enrique Mendez, Megan Yamoah, Leonardo Salvi, Daisuke Akamatsu, Yanhong Xiao, and Vladan Vuletić. Near-unitary spin squeezing in $^{171}$Yb. Phys. Rev. Lett., 122:223203, Jun 2019.

[15] Daniel W. C. Brooks, Thierry Botter, Sydney Schreppler, Thomas P. Purdy, Nathan Brahms, and Dan M. Stamper-Kurn. Non-classical light generated by quantum-noise-driven cavity optomechanics. Nature, 488(7412):476–480, Aug 2012.

[16] S. L. Campbell, R. B. Hutson, G. E. Marti, A. Goban, N. Darkwah Oppong, R. L. McNally, L. Sonderhouse, J. M. Robinson, W. Zhang, B. J. Bloom, and J. Ye. A fermi-degenerate three-dimensional optical lattice clock. Science, 358(6359):90–94, 2017.

[17] Julien Chabé, Hans Lignier, Pascal Szriftgiser, and Jean Claude Garreau. Improving raman velocimetry of laser-cooled cesium atoms by spin-polarization. Optics Communications, 274(1):254 – 259, 2007.

[18] Jasper Chan, TP Mayer Alegre, Amir H Safavi-Naeini, Jeff T Hill, Alex Krause, Simon Gröblacher, Markus Aspelmeyer, and Oskar Painter. Laser cooling of a nanomechanical oscillator into its quantum ground state. Nature, 478(7367):89–92, 2011.

[19] *Zilong Chen. Breaking quantum limits with collective cavity-qed: Generation of spin squeezed states via quantum non-demolition measurements. PhD thesis, JILA and University of Colorado at Boulder, 2013.

[20] *Zilong Chen, Justin G. Bohnet, Shannon R. Sankar, Jiayan Dai, and James K. Thompson. Conditional spin squeezing of a large ensemble via the vacuum rabi splitting. Phys. Rev. Lett., 106:133601, Mar 2011.

[21] *Zilong Chen, Justin G. Bohnet, Joshua M. Weiner, Kevin C. Cox, and James K. Thompson. Cavity-aided nondemolition measurements for atom counting and spin squeezing. Phys. Rev. A, 89:043837, Apr 2014.

[22] Steven Chu, JE Bjorkholm, A Ashkin, and Alex Cable. Experimental observation of optically trapped atoms. Physical Review Letters, 57(3):314, 1986.

[23] Logan W. Clark, Nathan Schine, Claire Baum, Ningyuan Jia, and Jonathan Simon. Observation of laughlin states made of light. Nature, 582(7810):41–45, Jun 2020.

[24] Giorgio Colangelo, Ferran Martin Ciurana, Lorena C. Bianchet, Robert J. Sewell, and Morgan W. Mitchell. Simultaneous tracking of spin angle and amplitude beyond classical limits. Nature, 543:525 EP –, Mar 2017.

[25] Christopher Corder, Brian Arnold, and Harold Metcalf. Laser cooling without spontaneous emission. Phys. Rev. Lett., 114:043002, Jan 2015.

[26] *Kevin C. Cox. Quantum-enhanced measurements with atoms in cavities: Superradiance and spin squeezing. PhD thesis, JILA and University of Colorado at Boulder, 2016.

[27] *Kevin C. Cox, Graham P. Greve, Joshua M. Weiner, and James K. Thompson. Deterministic squeezed states with collective measurements and feedback. Phys. Rev. Lett., 116:093602, Mar 2016.

[28] *Kevin C. Cox, Graham P. Greve, Baochen Wu, and James K. Thompson. Spatially homogeneous entanglement for matter-wave interferometry created with time-averaged measurements. Phys. Rev. A, 94:061601, Dec 2016.

[29] Kevin C. Cox, David H. Meyer, Zachary A. Castillo, Fredrik K. Fatemi, and Paul D. Kunz. Spin-wave multiplexed atom-cavity electrodynamics. Phys. Rev. Lett., 123:263601, Dec 2019.

[30] J. Dalibard and C. Cohen-Tannoudji. Laser cooling below the doppler limit by polarization gradients: simple theoretical models. J. Opt. Soc. Am. B, 6(11):2023–2045, Nov 1989.

[31] Emily J. Davis, Gregory Bentsen, Lukas Homeier, Tracy Li, and Monika H. Schleier-Smith. Photon-mediated spin-exchange dynamics of spin-1 atoms. Phys. Rev. Lett., 122:010405, Mar 2019.

[32] F Diedrich, JC Bergquist, Wayne M Itano, and DJ Wineland. Laser cooling to the zero-point energy of motion. Physical Review Letters, 62(4):403, 1989.

[33] Emma Dowd, Justin Gerber, and Dan Stamper-Kurn. Toward many-body cavity qed with addressable ultracold atoms. Poster presented at SQuInT, 2019.

[34] P. M. Duarte, R. A. Hart, J. M. Hitchcock, T. A. Corcovilos, T.-L. Yang, A. Reed, and R. G. Hulet. All-optical production of a lithium quantum gas using narrow-line laser cooling. Phys. Rev. A, 84:061406, Dec 2011.

[35] Alexander Dunning, Rachel Gregory, James Bateman, Matthew Himsworth, and Tim Freegarde. Interferometric laser cooling of atomic rubidium. Phys. Rev. Lett., 115:073004, Aug 2015.

[36] L. ESSEN and J. V. L. PARRY. An atomic standard of frequency and time interval: A cæsium resonator. Nature, 176(4476):280–282, Aug 1955.

[37] Martin Gärttner, Justin G. Bohnet, Arghavan Safavi-Naini, Michael L. Wall, John J. Bollinger, and Ana Maria Rey. Measuring out-of-time-order correlations and multiple quantum spectra in a trapped-ion quantum magnet. Nature Physics, 13:781 EP –, May 2017. Article.

[38] Fabrice Gerbier, Artur Widera, Simon Fölling, Olaf Mandel, and Immanuel Bloch. Resonant control of spin dynamics in ultracold quantum gases by microwave dressing. Phys. Rev. A, 73:041602, Apr 2006.

[39] Vittorio Giovannetti, Seth Lloyd, and Lorenzo Maccone. Quantum-enhanced measurements: Beating the standard quantum limit. Science, 306(5700):1330–1336, 2004.

[40] Peter W Graham, Jason M Hogan, Mark A Kasevich, and Surjeet Rajendran. New method for gravitational wave detection with atomic sensors. Phys. Rev. Lett., 110(17):171102, 2013.

[41] *G P Greve, B Wu, and J K Thompson. Laser cooling with adiabatic transfer on a raman transition. New Journal of Physics, 21(7):073045, jul 2019.

[42] Andrew T. Grier, Igor Ferrier-Barbut, Benno S. Rem, Marion Delehaye, Lev Khaykovich, Frédéric Chevy, and Christophe Salomon. Λ-enhanced sub-doppler cooling of lithium atoms in $D_1$ gray molasses. Phys. Rev. A, 87:063411, Jun 2013.

[43] Christian Gross. Spin squeezing, entanglement and quantum metrology with bose–einstein condensates. Journal of Physics B: Atomic, Molecular and Optical Physics, 45(10):103001, may 2012.

[44] B. Hacker, S. Welte, S. Daiss, A. Shaukat, S. Ritter, L. Li, and G. Rempe. Deterministic creation of entangled atom–light schrödinger-cat states. Nature Photonics, 13:110, Jan 2019.

[45] Paul Hamilton, Matt Jaffe, Philipp Haslinger, Quinn Simmons, Holger Müller, and Justin Khoury. Atom-interferometry constraints on dark energy. Science, 349(6250):849–851, 2015.

[46] Serge Haroche. Cavity quantum electrodynamics: a review of rydberg atom-microwave experiments on entanglement and decoherence. AIP Conference Proceedings, 464(1):45–66, 1999.

[47] Thomas P Heavner, Elizabeth A Donley, Filippo Levi, Giovanni Costanzo, Thomas E Parker, Jon H Shirley, Neil Ashby, Stephan Barlow, and S R Jefferts. First accuracy evaluation of NIST-f2. Metrologia, 51(3):174–182, may 2014.

[48] A. Heinz, A. J. Park, N. Šantić, J. Trautmann, S. G. Porsev, M. S. Safronova, I. Bloch, and S. Blatt. State-dependent optical lattices for the strontium optical qubit. Phys. Rev. Lett., 124:203201, May 2020.

[49] N Hinkley, JA Sherman, NB Phillips, M Schioppo, ND Lemke, K Beloy, M Pizzocaro, CW Oates, and AD Ludlow. An atomic clock with $10^{-18}$ instability. Science, 341(6151):1215–1218, 2013.

[50] Mahdi Hosseini, Yiheng Duan, Kristin M. Beck, Yu-Ting Chen, and Vladan Vuletić. Cavity cooling of many atoms. Phys. Rev. Lett., 118:183601, May 2017.

[51] Onur Hosten, Nils J. Engelsen, Rajiv Krishnakumar, and Mark A. Kasevich. Measurement noise 100 times lower than the quantum-projection limit using entangled atoms. Nature, 529:505, Jan 2016.

[52] Jiazhong Hu, Wenlan Chen, Zachary Vendeiro, Hao Zhang, and Vladan Vuletić. Entangled collective-spin states of atomic ensembles under nonuniform atom-light interaction. Phys. Rev. A, 92:063816, Dec 2015.

[53] Kai M. Hudek. A compact and transportable ultracold matter system and progress towards a continuously operating neutral rydberg atom quantum computer. PhD thesis, JILA and University of Colorado at Boulder, 2012.

[54] Tetsuya Ido, Yoshitomo Isoya, and Hidetoshi Katori. Optical-dipole trapping of sr atoms at a high phase-space density. Phys. Rev. A, 61:061403, May 2000.

[55] D F James and J Jerke. Effective hamiltonian theory and its applications in quantum information. Canadian Journal of Physics, 85(6):625–632, 2007.

[56] Hidetoshi Katori. Optical lattice clocks and quantum metrology. Nat. Photon., 5(4):203–210, March 2011.

[57] Hidetoshi Katori, Koji Hashiguchi, E. Yu. Il'inova, and V. D. Ovsiannikov. Magic wavelength to make optical lattice clocks insensitive to atomic motion. Phys. Rev. Lett., 103:153004, Oct 2009.

[58] Hidetoshi Katori, Tetsuya Ido, Yoshitomo Isoya, and Makoto Kuwata-Gonokami. Magneto-optical trapping and cooling of strontium atoms down to the photon recoil temperature. Phys. Rev. Lett., 82:1116–1119, Feb 1999.

[59] Colin J. Kennedy, Eric Oelker, John M. Robinson, Tobias Bothwell, Dhruv Kedar, William R. Milner, G. Edward Marti, Andrei Derevianko, and Jun Ye. Precision metrology meets cosmology: Improved constraints on ultralight dark matter from atom-cavity frequency comparisons. Phys. Rev. Lett., 125:201302, Nov 2020.

[60] Andrew J. Kerman. Raman sideband cooling and cold atomic collisions in optical lattices. PhD thesis, Stanford University, 2002.

[61] Masahiro Kitagawa and Masahito Ueda. Squeezed spin states. Phys. Rev. A, 47:5138–5143, Jun 1993.

[62] A. Kuzmich, L. Mandel, and N. P. Bigelow. Generation of spin squeezing via continuous quantum nondemolition measurement. Phys. Rev. Lett., 85:1594–1597, Aug 2000.

[63] X. Lacour, S. Guérin, L. P. Yatsenko, N. V. Vitanov, and H. R. Jauslin. Uniform analytic description of dephasing effects in two-state transitions. Phys. Rev. A, 75:033417, Mar 2007.

[64] Jongmin Lee, Geert Vrijsen, Igor Teper, Onur Hosten, and Mark A. Kasevich. Many-atom–cavity qed system with homogeneous atom–cavity coupling. Opt. Lett., 39(13):4005–4008, Jul 2014.

[65] Ian D. Leroux, Monika H. Schleier-Smith, and Vladan Vuletić. Implementation of cavity squeezing of a collective atomic spin. Phys. Rev. Lett., 104:073602, Feb 2010.

[66] Ian D. Leroux, Monika H. Schleier-Smith, and Vladan Vuletić. Orientation-dependent entanglement lifetime in a squeezed atomic clock. Phys. Rev. Lett., 104:250801, Jun 2010.

[67] Thomas H. Loftus, Tetsuya Ido, Andrew D. Ludlow, Martin M. Boyd, and Jun Ye. Narrow line cooling: Finite photon recoil dynamics. Phys. Rev. Lett., 93:073003, Aug 2004.

[68] Andrew D. Ludlow, Martin M. Boyd, Tanya Zelevinsky, Seth M. Foreman, Sebastian Blatt, Mark Notcutt, Tetsuya Ido, and Jun Ye. Systematic study of the $^{87}$Sr clock transition in an optical lattice. Phys. Rev. Lett., 96:033003, Jan 2006.

[69] Jian Ma, Xiaoguang Wang, C.P. Sun, and Franco Nori. Quantum spin squeezing. Physics Reports, 509(2):89–165, 2011.

[70] G. Edward Marti, Ross B. Hutson, Akihisa Goban, Sara L. Campbell, Nicola Poli, and Jun Ye. Imaging optical frequencies with 100 $\mu$Hz precision and 1.1 $\mu$m resolution. Phys. Rev. Lett., 120:103201, Mar 2018.

[71] Harold J. Metcalf and Peter van der Straten. Laser Cooling and Trapping. Springer-Verlag, New York, 1999.

[72] P. Meystre and M. Sargent. Elements of Quantum Optics, chapter System-Reservoir Interactions. Springer Berlin Heidelberg, 1998.

[73] X. Miao, E. Wertz, M. G. Cohen, and H. Metcalf. Strong optical forces from adiabatic rapid passage. Phys. Rev. A, 75:011402, Jan 2007.

[74] William R. Milner, John M. Robinson, Colin J. Kennedy, Tobias Bothwell, Dhruv Kedar, Dan G. Matei, Thomas Legero, Uwe Sterr, Fritz Riehle, Holly Leopardi, Tara M. Fortier, Jeffrey A. Sherman, Judah Levine, Jian Yao, Jun Ye, and Eric Oelker. Demonstration of a timescale based on a stable optical carrier. Phys. Rev. Lett., 123:173201, Oct 2019.

[75] *Juan A. Muniz, Diego Barberena, Robert J. Lewis-Swan, Dylan J. Young, Julia R. K. Cline, Ana Maria Rey, and James K. Thompson. Exploring dynamical phase transitions with cold atoms in an optical cavity. Nature, 580(7805):602–607, Apr 2020.

[76] *Juan A. Muniz, Dylan J. Young, Julia R. K. Cline, and James K. Thompson. Cavity-qed determination of the natural linewidth of the $^{87}$sr millihertz clock transition with 30$\mu$hz resolution. 2020.

[77] TL Nicholson, SL Campbell, RB Hutson, GE Marti, BJ Bloom, RL McNally, W Zhang, MD Barrett, MS Safronova, GF Strouse, et al. Systematic evaluation of an atomic clock at $2 \times 10^{-18}$ total uncertainty. Nature Communications, 6, 2015.

[78] T. Noel, M. R. Dietrich, N. Kurz, G. Shu, J. Wright, and B. B. Blinov. Adiabatic passage in the presence of noise. Phys. Rev. A, 85:023401, Feb 2012.

[79] *M. A. Norcia, R. J. Lewis-Swan, J. R. K. Cline, B. Zhu, A. M. Rey, and J. K. Thompson. Cavity-mediated collective spin-exchange interactions in a strontium superradiant laser. Science, 361:259, Jul 2018. Article.

[80] *M. A. Norcia, M. N. Winchester, J. R. K. Cline, and J. K. Thompson. Superradiance on the millihertz linewidth strontium clock transition. Science Advances, 2:e1601231, Oct 2016.

[81] *Matthew A. Norcia, Julia R. K. Cline, John P. Bartolotta, Murray J. Holland, and James K. Thompson. Narrow-line laser cooling by adiabatic transfer. New J. Phys., 20:023021, 2017.

[82] Edwin Pedrozo-Peñafiel, Simone Colombo, Chi Shu, Albert F. Adiyatullin, Zeyang Li, Enrique Mendez, Boris Braverman, Akio Kawasaki, Daisuke Akamatsu, Yanhong Xiao, and Vladan Vuletić. Entanglement on an optical atomic-clock transition. Nature, 588(7838):414–418, Dec 2020.

[83] N. Petersen, F. Mühlbauer, L. Bougas, A. Sharma, D. Budker, and P. Windpassinger. Sawtooth-wave adiabatic-passage slowing of dysprosium. Phys. Rev. A, 99:063414, Jun 2019.

[84] Alexander Prehn, Martin Ibrügger, Rosa Glöckner, Gerhard Rempe, and Martin Zeppenfeld. Optoelectrical cooling of polar molecules to submillikelvin temperatures. Phys. Rev. Lett., 116:063005, Feb 2016.

[85] E. M. Purcell, H. C. Torrey, and R. V. Pound. Resonance absorption by nuclear magnetic moments in a solid. Phys. Rev., 69:37–38, Jan 1946.

[86] Norman F. Ramsey. A molecular beam resonance method with separated oscillating fields. Phys. Rev., 78:695–699, Jun 1950.

[87] C. Jess Riedel. Direct detection of classically undetectable dark matter through quantum decoherence. Phys. Rev. D, 88:116005, Dec 2013.

[88] Simon M. Rochester, Konrad Szymański, Mark Raizen, Szymon Pustelny, Marcis Auzinsh, and Dmitry Budker. Efficient polarization of high-angular-momentum systems. Phys. Rev. A, 94:043416, Oct 2016.

[89] G. Rosi, F. Sorrentino, L. Cacciapuoti, M. Prevedelli, and G. M. Tino. Precision measurement of the newtonian gravitational constant using cold atoms. Nature, 510(7506):518–521, June 2014.

[90] Marianna S. Safronova, Sergey G. Porsev, Christian Sanner, and Jun Ye. Two clock transitions in neutral yb for the highest sensitivity to variations of the fine-structure constant. Phys. Rev. Lett., 120:173001, Apr 2018.

[91] Evan A. Salim. Ultracold matter systems and atomtronics instrumentation. PhD thesis, JILA and University of Colorado at Boulder, 2015.

[92] G. Salomon, L. Fouché, P. Wang, A. Aspect, P. Bouyer, and T. Bourdel. Gray-molasses cooling of 39 k to a high phase-space density. EPL (Europhysics Letters), 104(6):63002, dec 2013.

[93] Polnop Samutpraphoot, Sophie Weber, Qian Lin, Dorian Gangloff, Alexei Bylinskii, Boris Braverman, Akio Kawasaki, Christoph Raab, Wilhelm Kaenders, and Vladan Vuletić. Passive intrinsic-linewidth narrowing of ultraviolet extended-cavity diode laser by weak optical feedback. Opt. Express, 22(10):11592–11599, May 2014.

[94] Nathan Schine, Michelle Chalupnik, Tankut Can, Andrey Gromov, and Jonathan Simon. Electromagnetic and gravitational responses of photonic landau levels. Nature, 565(7738):173–179, Jan 2019.

[95] Nathan Schine, Albert Ryou, Andrey Gromov, Ariel Sommer, and Jonathan Simon. Synthetic landau levels for photons. Nature, 534(7609):671–675, Jun 2016.

[96] Monika H. Schleier-Smith, Ian D. Leroux, and Vladan Vuletić. Squeezing the collective spin of a dilute atomic ensemble by cavity feedback. Phys. Rev. A, 81:021804, Feb 2010.

[97] Monika H. Schleier-Smith, Ian D. Leroux, and Vladan Vuletić. States of an ensemble of two-level atoms with reduced quantum uncertainty. Phys. Rev. Lett., 104:073604, Feb 2010.

[98] D. Schlippert, J. Hartwig, H. Albers, L. L. Richardson, C. Schubert, A. Roura, W. P. Schleich, W. Ertmer, and E. M. Rasel. Quantum test of the universality of free fall. Phys. Rev. Lett., 112:203002, May 2014.

[99] Athreya Shankar, Graham P. Greve, Baochen Wu, James K. Thompson, and Murray Holland. Continuous real-time tracking of a quantum phase below the standard quantum limit. Phys. Rev. Lett., 122:233602, Jun 2019.

[100] Simon Stellmer, Benjamin Pasquiou, Rudolf Grimm, and Florian Schreck. Laser cooling to quantum degeneracy. Phys. Rev. Lett., 110:263003, Jun 2013.

[101] K. Sueda, G. Miyaji, N. Miyanaga, and M. Nakatsuka. Laguerre-gaussian beam generated with a multilevel spiral phase plate for high intensity laser pulses. Opt. Express, 12(15):3548–3553, Jul 2004.

[102] J. D. Teufel, T. Donner, Dale Li, J. W. Harlow, M. S. Allman, K. Cicak, A. J. Sirois, J. D. Whittaker, K. W. Lehnert, and R. W. Simmonds. Sideband cooling of micromechanical motion to the quantum ground state. Nature, 475:359 EP –, Jul 2011.

[103] Kurt R Vogel, Timothy P Dinneen, Alan Gallagher, and John L Hall. Narrow-line doppler cooling of strontium to the recoil limit. IEEE Transactions on Instrumentation and Measurement, 48(2):618–621, 1999.

[104] H. Wallis and W. Ertmer. Broadband laser cooling on narrow transitions. J. Opt. Soc. Am. B, 6(11):2211–2219, Nov 1989.

[105] W. Wasilewski, K. Jensen, H. Krauter, J. J. Renema, M. V. Balabas, and E. S. Polzik. Quantum noise limited and entanglement-assisted magnetometry. Phys. Rev. Lett., 104:133601, Mar 2010.

[106] *Joshua M. Weiner. Synchronization and sensing with steady state superradiance and spin squeezing. PhD thesis, JILA and University of Colorado at Boulder, 2015.

[107] Minghui Xu, Simon B. Jäger, S. Schütz, J. Cooper, Giovanna Morigi, and M. J. Holland. Supercooling of atoms in an optical resonator. Phys. Rev. Lett., 116:153002, Apr 2016.

[108] Megan Yamoah, Boris Braverman, Edwin Pedrozo-Pe nafiel, Akio Kawasaki, Bojan Zlatković, and Vladan Vuletić. Robust khz-linewidth distributed bragg reflector laser with optoelectronic feedback. Opt. Express, 27(26):37714–37720, Dec 2019.

[109] Yi-Quan Zou, Ling-Na Wu, Qi Liu, Xin-Yu Luo, Shuai-Feng Guo, Jia-Hao Cao, Meng Khoon Tey, and Li You. Beating the classical precision limit with spin-1 dicke states of more than 10,000 atoms. Proceedings of the National Academy of Sciences, 115(25):6381–6385, 2018.